UiO : University of Oslo

Vegard Skiftestad Olsen

Functional Properties and Band Gap Engineering of ZnO-GaN Alloys

Dissertation submitted for the degree of Philosophiae Doctor

The Department of Physics
Faculty of Mathematics and Natural Sciences

2020

© **Vegard Skiftestad Olsen, 2020**

Series of dissertations submitted to the
Faculty of Mathematics and Natural Sciences, University of Oslo
No. 2242

ISSN 1501-7710

All rights reserved. No part of this publication may be
reproduced or transmitted, in any form or by any means, without permission.

Cover: Hanne Baadsgaard Utigard.
Print production: Reprosentralen, University of Oslo.

Abstract

Highly crystalline thin films of $(ZnO)_{1-x}(GaN)_x$ were synthesised using RF magnetron sputtering, with x ranging from 0 to 0.20. The band gap of the alloys showed, as estimated, a significant reduction down to ∼2.5 eV for $x > 0.07$, by employing UV-VIS transmission measurements and electron energy loss spectroscopy, compared to the band gap energies of the two host materials, i.e. E_g^{ZnO} = 3.37 eV and E_g^{GaN} = 3.51 eV. The reduced band gap results in an extension of the absorption for the alloys well into the visible part of the spectrum. Structural analysis, utilizing x-ray diffraction, Rutherford backscattering spectrometry and transmission electron microscopy, yielded highly crystalline films, with columnar grains and a good heteroepitaxial relation to the Al_2O_3 substrate. The unit cell of the alloys was found to be rotated 30° with respect to the that of the substrate, in order to minimize the lattice mismatch to the substrate. An increase in c-lattice constant as a function of GaN content (x) was found, opposite to that predicted by Vegard's law, and explained in terms of strain, as well a high density of threading dislocations. The effects of thermal annealing in N_2 atmosphere after growth were analysed, both experimentally and using computational calculations employing density functional theory. Optically no large effects were found, especially in the estimated band gap energies. In terms of crystal structure, an increase in grain size was detected, reduced strain and c-lattice parameters approaching the expected values from Vegard's law, reduced dislocation density and an overall increase in crystalline quality. On the other hand, a systematic peak-broadening of the (0002) x-ray diffraction reflection was detected, attributed to an increase in Ga-N bonds. Moreover, for the films with higher x, an interfacial layer with a higher Ga-content compared to the remaining film was detected, attributed to the formation of zinc blende phases resulting from the accumulation of stacking faults. Nano-sized voids consisting of molecular N_2 were also found after post-deposition annealing, where the formation of voids was attributed to the agglomeration of Zn- and Ga-vacancies. The filling of voids with molecular N_2 was found to be a stabilization mechanism for the vacancy clusters, indicating that N is not stable in the O substitutional site. Finally, a deeper investigation of the mechanisms governing the band bowing effect in the $(ZnO)_{1-x}(GaN)_x$ alloys was undertaken, combining experimental and computational results. The results revealed the formation of a GaN-like defect band above the valence band maximum of ZnO to be the cause of the reduced band gap, oppositely to the explanation used in the literature, with orbital repulsions within the valence band, pushing the valence band maximum upward in energy.

Acknowledgements

There are many people that have contributed to the realization of this thesis. First of all, I want to thank my main supervisor Prof. Lasse Vines for giving me the opportunity of doing this doctoral study, and for being a true support through the entire work. He has always taken time out of his busy schedule to give advices and answer questions, and discussing with him has helped me greatly. For me, you have been an inspiration, and I am very grateful for having you as my supervisor. My co-supervisor Prof. Andrej Yu. Kuznetsov has contributed with guidance, his advices have always been very helpful and his experience has helped to elevate the scientific impact of my work. My second co-supervisor, Prof. Bengt Gunnar Svensson, sadly left us during my study, but I want to thank him with all my heart. His knowledge and understanding of science, which he gladly shared with all of us working at LENS, has helped me tremendously throughout my work.

I want to thank Dr. Kalliope Bazioti, Dr. Cecilie S. Granerød and Assoc. Prof. Øystein Prytz for providing TEM measurements and valuable discussions. A significant part of this thesis has been realized through our collaboration, and I am deeply grateful for your contributions. Gustavo Baldissera and Prof. Clas Persson have provided theoretical calculations that have enhanced the scientific impact of this thesis, and I am very grateful for our collaboration, relating theoretical and experimental results. I want to thank Christian Zimmerman and Dr. Augustinas Galeckas for providing PL results, and giving me a deeper understanding of optical properties of materials. I would also like to thank Dr. Alexander Azarov for contributing with RBS measurements and helpful discussions. To Dr. Klaus Magnus Johansen, I would like to say thank you for our discussion regarding my work. You have helped me to look at my results from different perspectives, and your advices have always been very helpful. A big thank you to the MiNaLab engineers, Micke, Halvor, Christoph and Viktor, for their tireless contributions in order to keep the MiNaLab up and running. Without your efforts, I would not have been able to obtain the results from various experimental techniques that constitutes this thesis.

I am very grateful for the social environment at LENS, and I want to thank all the Professors, researchers, PhDs and master students for making LENS such a great place to work. A special thanks to Heine, Mads, Sigbjørn, Kristin, Torunn and Marianne for making these years great. A special thanks to Ole Kristian, for motivating me throughout my PhD, giving me always useful tips. To my friends and family, and particularly my mom and dad, I am eternally grateful for always believing in me and cheering me on. Last, but not least, I want to thank my girlfriend, Sunniva. You have been the one that have listened when I have been frustrated, encouraged me when I have been tired and cheered me on when I have been excited. I am very, very grateful for all your help, and I love you for encouraging me and pushing me forward.

Thank you all so much!

Publications

Appended papers

I. V. S. Olsen, C. Bazioti, A. Azarov, B. G. Svensson, A. Yu. Kuznetsov, Ø. Prytz and L. Vines, *Bandgap bowing in crystalline* $(ZnO)_{1-x}(GaN)_x$ *thin films; influence of composition and structural properties*, Semiconductor Science and Technology 34, 015001 (2019)

II. V. S. Olsen, C. Bazioti, G. Baldissera, A. Azarov, Ø. Prytz, C. Persson, B. G. Svensson, A. Yu. Kuznetsov and L. Vines, *Effects of Substrate and Post-Deposition Annealing on Structual and Optical Properties of* $(ZnO)_{1-x}(GaN)_x$ *Films*, Physica Status Solidi B 256, 1800529 (2019)

III. V. S. Olsen, G. Baldissera, C. Zimmermann, C. S. Granerød, C. Bazioti, A. Galeckas, B. G. Svensson, A. Yu. Kuznetsov, C. Persson, Ø. Prytz and L. Vines, *Evidence of the defect band mechanism responsible for the band gap evolution in* $(ZnO)_{1-x}(GaN)_x$ *alloys*, Physical Review B 100, 165201 (2019)

IV. C. Bazioti, V. S. Olsen, A. Yu. Kuznetsov, L. Vines and Ø. Prytz, *Formation of* N_2 *bubbles along grain boundaries in* $(ZnO)_{1-x}(GaN)_x$*: nanoscale STEM-EELS studies*, Physical Chemistry Chemical Physics Communications (2020)

V. C. Bazioti, V. S. Olsen, A. Yu. Kuznetsov, L. Vines and Ø. Prytz, *Interfacial properties and the resulting defects of* $(ZnO)_{1-x}(GaN)_x$ *thin films grown on c-*Al_2O_3, Manuscript in preparation for publication, 2019.

Papers not appended

H. N. Riise, V. S. Olsen, A. Azarov, A. Galeckas, T. N. Sky, B. G. Svensson and E. Monakhov, *Local homoepitaxy of zinc oxide thin films by magnetron sputtering*, Thin Solid Films 601, 18-21(2016)

Contents

Publications **v**
Appended papers v
Papers not appended v

Contents **vii**

1 Introduction **1**

2 Physics of Semiconductors **5**
2.1 Crystal Structure 5
2.2 Band Structure 6
2.3 Absorption and Emission in a Semiconductor 9
2.4 Semiconductor Junction 10

3 Methodology **11**
3.1 Magnetron Sputtering 11
3.2 X-ray Diffraction 15
3.3 UV-VIS Transmission Measurements 18
3.4 Transmission Electron Microscopy 20
3.5 Photoluminescence 23
3.6 Secondary Ion Mass Spectrometry 25
3.7 Rutherford Backscattering Spectrometry 27
3.8 Density Functional Theory 27

4 The $(ZnO)_{1-x}(GaN)_x$ Alloys **31**
4.1 GaN and ZnO 31
4.2 The Band Bowing Effect 32
4.3 The $(ZnO)_{1-x}(GaN)_x$ Alloys in Hydrogen Production 34
4.4 Potential of the $(ZnO)_{1-x}(GaN)_x$ Alloys 35

5 Summary of Results **37**
5.1 Structural Properties of the $(ZnO)_{1-x}(GaN)_x$ Alloys 37
5.2 Effects of Thermal Annealing 39
5.3 Band Gap Evolution in $(ZnO)_{1-x}(GaN)_x$ Alloys 42
5.4 Electrical Properties 44

6 Conclusions and Future Work **49**

Bibliography **51**

Paper I 60

Paper II 70

Paper III 86

Paper IV 102

Paper V 114

Chapter 1

Introduction

The importance of semiconductor materials in the modern world is immense. A large variety of technologies in areas as communication, energy and health, to mention a few, would have been impossible to develop had it not been for the advances made in semiconductor physics. The invention of the transistor, using the semiconducting material germanium, in 1947 by John Bardeen, Walter Brattain and William Shockley, represents the official start of what today is seen upon as a number of crucial inventions that changed the course of humanity, and significantly increased the human well-being. Bardeen, Brattain and Shockley were in 1956 awarded the Nobel Prize in Physics *for their researches on semiconductors and their discovery of the transistor effect*[1]. The silicon-based integrated circuits mark another invention that has forever changed the world, as computers and mobile phones, are technologies that are easily taken for granted in our technological daily life.

Aiming the scope, optoelectronic and photoelectrochemical technologies fundamentally rely on the semiconductor material employed. Solar cells utilize the photo voltaic effect of semiconductor materials, harvesting green, renewable energy from the largest energy source available. The conversion of optical energy into electrical energy is also exploited in other photodiodes and photodetectors. Hydrogen production, another renewable energy source, through overall water splitting uses the photo-excited charge carriers in semiconductors to split water molecules into pure oxygen and hydrogen gas through redox reactions. The conversion of electrical charge carriers into photons is the basis of applications including light emitting diodes (LEDs) and lasers. Solid-state light sources, as LEDs, are advances in optoelectronics with enormous impact. With their smaller size, higher efficiency in converting electrical energy into light, and the absence of radiated heat, to mention a few, LEDs have several advantages over the conventional incandescent lamps[2]. These advantages are, in its turn, reflected in the rapidly increasing marked for LEDs and solid-state light sources, which have grown approximately 25% for each year the past several years[2].

Gallium nitride (GaN), a III-V compound semiconductor, has played a vital role in the development of optoelectronic devices, especially LEDs. GaN-based alloys, as InGaN, have been used extensively as the active layer, i.e. the light emitting layer in LEDs, with emission covering the violet, blue and green part of the visible spectrum[3]. Furthermore, the invention of the blue LED by I. Akasaki, H. Amano and S. Nakamura, based on GaN-alloys, for which they in 2014 were awarded the Nobel Prize in Physics[4], has made GaN-based blue LEDs the main provider of white light for space lighting. By employing a phosphor, a material that down-converts a fraction of the emitted light, the total output will appear white to the human eye[2]. Zinc oxide (ZnO), a II-VI compound semiconductor, exhibits many of the same intriguing properties for optoelectronic applications as GaN, and has due to its large exciton binding energy, been suggested as one of the competitors to exceed GaN in optoelectronics. Due to the

band gap of 3.37 eV, corresponding to the near ultra-violet (UV) region of the spectrum, ZnO has been employed as a transparent conductive oxide (TCO) contact on solar cells, and is promising for devices as photo detectors, lasers and LEDs, but the main obstacle of obtaining a stable, low-resistive *p*-type conduction, still prevents ZnO to live up to its potential.

Alloying semiconductor materials are extensively used in order to obtain application-specific properties. Band gap engineering of an alloy is an effective method to obtain band gap energies that is hard to achieve with, e.g. a binary semiconductor. An example is the already mentioned InGaN alloys, where the band gap of the alloys is tunable from 0.65 eV (InN) to 3.51 eV (GaN), by only changing the composition of the cat-ion. The band bowing effect, i.e. the deviation from the linear relationship between the band gap energy and the alloy composition, can be either upward or downward. In the case of InGaN, the band bowing effect is weak, and small compared to the energy difference between the two host compounds. Alloying ZnO and GaN, on the other hand, results in a significant downward bowing of the band gap, with large deviations from the linear change between 3.37 eV (ZnO) and 3.51 eV (GaN), and first exploited by Maeda et al.[5] for water splitting applications. Combining this observed band gap bowing with the intriguing optical properties of ZnO and GaN opens for potential use in optoelectronic applications as light emitting sources, as absorbing layer in solar cells, and as photodetectors, all with a tunable band gap from the UV- to well into the visible part of the spectrum.

The present work investigates the fundamental properties of the $(ZnO)_{1-x}(GaN)_x$ (ZOGN) alloys. Thin films of ZOGN with different GaN content, x, have been synthesised employing a widely used deposition technique in thin film industry, i.e magnetron sputtering, a method that is both easily up-scaled and allows for synthesis at relatively low growth temperatures. The crystalline quality of the hexagonal wurtzite crystal structure of the alloys was thoroughly investigated, employing characterization techniques as x-ray diffraction (XRD), transmission electron microscopy (TEM) and Rutherford backscattering spectroscopy (RBS), under different conditions as alloy composition, substrate lattice mismatch, and post-deposition annealing. Furthermore, a deeper investigation on the mechanisms governing the band gap evolution, or band bowing effect, in the ZOGN alloys has been made. The evidence obtained from this work, utilizing experimental techniques such as optical transmission measurements, photoluminescence (PL) and electron energy-loss spectroscopy (EELS), combined with computational calculations employing DFT and GW calculations, suggest that the earlier understanding of the mechanisms reducing the band gap in the ZOGN alloys, namely orbital repulsion within the valence band, might not be accurate.

This thesis is organized as follows. Chapter 2 introduces the semiconductor physics most relevant for this study. Chapter 3 is devoted to the various techniques employed, both experimentally and computational, to investigate the properties of the ZOGN alloys, and the effects of thermal treatment and lattice mismatch to the substrate. In Chapter 4, an introduction to the two compound semiconductors ZnO and GaN is given, as well as a detailed introduction to the band bowing effect, an effect that is observed in numbers of semiconductor alloys. Moreover, the pioneering work of Maeda et al.[6] utilizing this observed band bowing effect for hydrogen production is introduced, as well as the potential for utilizing the intriguing properties of ZOGN in optoelectronic

applications. Chapter 5 gives a summary of the main results of the appended papers, in addition to present unpublished results. The conclusions drawn from this study, as well as suggestions for further work is presented in Chapter 6.

Chapter 2

Physics of Semiconductors

In this chapter the relevant basic concepts in semiconductor physics are introduced. In particular, the interplay between the structural and optical properties of a semiconductor are highlighted, and how deviations from an ideal solid affect such properties.

2.1 Crystal Structure

A solid can be crystalline, being a single crystal, or polycrystalline with several crystalline domains of different orientation, or the material can be amorphous, i.e. with no long range periodic arrangement of atoms. In a crystalline material, the atoms are arranged in a crystal structure, and the periodicity within this crystal structure is called the lattice, which is an array of symmetric points. The most well-known semiconductor, silicon, has a diamond structure, composed of the unit cell, i.e. the smallest repeatable cell in the material, spanned by three lattice parameters, a, b and c. Another example of a crystal structure is the hexagonal wurtzite crystal structure, which is the thermodynamically most stable for ZnO and GaN at ambient conditions, as shown in Fig. 2.1 (a) for ZnO. The wurtzite crystal structure consists of alternating biatomic (0001) planes with a stacking sequence of AaBbAaBb$\cdots$ in the $\langle 0001 \rangle$ direction[7], illustrated in Fig. 2.1 (b). With two interpenetrating hexagonal close-packed (hcp) sublattices, all cations are surrounded by four anions and vice versa, as can be seen in Fig. 2.1 (a), forming tetrahedrons. These have generally sp^3 covalent bonds, but due to the ionicity of the II-VI and III-V semiconductors, the bonds in ZnO and GaN are a combination of ionic and covalent. Due to the alternating biatomic planes, the wurtzite structure has no inversion symmetry along the c-axis, making the materials polar, whereas a six-fold symmetry is found about the c-axis.

A real material contains deviations from the perfect crystal lattice, and these deviations are termed defects. The defects break the periodicity of atoms in different dimensions. Point defects, or defects in zero dimension (0D), includes a missing atom on a lattice point, a vacancy, or an atom outside a lattice point, an interstitial. Higher dimension defects are also often present in solids, where 1D and 2D are termed dislocations and planar defects, respectively. Planar defects include grain boundaries and stacking faults. Si and Ge, materials that can be synthesized with an incredible crystal quality, and with remarkably low defect concentrations, enables the study of single point defects. On the other hand, in this study, two compound semiconductors are alloyed using a physical deposition method, resulting in defect-rich thin films, compared to Si and Ge, including point defects, dislocations and planar defects.

Thin films are typically grown on substrates, and the material that is used as substrate will affect properties of the film, and the structural properties in particular. Homoepitaxy occurs when the growth of the film is of same material and has the same crystal structure as the substrate, and thus uses the substrate as a template for further growth.

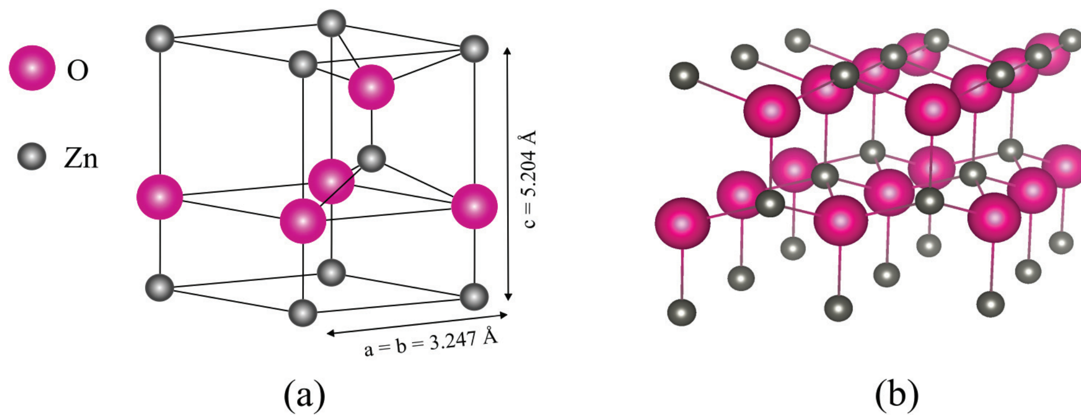

Figure 2.1: (a) Illustration of the hexagonal unit cell of wurtzite ZnO, and (b) with more atoms are added to illustrate the alternating biatomic planes. Figure (b) was made using the VESTA software[8].

Heteroepitaxy is similar, but where the substrate and film are different materials. Thin films can also be grown on substrates where only the crystal structure is the same, on substrates with different crystal structure, or with no structure at all, i.e. amorphous substrates. With respect to substrates and the crystal structure, strain is an important parameter that affects both structural and optical properties of a material. Strain in thin films is usually caused by stress due to defects and dislocations present in the crystal structure, as well as lattice mismatch to the substrate. If there is a mismatch between crystal structure or lattice parameters of the film and substrate, the thin film will be strained, i.e. either compressed or extended (compressive strain or tensile strain, respectively) in one or more dimensions. Naturally, the film will be least strained if grown homoepitaxially, e.g. ZnO on ZnO, where the main cause of stress will be structural defects in the film formed during growth. Higher strain is expected for films grown on substrates with both different crystal structure and thus also lattice parameters, as ZnO on Si, or films grown on amorphous substrates, e.g. ZnO on SiO_2. If the film is thicker than a critical thickness, it becomes energetically favourable to relieve this strain through the formation of defects, for example dislocations[9].

2.2 Band Structure

In an isolated atom, electrons can occupy discrete energy levels. When a large number of atoms are brought together to form a solid, these discrete energy levels split, due to Pauli's exclusion principle prohibiting two electrons with equal spin to occupy the same energy quantum state, eventually forming continuous bands. These bands depend on electron energy (E) and momentum (**k**), which again are material dependent, and a band diagram is thus often presented with a **k**-axis (x) and an energy-axis (y). The band structure is thus determined by the composition and periodicity of the material, and these bands can either be fully or partly occupied, or unoccupied by electrons, depending on the energy of the band. The highest band occupied by electrons at 0 K is

termed the valence band (VB), whereas the lowest unoccupied band at 0 K is called the conduction band (CB). In order to conduct electrical current, the CB must be occupied by electrons, termed *n*-type conduction, or the VB being occupied by holes, i.e. missing electrons, treated as charge carriers with opposite charge of electrons, termed *p*-type conduction. Metals have partly filled CBs, or the VB and CB overlap, resulting in a high conductivity. For semiconductors and insulators, the valence band maximum (VBM) and conduction band minimum (CBM) are separated by an energy gap - the band gap (see Fig. 2.2 (a)). The magnitude of this band gap is what separates semiconductors from insulators, as the band gap energy of a semiconductor is much smaller than that of insulators. The Fermi level separates the occupied and unoccupied states at 0 K. Thus, at 0 K, no insulator or semiconductor conducts current, because there is a zero probability of having electrons excited to the CB. For a semiconductor, when increasing the temperature, the energy will eventually allow for excitation of charge carriers to the CBM. If the VBM and CBM are located at the same wavevector, **k**, the semiconductor has a direct band gap, as in both ZnO and GaN. Oppositely, if VBM and CBM occurs at different **k**, a change in the electrons momentum is required for excitations over the band gap, and the band gap has an indirect nature. An important example of an indirect band gap semiconductor is Si. The change in momentum is achieved by the contribution of a phonon, i.e. a quantum of the lattice vibrations. When an electron is excited to the CB, a positive hole, is left behind in the VB, creating an electron-hole pair, EHP. In addition to thermal energy generating EHPs, other excitation sources can also generate charge carriers, e.g. by photoexcitation where a photon is absorbed and excites an electron to the CB.

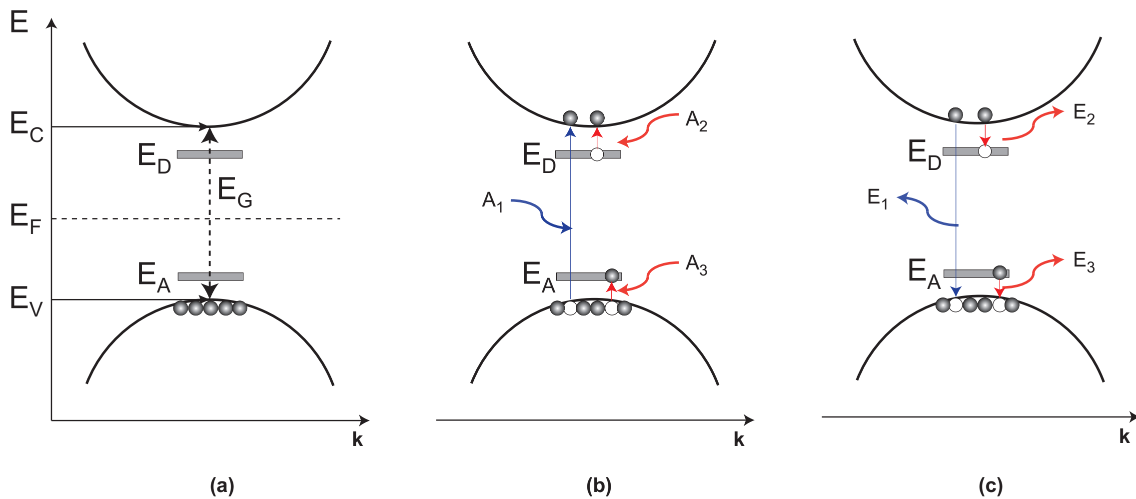

Figure 2.2: A simplified energy band diagram as a function of wavevector, **k**. (a) shows the valence- and conduction band edges, E_V and E_C, respectively, with a direct band gap of energy E_G. E_F illustrates the Fermi level, whereas E_D and E_A illustrate donor level and acceptor level in close proximity to the CB and VB, respectively. (b) shows three absorption processes; band-to-band absorption (A_1) as well as impurity absorption from a donor level (A_2) and acceptor level (A_3). (c) shows the recombination mechanisms yielding emission from band-to-band (E_1) and involving impurity levels (E_2 and E_3).

An ideal semiconductor material, where the charge carriers contributing to electrical conductivity are the EHPs generated by band-to-band excitations is called an intrinsic semiconductor, and the Fermi level is found approximately in the middle of the band gap (as in Fig. 2.2 (a)). A very powerful method of altering a semiconductors electrical properties is by doping, i.e. the introduction of impurity elements, acting as donors or acceptors. If the impurity atom has an extra valence electron compared to the host atom and is electrically active, the defect will form an energy state, or a defect level below the CBM (E_D in Fig. 2.2 (a)). A lower energy than the band gap is thus needed to excite the donor-electron to the CB, resulting in an excess of electrons, and the semiconductor has an *n*-type conduction. For *n*-type semiconductors, the Fermi level will be located closer to the CB compared to an intrinsic semiconductor. Oppositely, doping with an element with one electron less than the host results in a deficit of electrons, and the semiconductor has a *p*-type conduction and Fermi level closer to the VB.

2.2.1 Band Gap Dependencies

The mechanisms governing the band gap evolution in, for instance, alloys are not easily determined. The band gap of a semiconductor is, as mentioned, very material dependent, and both the discrete energy levels of the elements constituting the semiconductor material, as well as the interatomic distances, affect the band gap energy. The band gap dependencies of semiconductors are often described in terms of interatomic distances, since the formation of energy bands is caused by bringing atoms together. By continuously increasing the interatomic distance, while holding all other parameters the same, the band gap energy decreases. Thus, a general trend is an increase in interatomic distance reduces that band gap energy, and vice versa. The band gap energy of pristine, stoichiometric materials may hence be altered in several ways, including temperature and strain; temperature affect the interatomic distances by altering the atomic vibration amplitudes, meaning that a higher temperature results in a larger interatomic distance. Strain in the crystal structure will naturally also affect the band gap of materials, since strain is a quantification of the deviation in lattice parameters from the ideal case, often caused by stress applied to the structure.

The band gap is, as previously mentioned, defined as the energy gap between VBM and CBM. In real materials, there might be a deviation between the actual band gap of the material and the energy gap that is measured - the apparent band gap. This apparent band gap can be affected by for instance doping. If a *n*-type semiconductor is heavily doped, and the electron effective mass is low, resulting in a sharper curvature at the bottom of the CB, the E_F and the lowest unfilled energy level are located above the CBM. The result is an excitation over a higher energy than the band gap, meaning that the apparent band gap is larger than the actual band gap, called the Moss-Burstein effect[10, 11]. Thus, the impurity concentration and the magnitude of the charge carriers effective mass is related to a shift in the apparent band gap, which for increasing impurity concentration results in a blueshift. On the other hand, the apparent band gap can also be smaller than the real band gap. Defects, dislocations, compositional disorder and localized states form tails of the VB and CB density-of-states[12]. These tails result in absorption edges that increase exponentially in the lower energy range, allowing for sub-band gap absorption. This absorption tail is known as Urbach tail[13], and

the size of this tail is related to the density of defects, impurities and localized states. Highly crystalline, pure semiconductor materials, will thus have small Urbach tailing, and hence an abrupt absorption edge.

As much as strain, defects and impurities can affect the band gap of a material, the variation in the band gap energy can be significantly different when mixing materials, i.e. by alloying. The alloys may have properties as lattice parameters and band gap energy that are significantly different from the two host materials. For example, it is known that the VB in ZnO consist mainly of O states, whereas N states constitutes most of the VB in GaN. As these anion states have different energy, it may be foreseen that the VB undergoes changes when ZnO and GaN are alloyed together, compared to the VBs of the hosts. In other words, a change in the states that constitutes the VB and CB upon alloying will naturally affect the band gap. A dependency in band gap energy upon alloying known as the band bowing effect is described in more detail in section 4.2.

2.3 Absorption and Emission in a Semiconductor

A semiconductor material can absorb light through a number of mechanisms depending on the photon energy, including band-to-band- and impurity absorption. The band-to-band absorption of a direct, crystalline semiconductor is directly related to the band gap energy, where the absorption of a photon excites an electron from the VB to the CB, generating an EHP, as illustrated as A_1 in Fig. 2.2 (b). Absorption by impurities is also important when investigating sputter deposited thin film semiconductors, where the number of impurities are typically higher than e.g. in single crystal Si and Ge. Impurities results in energy states within the band gap, also allowing below-band gap absorption. The impurity states can be either donor or acceptor levels depending on the impurity's nature of donating or accepting an electron to the CB or from the VB, respectively, either by thermal excitation or absorption of photons, as illustrated by A_2 and A_3 in Fig. 2.2 (b). Furthermore, the impurity level is termed shallow or deep, depending on the energy-distance to the respective bands. The opposite process to absorption is emission, where excited electrons decay back to an energy state, e.g., the VB or an impurity level, and recombine with a hole by emitting a photon, with the energy equal to the energy difference between the two states. Similarly to absorption, emission of photons can occur through recombination processes related to band-to-band transitions and band-to-impurity transitions, see E_1, E_2 and E_3 in 2.2 (c). Furthermore, excitons can also yield emission in semiconductors. An exciton is a neutral quasi-particle consisting of an electron bound together with a hole by the Coulomb force, and due to this attraction, the exciton has an energy slightly lower than the unbound electron and hole. Thus, as the exciton decays, emission of a photon with an energy lower than the band gap, where the energy difference between the energy of the emitted photon and the band gap is equal to the binding energy of the exciton. Excitonic emission is particularly relevant when discussing ZnO, which has a large exciton binding energy of 60 meV.

2.4 Semiconductor Junction

Optoelectronic applications utilizes, as the name implies, the optical and electronic properties of one or several semiconductor materials. Optoelectronic applications include solar cells, photodetectors and LEDs, which traditionally requires a pn-junction, a junction between a *p*-type and *n*-type material, although solar cells and photodiodes can also be made utilizing a Schottky junction between a semiconductor and a metal. In a pn-junction a neutral depletion region is formed at the junction as holes (electrons) from the *p*-side (*n*-side) diffuse over the junction and recombine. The width of this depletion region depends on e.g. the doping concentrations and the applied bias. An applied forward bias reduces the potential barrier and depletion width, resulting in an increase in the current. On the other hand, a reverse bias increases the potential barrier and in its turn the depletion width. In this case, only thermally generated EHPs (minority carriers) within a diffusion length of the depletion region can contribute to a small thermally generated current. Here, the number of EHPs and thus the magnitude of the generated current can be significantly increased with e.g. optical excitation of EHPs, which again depends on the band gap of the material. Power can be extracted from a photodiode, due to the photovoltaic effect, if it is operated in the fourth quadrant of the I-V characteristics, i.e., when junction voltage is positive, whereas photodetectors are usually operated in reverse bias (third quadrant).

Chapter 3
Methodology

This chapter serves to introduce the various experimental techniques and theoretical modelling utilized in this work. Thin film growth has been performed with magnetron sputtering, and several experimental techniques have been utilized to characterize the structural, optical and electrical properties of the thin films. Furthermore, theoretical calculations have been utilized to combine the experimentally obtained results to theory, in order to obtain a deeper understanding of the semiconductor alloys.

3.1 Magnetron Sputtering

Magnetron sputtering is a deposition technique widely used in the thin film industry. The method of sputtering has been under constant development, where the implementation of a magnet behind the sputter target in order to confine the plasma, giving the name magnetron sputtering, is one of the more important developments. Later, more advanced sputter processes have emerged, e.g. High-Power Impulse Magnetron Sputtering (HiPIMS) introduced by Kouznetsov et al.[14], utilizing a pulsed plasma discharge in order to generate a highly ionized plasma, making it a more efficient technique to deposit for instance nitrides. There are several advantages of magnetron sputtering compared to other deposition techniques, including low substrate temperatures, good adhesion to the substrate, up-scaling possibilities for industrial use, and the fact that co-sputtering, depositing alloys of materials with very different vapor-pressure, can be performed very easily[15]. Magnetron sputtering is a physical deposition technique, based on bombarding a target material with ions, which in turn will sputter off target-atoms in the direction of a substrate, illustrated in Fig. 3.1. In a low pressure chamber an inert gas is ionized, forming a plasma, which is confined in front of the target material (the cathode) using electric and magnetic fields. The strength of the magnetic field is adjusted so that electrons experience a cycloidal motion, increasing the ionization efficiency, whereas the ions remains unaffected. The positive ions (usually Ar^{+}) are accelerated towards the negatively biased cathode, bombarding the target surface and resulting in multiple atom collisions within the top atom layers of the target material, sputtering off atoms and diatoms towards the substrate. The energy of the incoming ion is determined by the applied voltage (V), whereas the number of ejected atoms, or the deposition rate, is proportional to the discharge current (I). In most sputtering systems, these two parameters are joined together as the target power ($P = VI$).

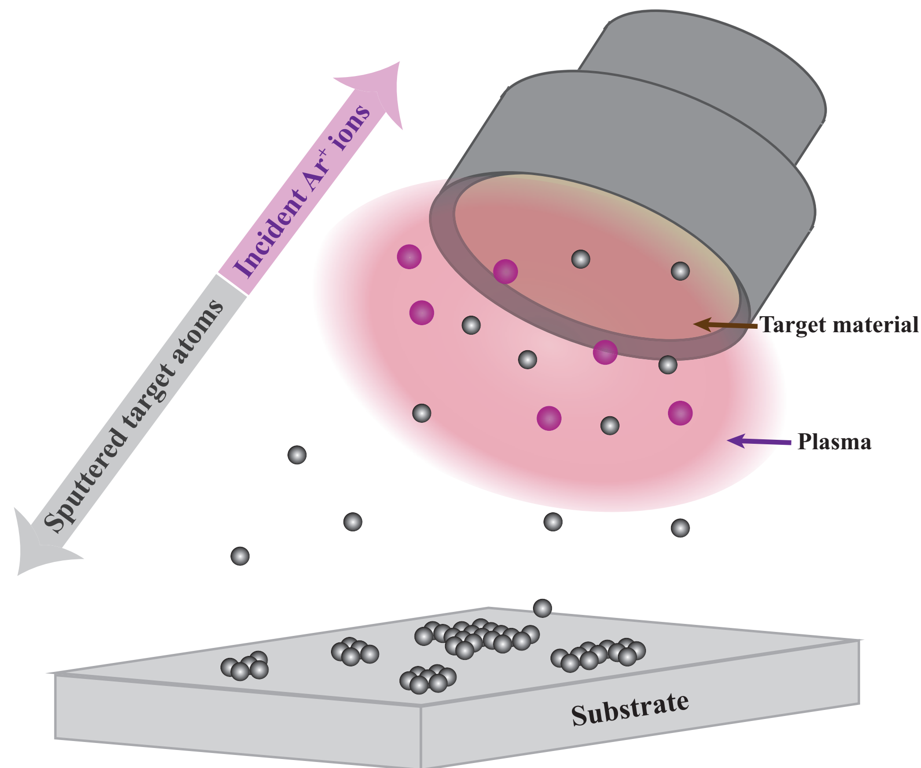

Figure 3.1: Schematic of a magnetron sputtering process. Positively charged plasma ions, usually Ar^+ (purple circles), are accelerated towards a negatively charged target material. Ion bombardment results in target atoms (grey circles) being ejected off the target in the direction of the substrate. The plasma is confined in front of the target due to a magnet on the backside of the target material.

3.1.1 Ion bombardment and plasma characteristics

As positive Ar^+ ions are bombarded onto the negatively biased cathode, different mechanisms can occur depending on the incident ion energy. If the ion energy is too low, the ions are reflected off- or adsorbed by the surface. The other extreme occurs if the ion energy is too high, resulting in the ions being implanted into the target material. Energies between that of adsorption and implantation yields a sputtering process, where the incoming ion bombards the cathode surface causing multiple atom collisions within the top layers of the target material, resulting in ejected atoms and molecules. At typical sputtering energies, this ejected material is constituted by about 95% atoms and the remaining part mostly being diatoms[16]. In addition to the incident ion energy, the deposition rate depend on the probability of a target atom being ejected, called the sputtering yield, as well as the transport through the plasma.

An additional result of the incident ions interaction with the cathode is the release of secondary electrons. These secondary electrons, being negatively charged, are accelerated from the cathode and towards the anode (in most systems being a shield around the target material). The secondary electrons, again having a cycloidal motion caused by the magnetic field, are accelerated though the plasma, causing further ionization. The plasma is therefore sustained by the sputtering process itself. If the target material is

insulating or semi-insulating, the release of secondary electrons will cause a build-up of positive charge on the target surface. As this net positive charge increases, the plasma eventually extinguishes. Therefore, when sputtering insulating materials the plasma is driven by an ac signal at radio frequency (RF), causing the electric field to oscillate between the two electrodes. The ions, being relatively slow, cannot follow the rapid oscillations, whereas the electrons are accelerated alternately towards the cathode and anode, resulting in both electrodes being negatively charged. Since the anode is usually connected to the chamber walls, and thereby maximizing the electrode area, the voltage difference between the two electrodes ensures that the ion accelerate towards the cathode.

3.1.2 Thin film growth

As the sputtered atoms and diatoms are incident on a substrate surface, the atoms can be adsorbed or desorbed. Through adsorption the atoms can nucleate 2D or 3D clusters, be captured by existing clusters or be captured by defects at the surface[17]. There are three main modes of crystal growth; the Volmer-Weber mode, also known as island growth, which occurs when atoms on the substrate surface are more strongly bound to the other deposited atoms than the substrate. Frank-van der Merwe mode is called the layer growth, where the deposited atoms form a monolayer on the substrate surface before forming a second layer. Layer growth occurs when the atoms are more strongly bound to the substrate than to each other. The last growth mode is called Stranski-Krastanov mode, which is a combination of the island and layer growth, where islands are energetically favourable after the formation one or more monolayers.

The quality of the deposited film or coating will naturally depend strongly on the growth conditions in terms of deposition parameters. The base pressure in the sputter chamber, i.e. the pressure before applying any gas, will give a strong indication on the purity of the deposited film. For nitride growth, unwanted oxygen may for instance, be introduced every time the chamber is exposed to atmosphere. In modern sputter systems, there is a separate chamber, or a load lock, for loading and unloading samples. The load lock is introduced in order to obtain a lowest possible base pressure, and in that way, mainly intentional impurities are incorporated into the growing film.

The growth of thin films can be divided into zones, describing the effects of process pressure (Ar) and substrate temperature (T/T_m, where T_m is the melting point in K of the sputtered material) on the morphology and topography of the sputtered films, as proposed by Movchan and Demchishin[18]. Thornton[19] modified this approach and divided the zone structure model into four zones, as illustrated in Fig. 3.2. In zone 1, at low substrate temperatures, the surface mobility is too low for the atoms to find energetically favourable sites, resulting in voided, porous grains with poor lateral strength. As the substrate temperature is increased (zone T), the surface mobility is increased and self-diffusion allows for denser, fibrous grains to form since voids are filled. In zone 2, the temperature is sufficient for atoms to diffuse between grains, and recrystallization is possible. Coatings deposited in zone 2 have larger, columnar grains of same crystal orientation that extend throughout the thickness of the film, since restructuring during growth is possible due to the larger atom mobility. In zone

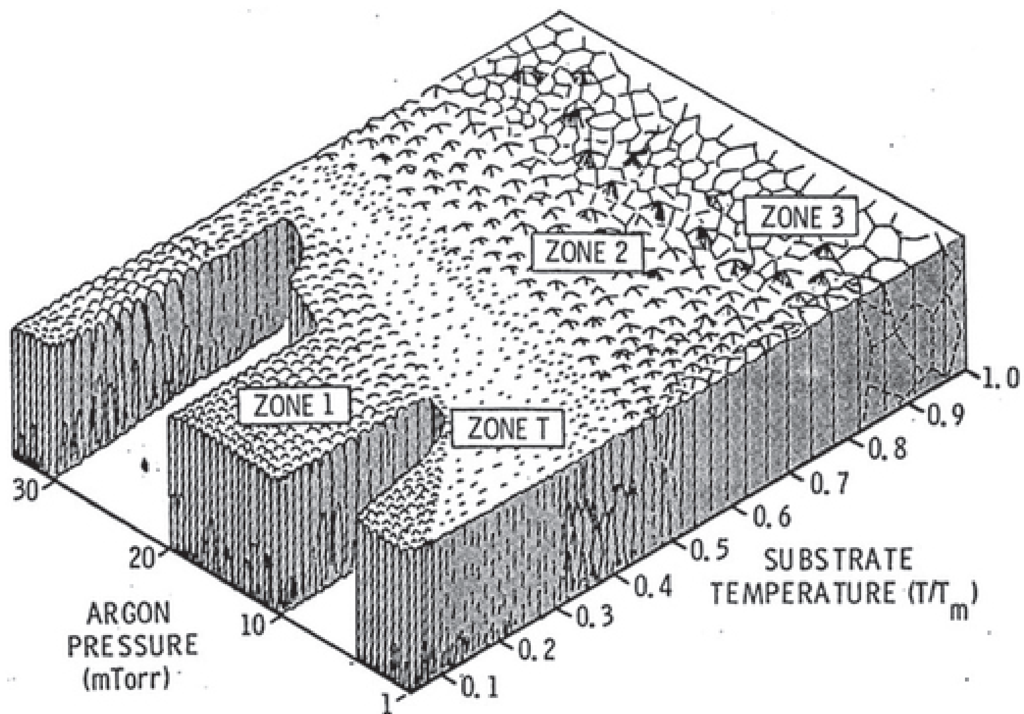

Figure 3.2: Structure zone model describing the effects of Ar pressure and substrate temperature on the morphology and topography of the sputtered film. Reproduced from J. A. Thornton, J. Vac. Sci. Technol. **11**, 666 (1974), with the permission of the American Vacuum Society.

3, the atom mobility both at the surface and in the bulk is high; recrystallization and restructuring occur during growth, resulting in larger grains with high crystal quality.

The most common inert gas utilized in sputter deposition is Ar, as mentioned previously. Other gasses can also be used both in combination to Ar, or separately, in order to obtain stoichiometric compositions, or to react with sputtered metal atoms. Reactive sputtering is widely used in industry since compound coatings can be sputtered using inexpensive and sturdy metal targets, e.g. AlN films using an Al target with N_2 as reactive gas. The introduction, and increasing flow of a reactive gas to the sputter process will, in addition to the composition, also strongly affect the deposition rate, making the process more complicated than regular inert Ar sputtering. For instance, if the flow of reactive gas, e.g. N_2, is sufficient for the partial pressure to form AlN, covering the Al target surface (in addition, the substrate), the deposition rate will decrease drastically, since the sputter yield for AlN is much lower than for Al. This is called target poisoning, and is one example of challenges associated with reactive sputtering. On the other hand, if the flow of N during reactive sputtering of AlN is too low, the deposited film will be more metallic.

For the ZOGN alloys, magnetron sputtering was chosen as the deposition technique since high quality thin films can be obtained at relatively low synthesis temperatures, the composition of the alloys can be controlled with high precision by tuning the applied powers on two separate ceramic targets, i.e. ZnO and GaN, of high purity, and the stoichiometry of the alloys can be optimized by changing the flow of nitrogen during

growth. In addition, synthesis of epitaxially grown ZnO thin films employing magnetron sputtering has successfully been a focus within the research group earlier[20], and formed a starting point for the ZOGN development. The instrument used in this study is a Moorfield MiniLab magnetron sputtering system with separate 3” ZnO (99.999%) and GaN (99.99%) ceramic targets.

3.2 X-ray Diffraction

To investigate structural properties of thin films, bulk materials or powders, X-ray diffraction (XRD) is an important and widely used technique. The general principle behind this technique is that incident x-rays, having a wavelength comparable to the atomic spacing, are scattered by the atoms in the material, and the number of scattered photons, as well as the scattering angle, is measured by a detector. The scattering that the x-rays undergoes is an elastic scattering by electrons, called Thomson scattering[21], where the electron is accelerated to oscillate at the frequency of the incident photon, and in turn emitting a photon with the same frequency. The incident ($\mathbf{K}_0$) and scattered ($\mathbf{K}$) waves, both vectors with magnitude $2\pi/\lambda$, are related through the scattering angle (abbreviated 2θ), which is the angle between $\mathbf{K}$ and the prolonged direction of $\mathbf{K}_0$. The vector difference between the incident and scattered waves is called the scattering vector $\mathbf{Q}$, illustrated in Fig. 3.3:

$$\mathbf{Q} = \mathbf{K} - \mathbf{K_0}. \tag{3.1}$$

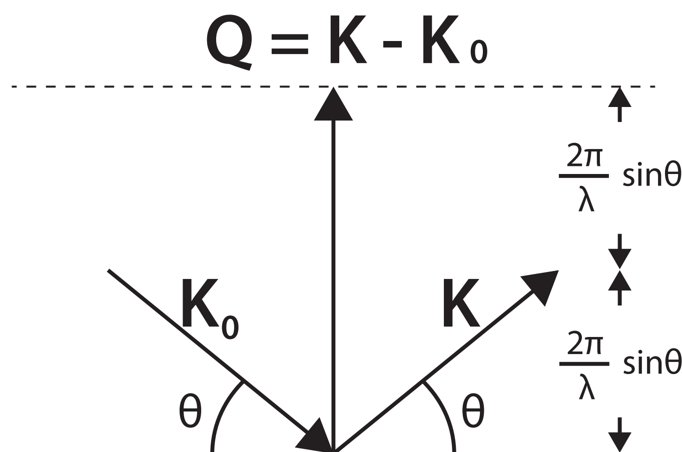

Figure 3.3: The scattering vector $\mathbf{Q}$ being the vector difference between the incident and scattered wave. The magnitude of $\mathbf{Q}$ equals $\frac{4\pi}{\lambda}$ $\sin\theta$.

.

If the material is crystalline, the atoms are arranged in lattice planes. For a simple cubic system, the condition for constructive scattering is given by the Laue equations:

$$\begin{aligned} a\mathbf{Q}\mathbf{a_1} &= 2\pi h \\ a\mathbf{Q}\mathbf{a_2} &= 2\pi k \\ a\mathbf{Q}\mathbf{a_3} &= 2\pi l \end{aligned} \tag{3.2}$$

where a is the lattice constant, $\mathbf{a}_1$, $\mathbf{a}_2$ and $\mathbf{a}_3$ are the unit vectors of the cubic unit cell and h, k, l are the Miller indices of the scattering plane (hkl). The magnitude of the scattering vector can thus be expressed as:

$$\frac{|\mathbf{Q}|}{2\pi} = \frac{\sqrt{h^2+k^2+l^2}}{a}. \tag{3.3}$$

By using the magnitude of $\mathbf{Q}$ being $\frac{4\pi}{\lambda}$ $\sin\theta$ from Fig. 3.3 and substituting for $|\mathbf{Q}|$ in Eq.3.3;

$$\lambda = 2\frac{a}{\sqrt{h^2+k^2+l^2}} sin\theta \tag{3.4}$$

The distance between two adjacent lattice planes is given by the interplanar spacing d_{hkl}, which for the simple cubic system is equal to $d_{hkl} = \frac{a}{\sqrt{h^2+k^2+l^2}}$, and by using the expression for d_{hkl} in Eq.3.4, Bragg's law is obtained:

$$2d_{hkl} sin\theta_B = n\lambda \tag{3.5}$$

where θ_B is the angle yielding maximum intensity. Thus constructive interference will occur when $2d_{hkl}$ $\sin\theta_B$ equals an integer multiple, n, of the wavelength. Bragg's law can also be understood as constructive interference that occurs when the waves that are scattered by lattice planes remain in phase, since the difference in path equals to an integer multiple of the wavelength, λ, as shown in Fig. 3.4.

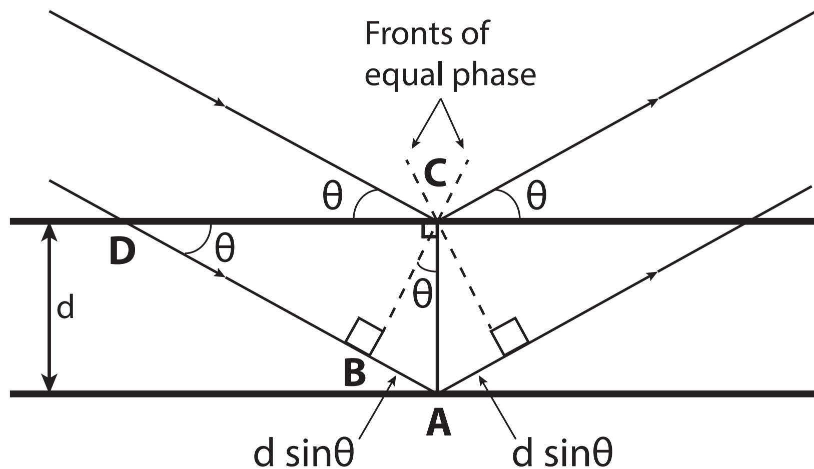

Figure 3.4: A schematic explanation of Bragg's law.

3.2.1 Scanning modes

In order to utilize Bragg reflections, and at the same time reduce the influence from fluctuations in the the scattered intensity due to variations in the sample-detector distance, both the x-ray source and detector are moved on a hemisphere with a constant radius to the sample. The Bragg reflections are of great interest, where their position, shape and intensity contain information related to material phases, structural properties and crystal quality. In the locked couple scan, or $\theta/2\theta$ scan, the x-rays are incident on the sample with an angle θ, and the detector measures the x-rays scattered from the sample with the same angle, θ. During a scan, both the angle of the incoming and exiting beams are varied continuously, but always equal to each other, i.e. $\theta_{in} = \theta_{out}$. Another interpretation of this scan is the variation of the exiting beam with respect to the prolonged incoming beam, i.e. 2θ[21]. A result of $\theta_{in} = \theta_{out}$ in the $\theta/2\theta$ scan is that **Q** will always be normal to the sample surface, meaning that only those crystallites with lattice planes *hkl* parallel to the sample surface can contribute to a Bragg reflection. By scanning over a range of 2θ angles, e.g. from 20° to 100°, several peaks may appear in the diffraction pattern. Each peak can be assigned to a specific plane of a unit cell. If a Bragg reflection is found at a Bragg angle θ_B, this peak can be assigned to a specific interplanar spacing d_{hkl} by using Eq. 3.5, where λ is the wavelength of the x-rays. The obtained interplanar spacing, d_{hkl}, can then be compared to a reference database. For a simple cubic material, the Bragg reflection can be assigned to a lattice plane *hkl* by solving $(a/d)^2 = h^2 + k^2 + l^2$, where a is the lattice parameter of the simple cubic unit cell. In this way, each peak in the diffraction pattern can be designated to a lattice plane, hkl. The $\theta/2\theta$ scan is thus a powerful tool to investigate which phases that are present in a sample, or to determine if a material is polycrystalline or a single crystal, by using the number of diffraction peaks, and their position. The peak position of a Bragg reflection in a diffraction pattern can also yield information about strain in the crystal structure responsible for that diffraction peak. If a peak position deviates from the relaxed- and unstrained position (e.g. from a single crystal) in the diffraction pattern, this deviation indicates that the crystal structure is subjected to either tensile- or compressive stain, depending on if the peak occurs at lower- or higher 2θ values, respectively. The broadness of the Bragg reflections, measured by the full-width at half maximum (FWHM), can also yield structural information about the material. If the material contains a high concentration of defects and dislocations, there will be a larger spread in the interplanar spacing d. A larger spread in d will again yield a broader Bragg reflection. The FWHM is also affected by the crystallite size, or grain size, where an increase in FWHM is usually interpreted as a decrease in the grain- or crystallite size as can be calculated by using the Scherrer equation[22]. In addition to the peak position and the broadness of the Bragg peak, the intensity yield information about the number of lattice planes contributing to the diffraction peak, where the most intense Bragg reflection is interpreted as the dominant crystal orientation, compared to other reflections that may appear in the diffraction pattern.

Another important scan mode is the rocking curve scan, or ω scan, which can give further information about, e.g., dislocations in the films. For the rocking curve scan, the detector is fixed at the intensity-maximum of a Bragg reflection, whereas the incident beam is scanned across the Bragg angle. Unlike the $\theta/2\theta$ scan, θ_{in} is no longer equal

to θ_{out}, meaning that the scattering vector, **Q**, which remained perpendicular to the surface throughout the $\theta/2\theta$ scan, is now systematically shifted from the surface normal. Dislocations in a material, in addition to altering the lattice spacing, can also cause tilt in the lattice planes. Therefore, a broadening in a rocking curve peak is interpreted as a larger spread in lattice plane tilt with respect to the surface normal, which can imply e.g. a higher concentration of dislocations in the material.

Utilization of XRD for the exploration of the ZOGN alloys is critical since the technique allows for a relatively fast way to obtain structural information about the sputtered films. XRD measurements yield, as mentioned, information about the crystal structure, the crystal orientation, the lattice constant (in respect to bulk values), and can also give indications on dislocation densities, all important parameters when investigating a new material. The initial XRD measurements were undertaken to ensure that the alloys were grown in the hexagonal wurtzite crystal structure, and that all crystallites or grains had the same crystal orientation, i.e. the (0002) orientation. Furthermore, as strain is an important factor in both the structural aspect of alloying, but also affect the optical properties, the *c*-lattice constant for each composition was measured and compared bulk ZnO. Rocking curve scans gave valuable indications on the dislocation density, later confirmed by transmission electron microscopy measurements.

The instrument used in this study is a Bruker AXS D8 discover system. The x-ray source employed was Cu Kα (λ = 1.5406 Å), and a Ge (220) double bounce monochromator was implemented to filter out the Kα_2 signal (λ = 1.5444 Å). The instrumental broadening of the diffraction peaks of 0.008° has been included in the standard error of the values given in this work.

3.3 UV-VIS Transmission Measurements

Several optical properties can be examined using a photospectrometer. As light is incident on a material, the light interacts with the sample through absorption, reflection or transmission. In a UV-VIS transmission measurement, light is incident on a sample, and the transmitted light is measured by a detector. The wavelength, and thus the energy of the incident light is varied from the ultra violet (UV)- to the visible part of the spectrum, forming a transmission spectrum, as can be seen in Fig. 3.5a. As a first approximation, if the incident light has energy lower than the band gap of the material, ideally no light would be absorbed. Oppositely, light with energy higher than that of the band gap would be absorbed, ideally yielding no transmission if the sample is sufficiently thick. In this way, the transmission spectrum can be used to determine the band gap of a material.

From the measured transmittance, the absorption coefficient, $\alpha(E)$, is calculated using relation;

$$T = \frac{(1-R)^2 e^{-\alpha d}}{1-R^2 e^{-2\alpha d}} \approx (1-R)^2 e^{-\alpha d} \tag{3.6}$$

where T is the measured transmittance, R is the reflectance (in the Tauc plot analysis in this work it is assumed to be negligible), and d is the measured thickness of the thin film. The equation for transmittance can be simplified for high absorption, as shown in

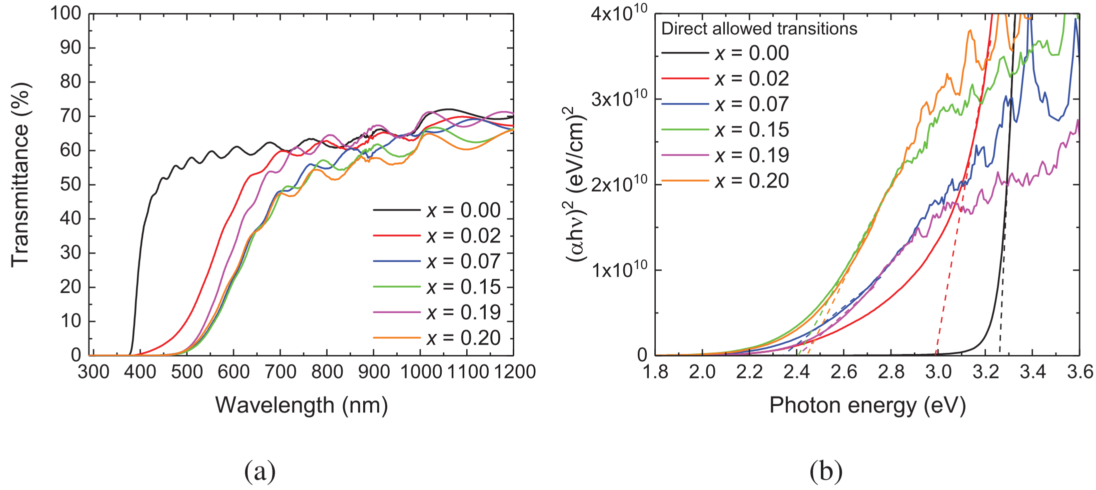

Figure 3.5: Example of band gap determination using (a) transmission measurements and (b) Tauc plot analysis for direct allowed transitions, i.e. r = 1/2. Plots from Olsen et al. [26]

equation (3.6). The calculated α is then plotted as a function of photon energy, E. In the energy region close to the band gap of the material, α will drop rapidly to zero, where the onset commonly interpreted as the material band gap. For band gap analysis, Tauc plots[23] are commonly employed, using the relation

$$[\alpha(E)h\nu]^{1/r} = c(h\nu - E_g) \tag{3.7}$$

where hν is the photon energy, c is a constant and r is a number that depends on the type of transition, where r = 1/2 or 2 for direct allowed transitions and indirect allowed transitions, respectively. In order to determine the band gap, using Tauc plot analysis, $(h\nu\alpha)^{1/r}$ is plotted as a function of the photon energy ($h\nu$), as shown in Fig. 3.5b. The intersect at the energy-axis with the extrapolation of the linear region, i.e. the onset where $(h\nu\alpha)^{1/r} = 0$, is interpreted as the material band gap. The deviation from the extrapolation of the linear region is commonly known as an absorption tail, or Urbach tail[13], and is normally related to disorder, localized states or compensation[24, 25].

Transmission measurements in this study were employed to estimate the band gap of the thin films deposited and to investigate the effects of composition, x, lattice-mismatch to the substrate, and post-deposition annealing. The band gap energies determined from Tauc plot analysis was also supported by scanning transmission electron microscopy, using an electron energy loss spectrometer.

For the transmission measurements in this study, a Shimadzu Solid Spe-3700 DUV spectrophotometer was employed. The covered wavelength rage was 175 - 2600 nm, with a resolution of 0.1 nm. There is an obvious source of errors when determining the optical band gap using Tauc analysis and extrapolating the linear region. Hence, the band gap energies determined from Tauc analysis, should be associated with a standard error of 0.05 eV.

3.4 Transmission Electron Microscopy

Transmission electron microscopy (TEM) is a powerful tool for investigating structural, chemical and functional properties of materials with high spatial resolution due to the small wavelength of electrons[27]. TEM operation can be divided into three main categories; diffraction, imaging and spectroscopy. The diffraction and imaging techniques utilizes the elastically scattered electrons, while spectroscopy use the electrons that are inelastically scattered from the specimen.

An important specification for a sample to be studied with TEM, is that it must be thin enough for electrons to be transmitted through. The specimens are thus, utilizing various sample preparation techniques, typically polished down to a thickness in the range of 100 nm, while for high-resolution imaging the optimum thickness is $\sim$10 nm. In the case of thin films, cross-section measurements are usually undertaken, in order to evaluate the bulk properties of the film, as well as the films relationship to the substrate.

In imaging mode of TEM, diffraction is used as contrast, utilizing the diffracted and transmitted electrons after interacting with the specimen, to form images. An aperture in the back focal plane of the objective lens can, for instance, only let the transmitted electrons pass, whereas the diffracted electrons are stopped by the aperture. The resulting image is a bright-field (BF) image, illustrated in Fig. 3.6 (a), where regions of the probed area that diffract will appear dark. Opposite, a dark-field (DF) image can be formed by utilizing only electrons that have undergone a specific diffraction condition, as shown in Fig. 3.6 (b). The regions that do not fulfil this diffraction condition will appear dark in the image. A specially useful case of DF imaging for characterizing dislocations in a material is the weak-beam dark-field (WBDF) condition. Here, the sample is tilted so that a diffraction condition is weak, and the image is quite dark. Dislocations on the other hand, causes the lattice planes close to the dislocation core to be bend into the diffraction condition, and will thus appear bright in the image. In addition to using diffraction as contrast in TEM imaging, the phase of the electron wave can also give contrast and this is known as high resolution (HR) TEM. In that case, both the transmitted beam and at least one (usually several) of the diffracted beams are utilized. In HRTEM, an image of columns of atoms, is in fact an interference pattern of the diffracted electron beam, with the phase of the transmitted beam as reference. Diffraction patterns can also be obtained using TEM in diffraction mode. In selected area diffraction (SAD), illustrated in Fig. 3.6 (c), an aperture is used to confine the diffraction pattern to a selected area of the sample, i.e. in the imaging plane. Since TEM allows for probing very small volumes compared to for instance XRD, the diffraction patterns obtained by TEM is more sensitive to deviations from an average structure, i.e. short-range ordering and defects[28].

In addition to conventional TEM, using a parallel electron beam incident on the specimen, scanning TEM (STEM) using a converged beam opens the possibility for mapping across a specimen. In STEM mode, the electron beam is converged to a small spot on the sample, which is rastered over the specimen. The transmitted electrons that are scattered elastically can be utilized for imaging using Annular Bright-Field (ABF) and Annular Dark-Field (ADF) detectors, as illustrated in Fig. 3.7. Electrons that are scattered elastically with larger angles, i.e. the collection angle, β, is large, can be collected by a High Angle Annular Dark-Field (HAADF) detector, and used

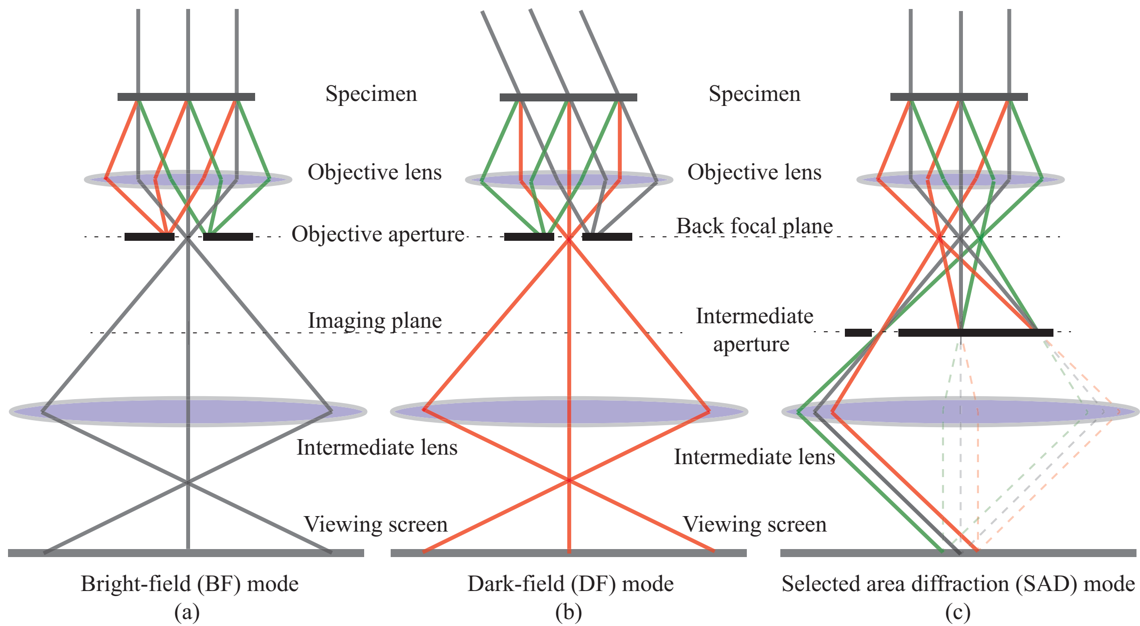

Figure 3.6: Schematic illustration of working in TEM-mode. (a) Bright-field (BF) mode imaging, with an objective aperture in the back focal plane blocking everything except the transmitted electrons. (b) Dark-field mode imaging, where the objective aperture only allows electrons with a certain diffraction condition to form an image. (c) Selected area diffraction (SAD), where an aperture located in the imaging plane, yielding diffraction pattern from a selected area of the specimen.

for Z-contrast imaging, since at high angles, the intensity is almost proportional to the square of the atomic number, Z.

The small electron spot, rastered over the specimen can furthermore be used to acquire emitted x-rays and inelastically scattered electrons[27]. Thus, by using STEM, spectroscopic mapping of the specimen, using techniques as energy dispersive x-ray spectrometry (EDS) and electron energy loss sepctroscopy (EELS), is made possible. EDS utilizes the fact that the incident electrons can excite inner-shell core electrons of atoms. These excited core-electrons can decay through emission of x-rays or Auger electrons. If an x-ray is emitted, the wavelength corresponds to that specific element's core-shell transition, and is thus characteristic for the element. In this way, by measuring the emitted x-rays, EDS provides elemental identification and composition quantification. The ratio of emitted x-rays to the sum of emitted x-rays and Auger electrons is called the fluorescence yield, where the fluorescence yield increases with the atomic number. Heavier elements are therefore more easily detected with EDS. An illustration of the four symmetrically arranged EDS detectors can be seen in Fig. 3.7. A second powerful spectroscopic technique is EELS. Electrons that are scattered inelastically will exit the specimen with energy less than when incident. By using an EELS spectrometer with a magnetic sector, a homogeneous magnetic field causes the electrons path to bend, and the bending curvature is energy dependent, dispersing the electrons by their energy onto the channels of a detector, as illustrated in Fig. 3.7. A spectrum can then be formed with energy-loss per channel. The EELS spectrum is usually divided into

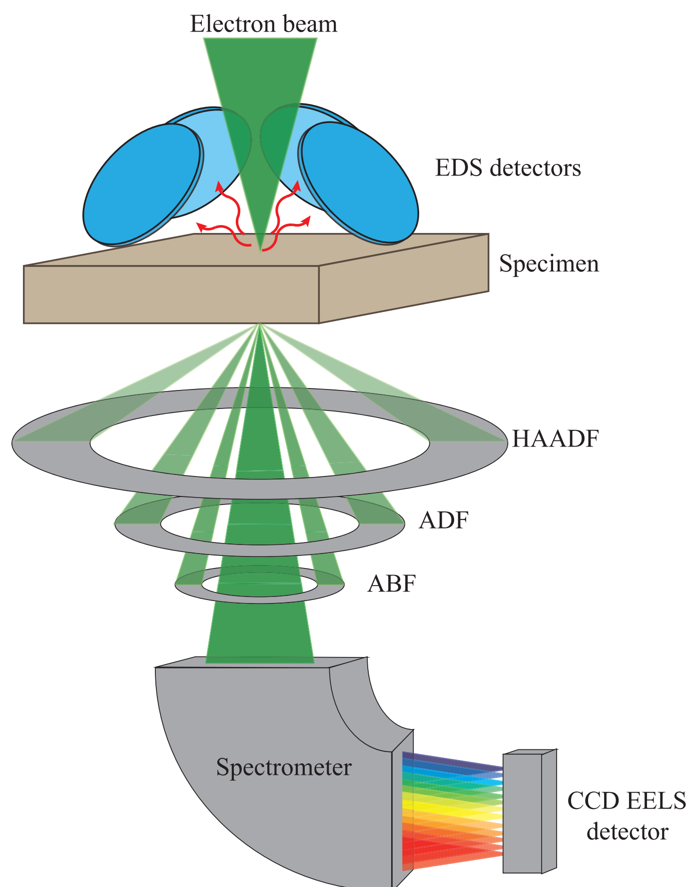

Figure 3.7: A schematic of a variety of detectors utilized in STEM imaging and spectroscopies. Above the specimen there are four symmetrically arranged EDS detectors. The elastically scattered electrons can be utilized for imaging with Annular Bright-Field (ABF), Annular Dark-Field (ADF) and High-Angle Annular Dark-Field (HAADF) detectors. ABF imaging is ideal for visualizing simultaneously heavy and light elements, ADF enables strain contrast, while HAADF is utilized for Z-contrast imaging. The energy loss of inelastically scattered electrons can be measured by EELS, using a spectrometer and a CCD EELS detector.

three regions, the zero-loss peak (ZLP) originating from the electrons that are elastically scattered (no energy loss), the core-loss region at energy-loss above 50 eV stemming from transitions between core-electronic states, and the low-loss region at loss-energies in between the ZLP and core-loss region, originating from valence states transitions, including excitons into the conduction band. From the EELS spectrum and the low-loss region, by subtracting the background originating from the tail of the ZLP, a fit can be made for the onset of energy loss, yielding for example the band gap of the material. Furthermore, EELS offers superior spatial resolution with respect to EDS, is ideal for the detection of light elements and enables access to bonding information.

In this work, the various measuring modes of TEM have been employed in order to determine compositional and structural effects of alloying ZnO and GaN, as well as band gap determination on a more local scale in the material. TEM EDS has, together with SEM EDS and SIMS measurements, given information about stoichiometry of the

different films. Furthermore, a thorough structural investigation has been performed, in order to examine the formation and evolution of different defect-types and localization of strain fields on the nanoscale. EELS was employed for band gap measurements on nano-scale, for a deeper investigation of the band bowing effect in the ZOGN alloys, as well as for investigating local chemical inhomogeneities and bonding re-arrangement.

The sample preparation for cross-section TEM investigations was done by mechanical grinding and polishing (Allied Multiprep). Final sample thinning was done by Ar ion milling using a GATAN PIPS II. Prior to the experiments, the specimens were plasma cleaned using a Fishione Model 1020. TEM and STEM imaging, as well as EDS and EELS analysis were performed using a FEI Titan G2 60-300 kV TEM, equipped with a monochromator, a CEOS DCOR probe-corrector, and Super-X EDS detectors. All structural and chemical investigations were performed at an acceleration voltage of 300 kV with a probe convergence angle of 21 mrad, and resulting spatial resolution of approximately 0.08 nm. For band gap measurements with EELS, an acceleration voltage of 60 kV was used to reduce the relativistic effects that might otherwise mask the band gap signal[29]. The EELS spectra were acquired using a GATAN GIF 965 spectrometer. Geometric Phase Analysis (GPA) was performed using the Gatan GMS software suite, to extract lattice phase maps and for the nanoscale localization of strained regions and dislocations.

3.5 Photoluminescence

A widely used optical characterization method in semiconductor physics is photoluminescence (PL). Luminescence is the emission of electromagnetic radiation, i.e. light, through recombination of excited charge carriers in a semiconductor material. These charge carriers can be excited by an electric current (*electroluminescence*), an electron beam (*cathodeluminescence*) or photons (*photoluminescence*). In PL, electrons and holes are generated by incident photons, e.g. by photon with energies above the band gap, creating electron-hole-pairs (EHP)s. As these EHPs recombine through different recombination mechanisms, the emitted photons are measured both in energy (origin of recombination) and in number (the intensity), using a detector. EHPs can decay through two main relaxation processes, namely a radiative- or a non-radiative recombination, depending on whether the occurring recombination is direct or indirect, respectively. If the transition is indirect, a change in the electrons momentum is necessary for the electron and hole to recombine, i.e. the recombination process must include a phonon.

There are several possible mechanisms for recombination in a material; The simplest mechanism is the band-to-band recombination between a free electron in the conduction band and a free hole in the valence band, emitting a photon with energy equal to or greater than the band gap. Excitons can also recombine causing luminescence. Free excitons (FX), or excitons bound to an electrically neutral or ionized impurity ($D^{0/+}X$ or $A^{0/-}X$ for an exciton bound to a neutral or ionized donor or acceptor, respectively) yields narrow luminescence lines, meaning that the spectral signatures are useful for identifying the recombining species[30]. Both band-to-band- and exciton emission constitutes what is called near-band-edge emission (NBE), whereas deeper defect levels in the band gap gives rise to deep level emission (DLE).

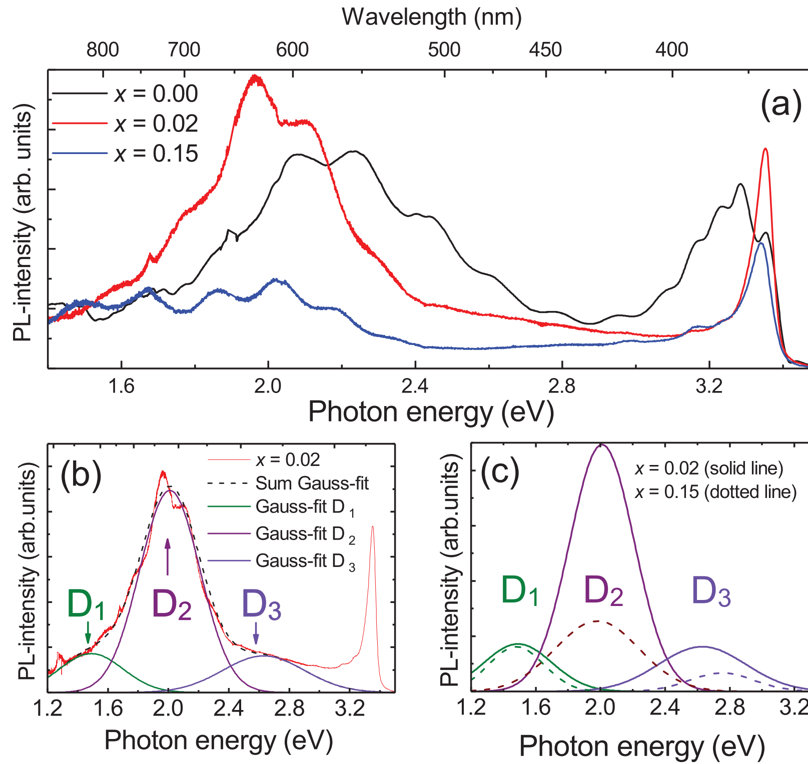

Figure 3.8: PL spectra recorded at 10K for ZOGN films with $x = 0$, 0.02 and 0.15 for investigation of NBE and DLE evolution with composition, x. (a) shows the full spectra, (b) a deconvolution of the broad band emission part of the $x = 0.02$ sample, and (c) the deconvoluted contributions for $x = 0.02$ and 0.15. The figure is from Olsen et al.[31].

Due to the strong exciton-related emission lines in ZnO, PL has been a widely used technique to determine optical properties in ZnO. The excitonic emission has been used to determine the band gap of the material, as well as the band gap dependence on temperature. One of the purposes of utilizing PL in this study was to measure the near-band-edge emission (NBE) of the alloys as a function of composition, as shown in Fig. 3.8 (a). If the band bowing effect of the alloys occurs due to the VBM being pushed upward in energy by orbital repulsion, the hypothesis was that the NBE would shift towards lower photon energies as a function of incorporated GaN content. Furthermore, by evaluating the deep-level contributions for different compositions, as shown in Fig. 3.8 (b and c), an indication of the evolution of defects could be obtained.

In this work, PL measurements were undertaken employing three different lasers; He-Cd laser (325 nm, nominal optical power approximately 5 mW, IK Series from Kimmon), Ar laser (488 nm, nominal optical power approximately 5 mW, from Melles Girot) and solid-state laser (405 nm, nominal optical power approximately 5 or 100 mW, from Oxxius). The PL emission was collected by a microscope, and afterwards, either directed into the imaging spectrometer (Horiba Jobin Yvon, iHR320) coupled to a CCD camera (Luca DL-658M EMCCD from Andor) or into an optical fiber connected to

a spectrometer (USB4000 from Ocean Optics) acting as two different detectors. The wavelength resolution in both cases was approximately 2-3 nm. Low-pass filters were used for the laser sources with excitation wavelengths of 488 nm and 405 nm in order to prevent scattered laser light from entering into the detection path.

3.6 Secondary Ion Mass Spectrometry

For characterizing the concentration of e.g. an impurity in a semiconductor, secondary ion mass spectrometry (SIMS) is one of the most powerful techniques, with the sensitivity down to parts per billion, or even below, and a depth resolution down to 2 nm. SIMS can be utilized to do three main types of measurements; mass spectrum over the probed area, depth profile of a specific element, and imaging. Independently of the measuring mode chosen, an ion beam, usually consisting of O_2^+ or Ce^+ ions, is incident on the sample surface, bombarding the top atom layers, causing atoms, and ionized species to be sputtered off the surface, making SIMS a destructive characterization technique. These secondary ions, forming a secondary ion beam, can then be accelerated towards analysers and detectors, as illustrated in Fig. 3.9. In a magnetic sector SIMS, the secondary ion beam goes through an electrostatic sector analyser, using two curved metal plates at different potential for energy filtering. After exiting the electrostatic sector analyser, the secondary ion beam enters a magnetic sector analyzer, where a perpendicular magnetic field causes the pathway of the ions to bend. The curvature of the ions pathway is mass dependent, thus the magnetic sector analyser acts as a mass filter. By carefully adjusting the magnetic field, only ions with a specific mass will pass the analyzer slit (exit slit). A mass spectrum can be formed by slowly varying (e.g. increasing) the magnetic field. Hence, the elements that are allowed to pass the analyzer slit will change from light to heavier elements. A depth profile on the other hand, is formed by keeping the magnetic field constant, allowing only a certain element to pass, while the primary ion beam sputters through the thickness of the film. The detector thus measures intensity as a function of time, which again can be converted into concentration versus depth profiles using standards and measuring the crater depth.

The amount of sputtered materials mainly consist of neutral atoms. Thus, the fraction that is ionized is low[32], and it is only these ions that can be extracted and measured in the mass spectrometer. The intensity of ions of material A, I_A, that reach the detector is dependent on several factors, including the intensity of the primary ion beam, I_P. I_A also depend on the sputter yield, Y, which is the number of ejected atoms per incident ion. Furthermore, the measured intensity depends on the ionization probability of the element A, γ_A. To enhance the ionization probability for more electronegative elements, Cs^+ as primary ions are usually employed, and oppositely, O_2^+ primary ions for electropositive elements. In addition, I_A depends on an instrument transmission constant, T, and the concentration of the element, C_A. All in all, the intensity of I_A can be expressed as:

$$I_A = I_P Y \gamma_A T C_A. \tag{3.8}$$

By measuring the depth of the sputtered crater and assuming uniform and time-independent erosion rate, the sputtering time can be converted to depth. Since both

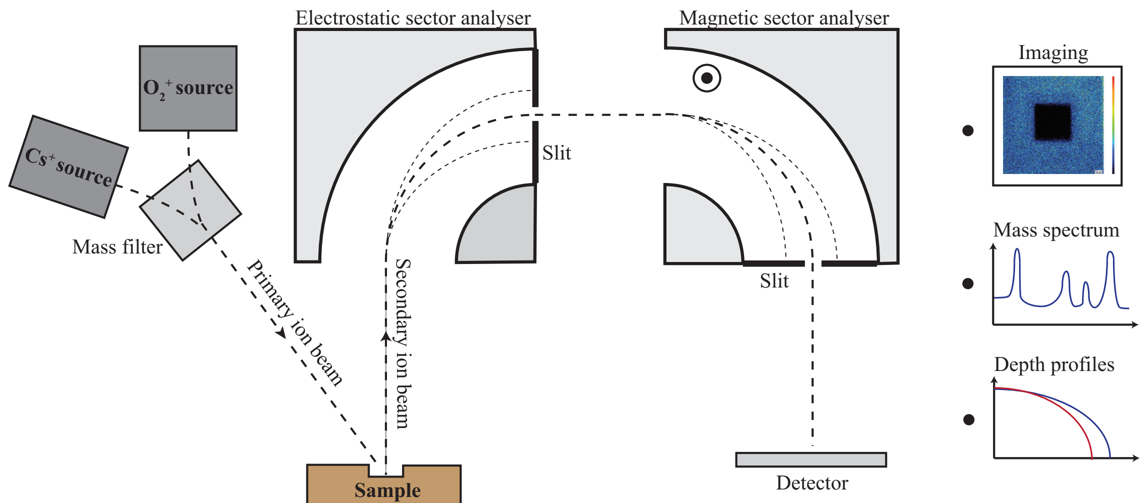

Figure 3.9: A simplified schematic of the SIMS instrument used in this study, including the three most used modes of operation; mass spectra, depth profiles and imaging.

the concentration of the material (C_A) and the ionization probability is unknown, the measured intensity can only be converted to concentration by measuring a reference sample with a known doping concentration at a certain depth, usually obtained by ion implantation. The reference sample is measured under the same conditions as the sample under investigation, meaning that it gives a good measure to the remaining proportionality factors, i.e. I_P, Y and γ_A as well. Hence, I_A as a function of time can be converted to C_A as function of depth, resulting in a depth profile of material A.

SIMS require high vacuum in the sample chamber, typically in the range of 10^{-9} mbar, to ensure a sufficiently large mean free path of the ions. In addition, the technique requires conductive samples, as charged particles (usually positive) enter the sample form the primary beam. The sputter process also results in ejection of electrons, in addition to the secondary ions and neutral atoms and molecules. In the case of an insulating sample, the ejection of secondary ions and electrons leads to a build-up of localized positive charge at the surface which will affect the energy of the secondary ions and therefore transmission of the secondary ion beam may be lost. For semi-insulating samples, this positive surface charge can, to some extent, be compensated by utilizing an electron gun.

In SIMS, the depth resolution is directly dependent on the energy of the primary ions, since the ions mix the lattice atoms close to the surface, resulting in an almost amorphous layer. With higher incident energy, the ions will break the lattice and displace lattice atoms deeper into the film. Secondary ions that are sputtered from the surface layer may have originated from any depth of the mixing region, meaning that the thickness of this amorphous layer determines the depth resolution.

In this work SIMS measurements, both mass spectra and depth profiles, were employed. Mass spectra measurements were undertaken for impurity identification, and depth profiles for Ga and N were obtained in order to ensure that the Ga and N were incorporated uniformly with respect to the film thickness during growth. The instrument used in this work was a magnetic sector SIMS (Cameca IMS-7f), with either 15 keV

Ce^+ ions or 10 keV O_2^+ ions as the primary beam. The depth of the sputtered crater was measured using a Veeco Dektak 8 Stylus Profilometer. Ga and N implanted ZnO samples were used to convert the recorded secondary ion intensities to concentration.

3.7 Rutherford Backscattering Spectrometry

Rutherford backscattering spectrometry (RBS) is a non-destructive characterization technique utilizing an ion beam to measure the atomic distortion in a material, determine mass of the elements and their distribution in a material. A monoenergetic MeV ion beam (usually consisting of H^+ or He^+ ions) is incident on a material surface. Several interaction mechanisms between the incident ions and the host atoms may occur, including elastic scattering at the surface, ionization and excitation of host atoms, and backscattering at various depths. The fraction of ions that undergoes elastic backscattering can be measured by a detector, in terms of energy and backscattering angle, in order to calculate the mass and determine the element causing the backscattering event. Ions backscattered from deeper into the materials thickness exit the material with lower energy, compared to those backscattered near the surface, since they must transverse through the material twice, losing energy to Coulombic interactions. In this way, the energy difference between ions scattered from the surface and from a specific depth can be used to determine this thickness, utilizing the backscattering energy loss factor[32] (eV/Å) which is tabulated for pure element samples. RBS is hence a powerful method for measuring thicknesses, depth profiles and compositions.

RBS measurements can be carried out in several modes, where the two most important ones when investigating the crystal structure of a material is RBS in random mode (RBS) and in channelling mode (RBS/C). RBS/C differs from random mode in the way that the ion beam is incident along a major crystal orientation, resulting in significantly reduced backscattering yield, and this mode of operation can give information about lattice defects, dislocations and crystal distortion, when compared to random mode. An example of comparing RBS/C to RBS spectra is when calculating the minimum surface yield. The backscattering yield at the surface measured by RBS/C is compared to RBS, where a minimum surface yield of $\sim$2% is anticipated for single crystals of high crystalline quality[33].

In this work, RBS measurements, both in random- and channelling mode, were employed to measure the effects of composition and post-deposition annealing on the displacement in the films, as well as minimum surface yield. The RBS measurements undertaken in this study were carried out employing a Tandem ion accelerator (National Electrostatics Corporation), with an ion beam consisting of 1.62 MeV He^+ ions. The backscattered beam was analyzed using a solid-state detector at an angle of 165° with respect to the incident beam. RBS/C measurements were done along the [0001] direction of the samples.

3.8 Density Functional Theory

In order to obtain a deeper understanding about material properties, experimentally obtained results are often compared to theoretically predicted results utilizing density

functional theory (DFT). DFT allows for investigation of the electronic structure in a material using computational modeling, yielding both structural, electrical and optical information about a material, e.g. formation energies, bond lengths, band gap energies and band structure.

The basis of DFT, established in 1964 by P. Hohenberg and W. Kohn and their two famous theorems[34] as well as the Kohn-Sham equation introduced in 1965[35], is that the ground-state energy, and all other ground-state properties of a many-electron system are functionals of the ground-state density, n_0. In addition, there exists an exact ground-state energy, $E[n_0]$, that is the global minimum for any external potential $V(\mathbf{r})$. Moreover, the density that minimizes the energy functional is the exact ground-state density, n_0. The Kohn-Sham equations can be written in the form

$$\left[-\frac{\hbar^2}{2m}\nabla^2 + V(\mathbf{r}) + V_H(\mathbf{r}) + V_{xc}(\mathbf{r})\right]\psi_i(\mathbf{r}) = \varepsilon_i\psi_i(\mathbf{r}) \tag{3.9}$$

and includes three potentials; the interaction between an electron and the collection of atomic nuclei (V), the Hartree potential describing the repulsion between a single electron and the total electron density (V_H), and the exchange-correlation potential which is the collection of terms that have not been considered in the former potentials (V_{xc}). The exchange-correlation potential is a functional derivative of the exchange-correlation energy;

$$V_{xc}(\mathbf{r}) = \frac{\delta E_{xc}(\mathbf{r})}{\delta n(\mathbf{r})}. \tag{3.10}$$

The total energy of the system must be calculated iteratively, where an initial guess of the electron density, $n(\mathbf{r})$, is made. The single-particle wave functions are calculated by solving the Kohn-Sham equations (3.9) using $n(\mathbf{r})$, which again will provide a calculated electron density from $n_{KS}(\mathbf{r}) = \sum_i |\psi_i(\mathbf{r})|^2$. If $n_{KS}(\mathbf{r})$ differs from $n(\mathbf{r})$, then $n_{KS}(\mathbf{r})$ is used to calculate new single-particle wave functions, and thus a new electron density. This process is repeated until $n(\mathbf{r})$ has converged, and is then treated as the ground-state electron density, n_0. From n_0, the ground state energy, $E[n_0]$, can be calculated.

The only unknown term for an exact calculation of $E[n_0]$ is thus E_{xc}. Several approximations for E_{xc} have been developed in order to obtain a $E[n_0]$ as close to the true value as possible. The local density approximation (LDA) uses the known exchange-correlation potential of an uniform electron gas, i.e. $n(\mathbf{r})$ is constant, to calculate $E[n_0]$. The generalized gradient approximation (GGA) uses the local density and its gradient to approximate E_{xc}, where information about the gradient can be included in the GGA functional different ways, e.g. using the Perdew-Burk-Ernzerhof functional (PBE)[36, 37]. DFT at the LDA and GGA levels, has been successful in describing ground-state properties such as structural properties and total energies, whereas the draw-back is a systematical underestimation of the band gap of semiconductors.

Several alternatives have been developed to circumvent the underestimation of the band gap. Hybrid functionals, which include a certain amount of the exact Hartree-Fock (HF) exchange potential added to the remaining part of the exchange-correlation

potential from GGA or LDA functionals, have been found to yield more accurate band gap energies. An example of such a hybrid functional is the HSE hybrid functional, that includes the screened HF exchange to the PBE functional[38]. Alternatively, the Green's functions approach can be utilized in order to calculate excited state properties. The energy of a quasi-particle is determined directly by calculating the contribution of the dynamical polarization of the surrounding electrons, whereas the self-energy is formulated in terms of a screened Coulomb potential W, thus naming it the GW method[39]. The GW method allows for calculation of excited states, and thus optical properties, yielding band gap energies much closer to the experimentally obtained values, compared to DFT at the LDA and GGA levels.

Chapter 4

The $(ZnO)_{1-x}(GaN)_x$ Alloys

The ZOGN alloys, where the host materials are two wide-band gap semiconductors with band gap energies corresponding to the UV-range of the spectrum (3.37 eV and 3.51 eV for ZnO and GaN, respectively), has been found to yield absorption in the visible range of the spectrum, with apparent band gap energies down to $\sim$2.3 eV. This band gap reduction has made the ZOGN material a strong candidates for water-splitting applications under visible light, as well as an intriguing material for use in other optoelectronic applications including solar cells, photodetectors and light emitting diodes (LEDs). However, many of the potential applications depend on the alloys to be grown as highly crystalline thin films with tunable structural, optical and electrical properties.

4.1 GaN and ZnO

Extensive research has been devoted to GaN, with a band gap energy of 3.51 eV, due to its potential for a wide range of applications, including ultraviolet (UV) detectors and emitters, and high power electronics. One of the main obstacles for realizing the true potential of GaN, especially for optoelectronic applications, has been to control the electrical conduction. The native *n*-type conductivity has been the topic of extensive research, and nitrogen vacancies[40, 41] as well as impurities incorporated during growth as Si and O, on substitutional site for Ga and N, respectively[42, 43], have been accepted as the main donors, contributing to the *n*-type conduction. Due to this natural *n*-type conductivity, and the ability of H to passivate acceptors[44], low resistive, *p*-type conduction was extremely challenging to obtain. Stable *p*-type conductivity for GaN was realized using Mg-doping by Amano et al.[45]. As a result, Amano was together with Akasaki and Nakamura, awarded the Nobel Prize in Physics in 2014 for inventing the blue LED, based on GaN alloys[4].

ZnO is another compound semiconductor with high potential for optoelectronic applications, mainly due to the band gap energy of 3.37 eV combined with a large exciton binding energy of 60 meV, i.e. substantially larger than that of GaN. Compared to GaN, ZnO has also faced similar challenges as the natural *n*-type conductivity. Zn interstitials and O vacancies[46, 47] have been identified as donors in ZnO, and hydrogen, which is commonly known to counteract the prevailing conductivity for semiconductors, exclusively acts as a donor in ZnO[48]. Oppositely to GaN, stable and low resistive *p*-type conduction in ZnO has, despite extensive research, still not been realized.

ZnO and GaN are similar compound semiconductors in several ways, including sharing the hexagonal wurtzite crystal structure as the thermodynamically stable phase at ambient conditions, similar lattice constants, i.e. a = 3.247 Å (3.189 Å) and c = 5.204 Å (5.186 Å) for ZnO (GaN) [49, 50], and similar band gap energy at 3.37 eV and

3.51 eV for ZnO and GaN, respectively. An important advantage for ZnO over GaN is the excitonic optical features due to the large excitonic binding energy, in addition to more inexpensive methods of fabricating high crystal quality bulk material. Thus, ZnO has an intriguing potential to realize near-UV light emission if a stable p-type conduction can be obtained. On the other hand, ZnO is already used in applications as a transparent conductive oxide (TCO) for displays and solar cells due the high charge carrier concentration obtained by e.g. Al-doping, while maintaining the optical transparency. GaN on the other hand is a more mature material for use in optoelectronics, and is used commercially in LEDs both as pure material and as alloys. AlGaN alloys have band gap energy tunable by composition in the range of 3.4 eV - 6.1 eV, i.e. in the UV-range, making the alloys applicable for e.g. solar-blind UV detectors.

High quality bulk material of ZnO and GaN is challenging to fabricate with defect and dislocation densities sufficiently low for use as substrates in devices. Therefore, the costly fabrication methods of GaN, the difficulty of obtaining low impurity concentrations, and lower quantity of fabricated wafers (compared to e.g. Si), makes the substrates unattractive for commercial purposes. This is especially true if compared to other substrate materials widely used in thin film industry including silicon, sapphire and quartz. On the other hand, it is also significantly more difficult to fabricate high quality GaN bulk materials than ZnO. Growth of high quality bulk GaN includes expensive methods like metal organic chemical vapor deposition (MOCVD) and hydride vapor phase epitaxy (HVPE). For these methods, issues as high growth temperatures and pressures, in addition to low growth rates and limited scaleability are essential. ZnO bulk material of high crystal quality is usually fabricated using the hydrothermal method, where high temperature and pressure still are significant issues, but compared to GaN, ZnO is significantly more inexpensive to fabricate. Due to the difference in availability of high quality bulk materials for ZnO and GaN, high quality ZnO substrates have been to a large degree employed to grow epitaxial GaN. This, since the lattice mismatch is significantly lower compared to e.g. sapphire.

4.2 The Band Bowing Effect

The band bowing effect occurs when two semiconductor materials are alloyed and the band gap energy of the alloys deviates from the linear relationship between band gap variation and the ratio between the two host materials. As a result, the effect can be considered as a deviation from Vegard's law, which predicts a linear variation in both band gap energy and lattice constants between the host materials in alloys[51]. This deviation from the linear variation is often described by a bowing parameter, *b*;

$$E_g(x) = E_g^A \cdot (1-x) + E_g^B \cdot x - b \cdot x \cdot (1-x), \tag{4.1}$$

where $E_g(x)$ is the band gap of the alloys for a composition, x. E_g^A and E_g^B are the band gap energies of the host materials, A and B, respectively, and *b* is the bowing parameter.

The band bowing effect is observed in several material systems, including alloys substituting the cation, for instance in nitrides where InN is alloyed with AlN and GaN[52, 53] and oxides where the cation in ZnO is substituted with Mg or Cd[54–56]. In addition, alloys where the anion is the element of substitution, e.g. ZnO where O is

substituted with S or Se[57, 58] also yield band gap bowing. In the case of these nitride- and oxide alloys, the difference in band gap energy between the host materials may be significant, e.g. E_g^{InN} (0.65 eV) and E_g^{AlN} (6.02 eV), implying that the effects of the band gap energy deviating from the linear variation as function of composition are limited. The ZOGN alloys differs from the material systems mentioned above since both the cation and anions are subject to substitution, i.e. isoelectric alloying. Interestingly, the observed band gap reduction for ZOGN yields band gap energies significantly lower than the binary hosts, well into the visible part of the spectrum. Hence, contrary to alloy systems as InN-AlN and ZnO-MgO, the ZOGN alloys yields band gap energies in a completely different range of the optical spectrum solely as a result of the band bowing effect.

Although the band gap energies of ZnO and GaN are fairly similar, the energy position of the valence- and conduction bands with respect to the vacuum level is different, resulting in the valence band maximum (VBM) of GaN being about 1 eV higher in energy than that of ZnO[59, 60]. Several hypothesis have been proposed for the cause of the band bowing effect, mainly based on theoretical calculations. Repulsions between the N 2*p* and Zn 3*d* orbitals within the ZOGN valence band have been proposed to cause an upward shift in the VBM[61–65], where a gradual band bowing occurs, often described by the bowing parameter, b, as in Eq. (4.1). Opposing to the orbital repulsion hypothesis, the band bowing effect has been proposed to be composed of different compositional regions with different band gap reduction. Two regions close to the host materials, A and B, where x is either low or high, and the one material acts mainly as defects in the other material's matrix. These two regions have strong band gap reduction which is explained by the band anticross model (BAC)[66, 67]. The two regions are separated by a wider region of compositions where the material acts more like an alloy, and the band gap is significantly less sensitive to compositional variations, i.e. as in Eq. (4.1) with a small b. Other hypotheses for explaining the band gap bowing in alloys have also been put forth, e.g. type-II band alignment.

In addition to the band gap being dependent of the composition, x, the atomic ordering for a specific x also affect the band gap. It has been found that the band gap depends on if the alloy is a random alloy or if there is presence of clusters of the binary host materials, either on nano- or micro scale. In this respect, the term cluster formation implies an increase in Ga-N bonds, as described for the ZnO-InN alloy by Dou et al. [68]. For the ZOGN alloys, cluster formation has been found energetically favourable[64], as more Ga-N bonds yield a more stable configuration[63, 64, 69, 70], and the formation of neutral and valence-conserving larger complexes driven by the octet rule for the atoms has been proposed as an explanation[71]. For the ZnO-InN alloys, InN clusters in the ZnO matrix was found to yield stronger band gap reduction compared to that of a random alloy[68]. For the ZOGN alloys on the other hand, theoretical calculations suggesting that the band bowing effect is caused by orbital repulsion, have found that clustering results in a band gap blueshift[61, 64, 69], where this weaker band gap reduction is explained by the fact that a random alloy would increase the number of Zn-N bonds causing stronger band gap reduction[61]. Oppositely, Maeda et al. experimentally found a band gap redshift when subjected to heat treatment[72].

4.3 The $(ZnO)_{1-x}(GaN)_x$ Alloys in Hydrogen Production

Hydrogen production through overall water splitting has been a driving force for developing the ZOGN alloys. Splitting water molecules into oxygen and hydrogen molecules cost energy, and in order to make hydrogen production a green alternative, this energy must be harvested from renewable energy sources such as solar or wind. Overall water splitting by solar energy utilizes e.g. a photocatalyst composing of a light-harvesting semiconductor material and a cocatalyst[73]. The semiconductor is responsible for generating electrons and holes through photo-excitation, before these charge carriers diffuse independently to the surface of the particle or film. The cocatalyst, a material is usually synthesized as nanoparticles on the semiconductor, and has the main function of providing redox reaction sites. The electrons and holes contributes to splitting water molecules through redox reactions, i.e.; $2H^+ + 2e^- \rightarrow H_2$ and $H_2O + 4h^+ \rightarrow 4H^+ + O_2$, respectively. It is evident that the material must meet specific requirements in order to maximize the water splitting efficiency, including; suitable band edge positions for overall water splitting, a band gap lower than 3 eV for harvesting the visible part of the spectrum, and high crystalline quality to minimize electron-hole recombination[73, 74].

The ZOGN alloys potentially meets all the mentioned criteria, and Maeda et al. were the pioneers in utilizing the band bowing effect observed in the ZOGN alloys for reducing the band gap to harvest the visible part of the solar spectrum. They found that the hydrogen conversion efficiency was higher than conventional oxide photocatalysts under visible light[5, 6, 75–77]. By nitridation of a mixture of Ga_2O_3 and ZnO at high temperatures, a solid solution of ZOGN with $x \geq 0.75$ was synthesized with different cocatalysts, where the ZOGN band gap was reduced to $\sim$2.6 eV. Later, the ZOGN alloys gained popularity for overall water splitting, where Mapa et al. reduced the ZOGN band gap to $\sim$2.5 by synthesizing a ZOGN solid solution with $x \leq 0.15$[78], Chen et al. used the high-pressure, high-temperature synthesis to fabricate ZOGN solid solution samples over the whole composition range, where $x = 0.51$ was found to absorb light with wavelength down to 500 nm, yielding a band gap reduction to $\sim$2.5 eV[79]. However, one major drawback of the ZOGN alloys synthesized as powder samples, is the relatively high recombination rate of electrons and holes, preventing high efficiency of the overall water splitting.

The overall surface area and crystalline quality determines the photocatalytic activity of the material. A larger surface area results in a higher number of reaction sites, whereas with higher crystalline quality, fewer defects and dislocations can act as recombination centres for the photo-excited charge carriers in the semiconductor. In order minimize the recombination rate in the photocatalyst, the alloys have been synthesized as nanostructures. Alloys with increased crystalline quality, compared to powder samples, were thus synthesized as both nanowires[80–83] and nanocrystals[84]. Furthermore, by synthesizing as nanowires, the alloys can be employed as photoanode in overall water splitting[81, 83]. It may be noted that an additional potential application of ZOGN alloys is photodegradation of organic materials[85, 86], which also utilizes the photocatalytic performance of the material.

4.4 Potential of the $(ZnO)_{1-x}(GaN)_x$ Alloys

In order to utilize the promising functional properties ZOGN in optoelectronic applications, a thorough investigation of the alloys and the functional properties are required. The alloys have been synthesized as powder, nanocrystals and nanowires, and has in many ways been optimized for hydrogen production through overall water splitting, as discussed in the previous section. For optoelectronic applications, on the other hand, high crystal quality, tunable electrical and optical properties are of utmost importance, and the fabrication method should be easy to scale up. In addition, the thin film deposition must be a viable and effective technique for a wide range of applications, such as solar cells, photodiodes and sensors.

Depositing a material as thin films is an effective, relatively inexpensive and readily up-scalable method of synthesizing highly crystalline materials. In addition, as for other synthesis routes, the parameter space for altering the electrical, optical and structural properties is wide. Several reports of thin film deposition of ZOGN have previously been reported in the literature; Shet et al. deposited polycrystalline ZOGN thin films using RF magnetron sputtering, although significant band gap reduction was not achieved (only down to about 3.0 eV - 3.1 eV) and the crystallinity of the films was relatively poor[87, 88]. Highly crystalline thin films with much larger band gap reduction were later deposited by Yang et al. utilizing pulsed laser deposition (PLD)[89]. However, the number of reports on thin film ZOGN alloys is scarce in the literature. Thus, the potential for growing alloy thin films using an industrial technique as sputter deposition is substantial.

The majority of the reported work on ZOGN, independent of synthesis and application, has been focused on the GaN-rich side of the compositional regime. Thus, there is a potential for exploring advantages of incorporating GaN into ZnO. In addition to Zn being more earth abundant and cheap to produce compared to Ga, Huda et al. used theoretical calculations to show that the band bowing effect in ZOGN is asymmetrical, i.e. a stronger band gap reduction is obtained by introducing GaN into ZnO than the opposite[90]. Furthermore, epitaxial ZnO can be achieved at relative low temperatures using magnetron sputtering[91], indicating that highly crystalline thin films may be easier to achieve, and thus more easy to scale up.

To fully exploit the potential of the ZOGN alloys in both optoelectronics and hydrogen production, an understanding of the mechanisms governing the band bowing effect for the alloys is a prerequisite. As mentioned in the section introducing the band bowing effect, there are various reports explaining the band gap reduction in ZOGN with orbital repulsion, defect bands and band alignment. Furthermore, the number of experimental reports investigating the mechanisms evolving the band gap in ZOGN is scarce in the literature, where the explanations put fourth are dominated by theoretical calculations. These mechanisms may be crucial in exploring the potential for use in optoelectronics, where achieving *p*-type conduction by making deep acceptors more shallow, or tune the emission of the alloys as a function of composition still have not been reported. In other words, there is need for a deeper investigation regarding the band bowing effect, connecting experimental results with theoretical predictions, in order to determine the mechanisms governing the band bowing effect.

Chapter 5

Summary of Results

This chapter serves to summarize the main results obtained in this study in the broader context that is this thesis. In order to potentially exploit the potential of the ZOGN alloy for optoelectronic applications, the interplay between the structural and optical properties of the alloy thin films must be understood and controlled. The alloy composition, as well as structural disorder have been found to affect the band gap energy of the alloy, and the mechanisms governing the band bowing effect must be investigated, combining experimentally obtained results with computational simulations. These band bowing investigations may also be applicable for other alloys as well, as the vast majority of the e.g. LED market today is based on semiconductor alloys. Furthermore, the electrical properties of the thin films must be controlled, both in terms of composition and structural properties, as well as the band bowing effect, if the ZOGN alloys is to be utilized in optoelectronic applications as e.g. LEDs, photodetectors and solar cells.

5.1 Structural Properties of the $(ZnO)_{1-x}(GaN)_x$ Alloys

Highly crystalline thin films of ZOGN with GaN content ranging up to $x = 0.20$ were deposited using magnetron sputtering. The thin films were found to be stoichiometric and by employing SIMS both the Ga- and N concentrations were found to be relatively uniform throughout the thickness of the films. A fully detailed table with growth parameters, as well as SEM EDS results showing the Ga and N content, can be seen in Table 5.1.

The high crystal quality was determined using XRD, RBS, HR-(S)TEM and Electron Diffraction. The alloys were found to yield columnar growth along the c-axis, following the general tendency for ZnO to grow faster along the c-axis, where some of the grains exhibited small twist rotations around the same axis. For the as-grown ZOGN thin films, XRD analysis yielded strained films, with increasing tensile strain along the *c*-axis with increasing *x*, as seen in Figure 5.1. This trend is opposite to what is expected by Vegard's law[51], predicting a linear decrease in both lattice parameters and band gap energy when increasing *x* in the ZOGN alloys. The lattice constants of the $x = 0.15$ film extracted by electron diffraction patterns in TEM, corroborates the increase in lattice constants with respect to the nominal values of ZnO, where the *c*- and *a*- lattice parameter were found to be 5.224 ± 0.006 Å and 3.252 ± 0.004 Å, respectively. The films reported in Paper I were found to be highly crystalline and with no secondary phases for $x < 0.2$. TEM investigations showed that the ZOGN films exhibited a good heteroepitaxial relationship with the c-Al_2O_3 substrate, with an alloy unit cell rotated 30° with respect to that of the substrate, which is favourable due to a reduced mismatch between the film and the substrate. These so-called "aligned domains" that were found to be dominant in our films are common for ZnO films deposited on c-Al_2O_3 due to the same reason of film-substrate mismatch reduction.

Composition	Ga [at%]	N [at%]	ZnO [W]	GaN [W]	Ar [sccm]	N_2 [sccm]	Time [Minutes]	Thickness [nm]
$x = 0.00$	0	0	30	0	12.5	0	1440	1380
$x = 0.02$	1.1 ± 0.1	3.0 ± 0.3	30	7	12.5	0.7	1440	1110
$x = 0.07$	3.5 ± 0.2	3.4 ± 0.3	30	10	12.5	0.7	1440	1690
$x = 0.15$	7.5 ± 0.4	5.7 ± 0.4	30	20	12.5	5	1200	1330
$x = 0.19$	9.5 ± 0.5	6.5 ± 0.5	20	20	10	20	1800	1880
$x = 0.20$	10.0 ± 0.5	7.9 ± 0.5	30	30	10	20	1200	1290

Table 5.1: Growth details for ZOGN films with $x \leq 0.2$. The composition, x, was taken as twice the measured Ga content. Both Ga- and N content was measured using SEM EDS, whereas TEM EDS and SIMS measurements corroborates the measured values. The listed thicknesses and growth times are from the films used in papers I, II and III. As for papers IV and V, thinner films with thicknesses of approximately 300 nm were used.

In terms of structural distortion in the as-grown ZOGN films, TEM investigations yielded a high density of threading dislocations for the $x = 0.15$ sample. From XRD analysis, the peak full-width at half maximum (FWHM) of the (0002) reflection measured with rocking curve scans, was found to increase with GaN content, x, interpreted as an increase in dislocation density with x. RBS measurements for the as-grown films corroborates the increase in structural distortion with increasing GaN content, where the minimum surface yields were calculated to be $\sim$23% and $\sim$29% for $x = 0.02$ and 0.15, respectively.

The investigations presented in Paper V showed for the $x = 0.15$ film, an interfacial area between the film and the c-Al_2O_3 substrate was formed. The interfacial area was approximately 50 nm thick and was more Ga-rich than the film (about 20% compared to 15% measured in the bulk of the film). In addition, extra diffraction reflections revealed the presence of nano-sized zinc blende (ZB) phases with an average size of $\sim$5 nm. A possible cause for the formation of ZB, is agglomeration of point defects in the basal planes, forming stacking faults. Indeed, the accumulation of stacking faults have previously been proposed to cause formation of ZB phase[92]. The possible explanation for the nano-sized ZB phases being formed in the interface layer, and not in the bulk of the film, is internal stresses due to grain misorientations leading to phase transformations to minimize the strain.

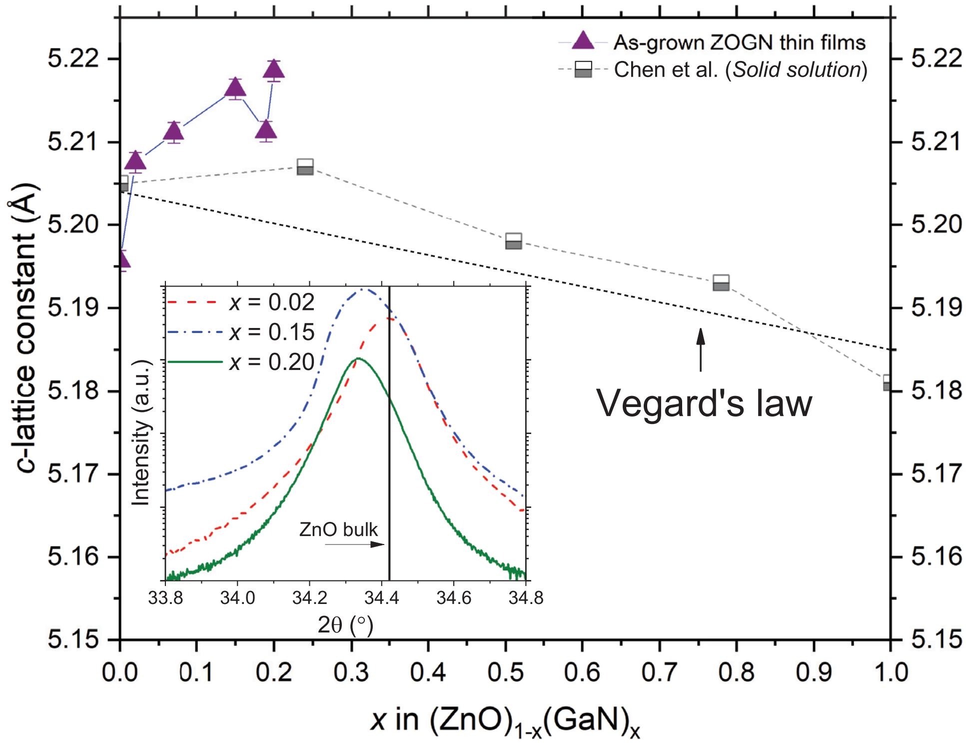

Figure 5.1: The c-lattice constant for as-grown ZOGN films as a function of composition, x. The measured lattice constants (purple triangles) are compared to the lattice constants obtained by Chen et al. [79], and the dotted line represents Vegard's law. The inset shows the (0002) peak for $x = 0.02$ (dashed line), 0.15 (dashed and dotted line) and 0.20 films (line), while the vertical line represents the peak position of bulk ZnO. Data from Paper I.

5.2 Effects of Thermal Annealing

Magnetron sputtering is a physical deposition method involving sputtered atoms and molecules incident on a substrate, thus the sputtered films are rarely, if ever, in thermal equilibrium at typical deposition temperatures. Indeed, strain is observed in the films, and can partly explain the deviation from Vegard's law, as stated in the previous section. In order to bring the sputtered thin films closer towards thermal equilibrium, post-deposition isochronal anneals at 600°C, 700°C and 800°C in nitrogen flow were employed. However, cluster formation has been predicted to energetically favourable and may affect the optical properties, i.e. the band bowing effect. Hence, post-deposition annealing is a effective method to investigate the evolution with respect to structure and optical properties.

For all the ZOGN alloys, a significant reduction in c-lattice constant was observed with increasing annealing temperature (Paper II), approaching the values predicted by Vegard's law. The relaxation of the crystal structure and reduction in tensile strain along

the *c*-axis can be explained by increased atomic mobility, giving an increased probability of finding a more energetically favourable configuration. Furthermore, a reduction in threading dislocation density was found from the TEM analysis, as well as an increase in the width of the grains, with mean values of 20 nm for as-grown and 50 nm after the last annealing step at 800°C. The increase in columnar grain size and reduction in threading dislocation density can be attributed to grain coalescence during annealing. An overall increase in crystalline quality was thus found with post-deposition annealing.

Although a substantial improvement in the crystalline quality was observed by post-deposition heat treatments, nano-sized nitrogen-rich voids along grain boundaries and threading dislocations were found to form after the annealing steps (Paper IV), as seen in Fig. 5.2. The voids had a diameter of 5 nm - 10 nm, and from STEM investigations, it was evident that the voids were not amorphous areas, and in fact no structural change deviating from the hexagonal stacking sequence along the *c*-axis was measured. The nitrogen contained in the voids was compared to both a GaN reference and N_2 reference, as shown in Fig. 5.2 (d), and it was concluded that the N was in molecular form. Furthermore, a time-resolved electron beam irradiation experiment yielded rapid removal of N_2, by drilling a hole in the void using the electron beam, and simultanously recording an EELS spectrum. A possible cause for the formation of nano-sized voids during annealing is the agglomeration of Zn-vacancies and Ga-vacancies (V_{Zn} and V_{Ga}) present in the film at grain boundaries and threading dislocations, whereas trapping of molecular nitrogen is attributed to the low stability of N substitution on O sites. Indeed, theoretical calculations predict O-sites to be energetically unfavourable for N_2[93] whereas V_{Zn} can be occupied by molecular nitrogen[94]. The formation of N_2 bubbles has also been proposed to be a result of thermal annealing[95] in ZnO, where N moves from substitutional O sites to form bubbles of molecular nitrogen.

In addition to voids, nano-sized GaN clusters are probable to form during the annealing steps. In Paper II, DFT calculations using the PBE functional showed that the change in formation energy decreases with increasing number of Ga-N bonds, and is shown in Fig. 5.3 (a), i.e. the total energy of the system is lowered with more Ga-N bonds, compared to Ga-O and Zn-N bonds. This reduction in total energy indicates that Ga-N cluster formation, i.e. an increase in Ga-N bonds as discussed by Dou et al. for the ZnO-InN alloys[68], is energetically favourable. Interestingly, as shown in Fig. 5.3 (b), a systematic broadening of the (0002) reflection was observed for all alloy compositions with thermal annealing, whereas the ZnO-only film became narrower with annealing, indicating increased overall crystal quality. Hence, despite the average meso-scale enhancement of the crystal quality of the films (increase of grain size and threading dislocation reduction), the systematic broadening of the (0002) reflection in XRD can be attributed to an increase in Ga-N bonds.

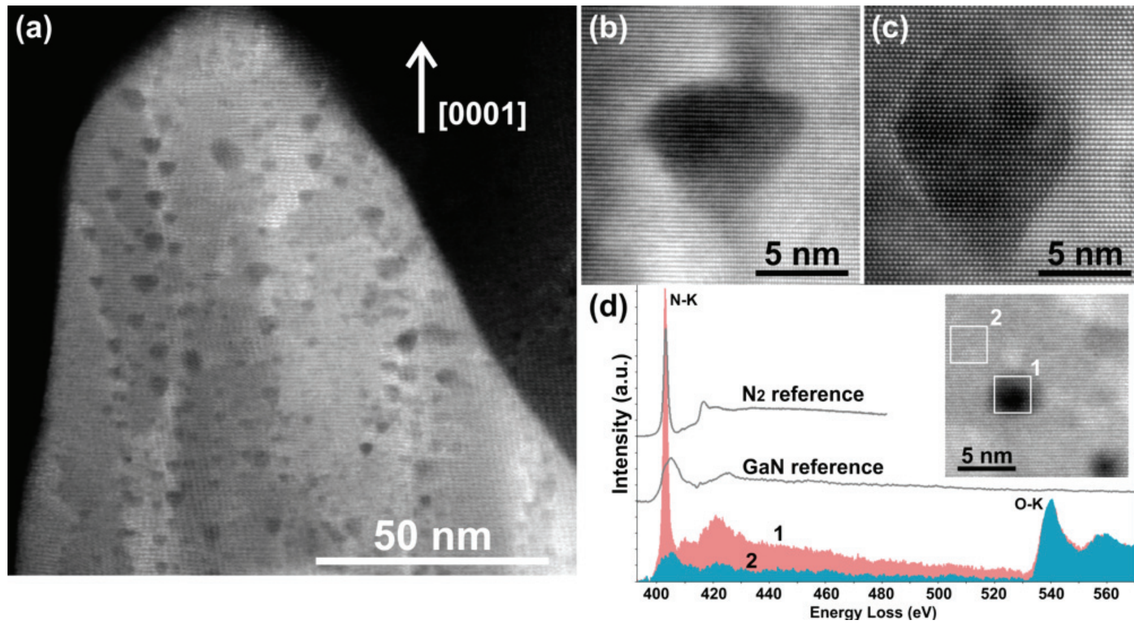

Figure 5.2: (a) ADF-STEM image, showing formation of voids along grain boundaries and threading dislocations. (b)-(c) High-resolution ADF-STEM images along the [$1\bar{1}00$] and [$11\bar{2}0$] zone axes, respectively, illustrating highly faceted voids. (d) EELS-spectra acquired from 2D scans (1) inside a void and (2) the surrounding matrix, as annotated in the high-resolution STEM image (inset). Voids are N-rich regions and the shape and energy-position of the N-K edge indicate the existence of N-N bonds in the voids along with pronounced Ga-N bonds in the ZOGN matrix.

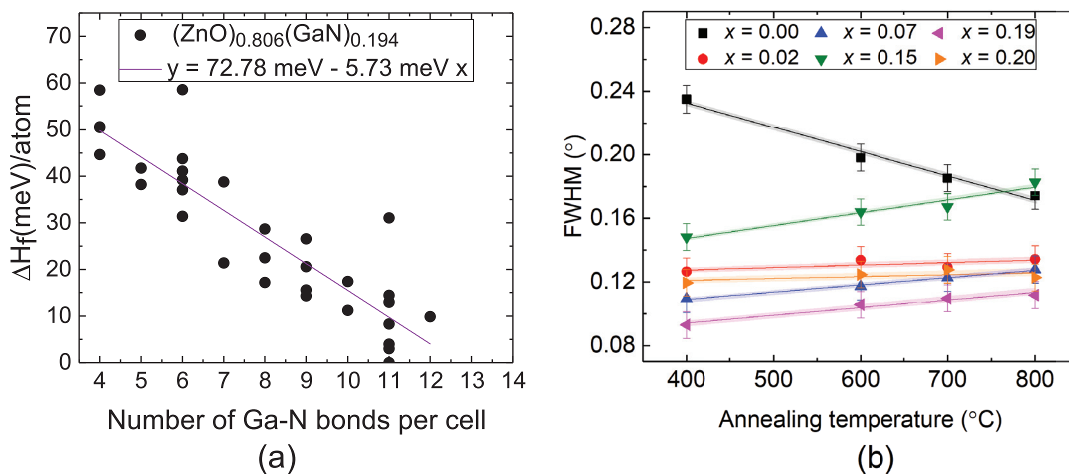

Figure 5.3: (a) shows the calculated change in formation energy per atom, ΔH_f/atom, as a function of Ga-N bonds for $x \approx 0.2$. Linear fit is represented with red line. (b) shows the FWHM of the (0002) peak measured using $\theta/2\theta$ scans as a function of post-deposition annealing temperature for different x. Linear fits are presented as lines.

5.3 Band Gap Evolution in $(ZnO)_{1-x}(GaN)_x$ Alloys

Over the years, several hypotheses have been suggested to explain of the observed band bowing effect in ZOGN. These hypotheses have to a large extent been based on theoretical calculations, as discussed in 4.2. In Paper III, experimental techniques including STEM-EELS, transmission measurements and PL, combined with theoretical calculations, using DFT and the GW approximation, were employed to determine the mechanisms governing the band bowing effect. The apparent band gap, E_g, for ZOGN thin films was estimated using transmission measurements, as well as STEM-EELS, both yielding a significant reduction down to $\sim$2.4 - 2.6 eV for $x \leq 0.15$. Using EELS represented as spatially resolved maps discriminating $\sim$5 nm pixels[96] together with EDX maps, it was furthermore found that the reduction in apparent E_g was close to homogeneous over the probed area, with no indications of segregation into ZnO- or GaN phases with band gap energies of $\sim$3.4 - 3.5 eV. Our experimentally obtained band bowing is also in remarkable agreement with our theoretically obtained results, utilizing the GW approximation. On the other hand, no redshift in the emission, measured by PL, was observed as a function of composition, x. Gaussian-like contributions to a broad deep band was affected upon increasing GaN incorporation, but the NBE, for all compositions, resembled that of pure ZnO, and attributed to the well-known excitonic peaks in ZnO.

Upon heat treatment, as discussed in section 5.2 the overall crystal quality was improved in terms of grain coalescence and reduction in both strain along the c-axis and threading dislocation density. Furthermore, indications of an increase in Ga-N bonds were observed. In terms of apparent E_g, no correlation between the optical band gap of the different alloy compositions and the annealing temperature (Paper III), where $x = 0.02$ shows only a minor change in apparent E_g after the last annealing step, whereas a larger spread in apparent E_g was observed for $x \geq 0.07$. Possible explanations for the evolution in apparent E_g were (i) increased crystal quality, reduced number of defects acting as non-radiative contributions, resulting in a steeper absorption slope and interpreted as a blueshift in apparent E_g, or (ii) structural cluster formation which has been theoretically predicted to cause a blueshift in E_g[61, 97].

Throughout the work reported in this thesis, it has been evident that a smooth, parabolic band bowing characterized by a bowing parameter fits poorly to our experimentally obtained results. As can be seen in Fig. 5.4, the apparent E_g is reduced rapidly when introducing GaN into ZnO, i.e. low-x, followed by a flat plateau with low compositional influence on apparent E_g. The rapid reduction for low-x was also observed by Maeda et al. [5] when incorporating ZnO into GaN, and as such the compositional apparent E_g-dependency can be divided into three regions, similar to what has been proposed for $(ZnO)_{1-x}(S)_x$ and $(ZnO)_{1-x}(Se)_x$ alloys[58]; a low (high)-x region with strong apparent E_g reduction, separated by a plateau with limited variations in apparent E_g. All our experimental results supports a band gap reduction caused by a defect band being formed above the ZnO VBM when incorporating GaN into ZnO. With this model, the absorption onset would decrease rapidly when more GaN is introduced into ZnO. The defect band hypothesis would also explain the apparent plateau with minimal compositional apparent E_g-dependency, as once the defect band is formed, no further reduction in the apparent E_g occur. This model was supported by theoretical

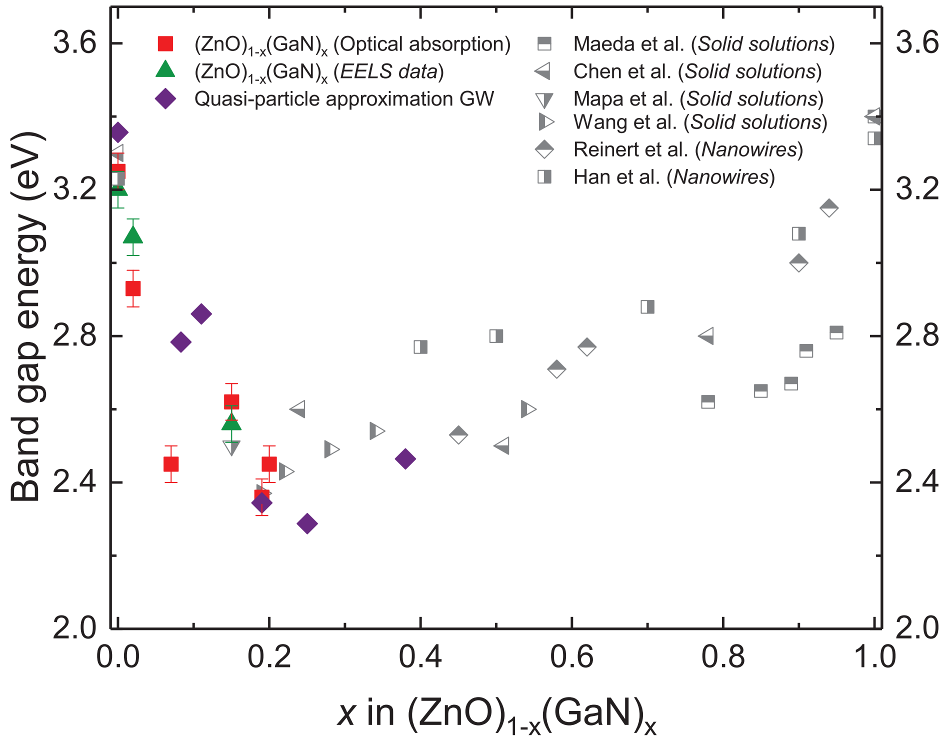

Figure 5.4: The magnitude of apparent band gap as a function of x, as determined by transmission measurements (filled squares), STEM EELS (filled triangles) and theory using GW approximation (filled diamonds). The band gap magnitudes are compared to the literature data (partly filled symbols) [6, 78–80, 98, 99].

calculations, as can be seen in Paper III, stating that the band gap reduction occurs mainly near the VB, whereas the CB is similar for both pure ZnO and the alloys. Fig. 5.5 shows that both the total density-of-states (DOS) and the partial atomic-resolved density-of-states (PDOS) for ZnO compared to ZOGN with two different compositions, $x \approx 0.02$ and 0.2. When incorporating GaN into ZnO, Ga+N states are formed above the VBM of pure ZnO, and the density of these Ga+N states shifts upward and becomes wider in energy with further increase in x from 0.02 to 0.2. Thus, N incorporation introduce a valence band at higher energy compared to VBM of ZnO. This defect band model can also explain the discrepancy between the measured absorption and emission, where a redshift in absorption was observed with increasing x up to 0.15, opposite to the stationary position of the NBE upon alloying. A defect band model can support this observation, since with the formation of a defect band, emission through CBM_{ZnO}-VBM_{ZnO} recombination would still be a viable route. Oppositely, a shift in the VBM due to orbital repulsion would expect a shift in the NBE. In Paper V, we indeed conclude that a defect band formation is the cause of band gap reduction in the ZOGN alloys.

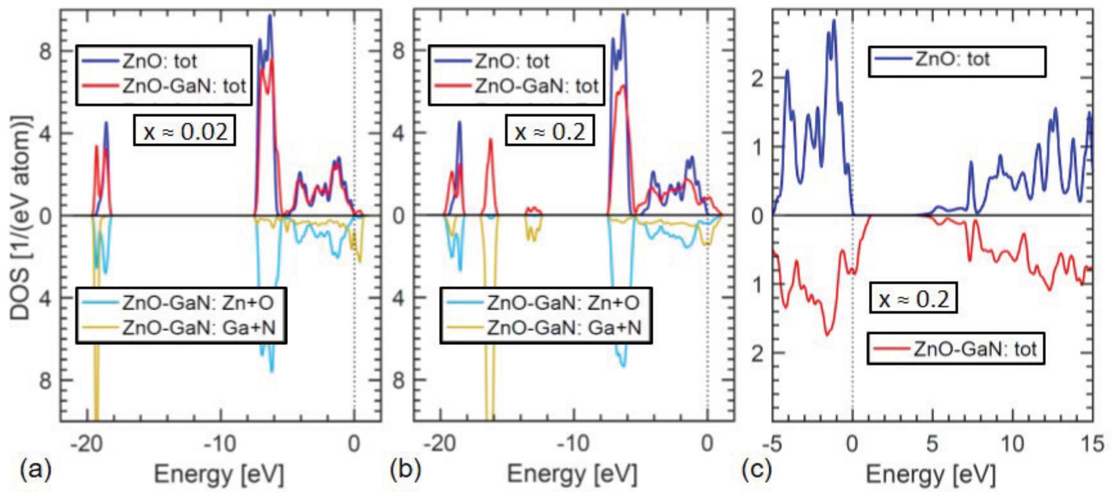

Figure 5.5: (a) Total DOS of the valence and semicore states for $x = 0$ (blue) and $x \approx 0.02$ (red) in upper panel, whereas the PDOS from Zn and O atoms (light blue) and Ga and N atoms (orange) in the $x \approx 0.02$ sample are shown in the lower panel. (b) same as in (a) but for $x \approx 0.2$. (c) Total DOS for $x = 0$ (blue) and $x \approx 0.2$ (red), scaled to lower energies, in order to emphasize that the effect on the electronic structure due to GaN incorporation occurs mainly near the VBM. The dotted vertical line indicates the VBM of pure ZnO. From Paper V.

5.4 Electrical Properties

If a material is to be utilized in optoelectronic or electronic applications, these properties needs to be controlled. Hence, the electrical properties of the ZOGN alloys were to some extent explored, e.g. using Hall effect measurements in the van der Pauw configuration. The ZOGN thin films with $x = 0.02$ and 0.15 were characterized using Hall measurements in order to determine the resistivity, mobility and carrier concentration. Detailed results form the ZOGN films with $x = 0.02$ and 0.15 are shown in Tab 5.2, whereas the mobility and carrier concentration are plotted as a function of temperature in Fig. 5.6 . The resistivity of the two as-grown thin films were fairly similar; 0.21 - 0.26 Ωcm, whereas the measured carrier concentration increased for $x = 0.02$ and 0.15, respectively, indicating a higher concentration of donors for $x = 0.15$. This may be attributed to the Ga/N ratio that is below and above unity for $x = 0.02$ and $x = 0.15$, respectively.

The isochromal anneals at 600°C, 700°C and 800°C in nitrogen atmosphere, discussed above, also affected the electrical properties of the films. A sharp increase in resistivity was observed for both compositions after the 600°C anneal by approximately two orders of magnitude, followed by a steady decrease of about one order of magnitude for $x = 0.02$ after annealing at 700°C and 800°C, respectively, reaching a minimum of 0.025Ωcm. The carrier concentration for $x = 0.02$, was reduced initially when annealing at 600°C by approximately one order of magnitude, shown in Fig. 5.6, indicating the activation of compensating defects, e.g. N-related acceptors, followed by a steady increase in carrier concentration. The mobility was also reduced slightly after the initial anneal at 600°C, but as for the carrier concentration, an increase of approximately one

Composition	Temp. [°C]	Atmosphere	Resistivity [Ω cm]	Std. Err. [Ω cm]	Mobility [cm^2/Vs]	Std. Err. [cm^2/Vs]
$x = 0.02$	As-grown		0.260	$4.83 \cdot 10^{-6}$	0.839	$6.64 \cdot 10^{-2}$
	600	N_2	10.395	$1.06 \cdot 10^{-3}$	0.386	$5.55 \cdot 10^{-2}$
	700	N_2	0.898	$5.39 \cdot 10^{-5}$	2.137	$9.20 \cdot 10^{-3}$
	800	N_2	0.025	$1.21 \cdot 10^{-6}$	10.032	$1.60 \cdot 10^{-1}$
	300	FG	0.131	$1.21 \cdot 10^{-5}$	1.943	$1.53 \cdot 10^{-1}$
	400	FG	0.042	$1.69 \cdot 10^{-6}$	3.885	$5.07 \cdot 10^{-2}$
$x = 0.15$	As-grown		0.210	$4.83 \cdot 10^{-6}$	0.426	$1.27 \cdot 10^{-1}$
	600	N_2	26.830	$4.34 \cdot 10^{-3}$	n.m.	
	700	N_2	2.630	$3.05 \cdot 10^{-4}$	0.296	$8.75 \cdot 10^{-3}$
	800	N_2	9.434	$5.87 \cdot 10^{-3}$	0.697	$7.81 \cdot 10^{-2}$
	300	FG	0.613	$2.72 \cdot 10^{-5}$	0.659	$1.63 \cdot 10^{-1}$
	400	FG	14.792	$1.05 \cdot 10^{-2}$	n.m.	

	Temp. [°C]	Atmosphere	Conduction	Carrier conc. [cm^{-3}]	Std. Err. [cm^{-3}]
$x = 0.02$	As-grown		n	$2.876 \cdot 10^{19}$	$2.53 \cdot 10^{18}$
	600	N_2	n	$1.588 \cdot 10^{18}$	$2.56 \cdot 10^{17}$
	700	N_2	n	$3.257 \cdot 10^{18}$	$1.40 \cdot 10^{16}$
	800	N_2	n	$2.469 \cdot 10^{19}$	$3.84 \cdot 10^{17}$
	300	FG	n	$2.471 \cdot 10^{19}$	$2.34 \cdot 10^{18}$
	400	FG	n	$3.818 \cdot 10^{19}$	$4.97 \cdot 10^{18}$
$x = 0.15$	As-grown		n	$8.069 \cdot 10^{19}$	$4.27 \cdot 10^{19}$
	600	N_2		n.m.	
	700	N_2	n	$8.029 \cdot 10^{18}$	$2.41 \cdot 10^{17}$
	800	N_2	n	$9.654 \cdot 10^{17}$	$1.09 \cdot 10^{17}$
	300	FG	n	$1.624 \cdot 10^{19}$	$3.65 \cdot 10^{18}$
	400	FG		n.m.	

Table 5.2: Measured resistivity, mobility and carrier concentration of the two compositions, $x = 0.02$ and 0.15, with standard errors. The electrical properties measured by Hall effect and van der Pauw method for the different annealing steps in two different atmospheres, i.e. N_2 and forming gas (FG), a mixture of H_2 and N_2. Each annealing step had the duration of one hour. For the $x = 0.15$ composition, two annealing steps showed no voltage tracking during measurements. Therefore, the mobilities and carrier concentrations obtained from these measurements should not be trusted, and are hence not listed in the table. These measurements are marked with n.m. (not measurable).

order of magnitude was observed per annealing step (up to $\sim$10 cm^2/Vs), as shown in Fig. 5.6, corroborating the increased overall crystal quality. The $x = 0.15$ film on the other hand showed a reduced resistivity after the 700°C anneal, followed by a slight increase after the 800°C. The carrier concentration was reduced by approximately one order of magnitude after 700°C and 800°C, respectively, whereas the mobility was relatively stable. The mobility and carrier concentration were not measurable after

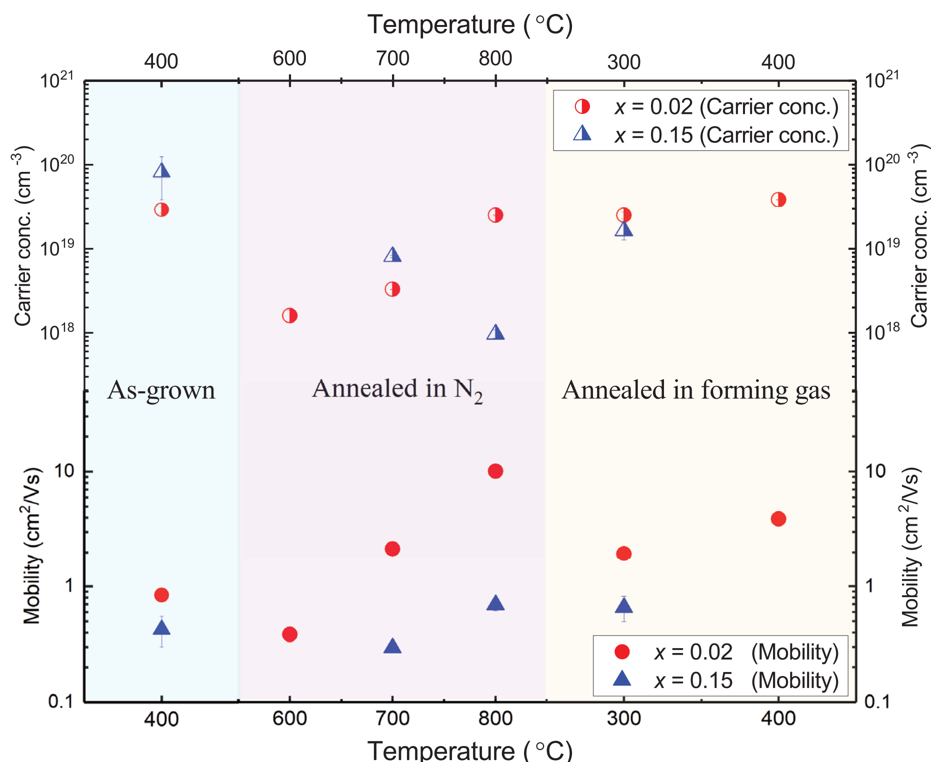

Figure 5.6: Measured carrier mobility and concentration for $x = 0.02$ and 0.15 using Hall measurements. The plot is divided in three areas with different background colour; (blue) as-grown films, (purple) thin films annealed in N_2 atmosphere after deposition, and (yellow) films annealed in FG after deposition. The upper part of the plot shows the carrier concentration, while the lower shows the mobility, both as a function of temperature.

600°C, probably due to the film having too low mobility.

The observed dip in both mobility and carrier concentration after the initial annealing step at 600°C originates most probably from the activation of acceptors in the alloys, where N on O-sites are probable candidates. The increase in carrier concentration after the annealing steps exceeding 600°C, and also in mobility, may be attributed to the relocation of N from substitutional O-site to form molecular N_2 bubbles, as discussed in Paper IV and also in MBE grown N-doped ZnO[95]. A decrease in N-acceptors will thus increase the carrier concentration in the films, as Ga on Zn-site still acts as electrically active donors.

A separate set of as-grown films were annealed in forming gas (FG), a mixture of H_2 (10%)and N_2 (90%), in order to increase both the carrier concentration and mobility. The films underwent isochronal anneals at 300°C and 400°C for one hour. In terms of mobility, an increase is observed, especially for the $x = 0.02$ composition, although not as significant as when annealed at 800°C in N_2 ambience, see Fig. 5.6. However, the $x = 0.15$ film did not yield reliable results after annealing at 400°C in FG and 600°C

in N_2 atmosphere. This may imply that the crystal quality and dislocation density is the limiting factor for the mobility, and that temperatures below 800°C are insufficient for significantly reducing the dislocation density. As for the carrier concentration, no significant change is observed for $x = 0.02$ when annealed in FG, whereas the $x = 0.15$ composition experiences a reduction when annealed at 300°C, and not measurable after annealing at 400°C.

Chapter 6

Conclusions and Future Work

This study has been a fundamental investigation of the ZOGN alloy, with the aim of utilizing the tunable functional properties in optoelectronic applications. Highly crystalline thin films were synthesized using rf magnetron sputtering, with x ranging from pristine ZnO to $x \leq 0.2$. The band bowing effect of the ZOGN alloys was observed, and the apparent band gap of the alloys was found to decrease rapidly when introducing GaN into ZnO, reaching a minimum of $\sim$2.4 - 2.5 eV for $x = 0.07$ (Paper I). Structurally, the films showed columnar grains with an epitaxial relationship to the c-Al_2O_3 substrate, with an alloy unit cell rotated 30° with respect to the substrate, which is typical also for ZnO-Al_2O_3 heterostructures in order to minimize lattice mismatch. Oppositely to what is expected from Vegard's law, an increase in c-lattice constant was observed for the as-grown films (Paper I), indicating strained films. Furthermore, the as-grown alloy films also contained a high concentration of threading dislocations. Thermal annealing in nitrogen atmosphere increased the overall crystal quality of the alloys, reducing the tensile strain along the c-axis as well as the dislocation densities. Other consequences of post-deposition annealing were the formation of nano-sized voids filled with molecular nitrogen (Paper IV), and possibly formation of nano-sized GaN-clusters (Paper II). The formation of nano-sized GaN-clusters has also been found to affect the optical properties of the alloys, as a blueshift in apparent E_g was observed. The band gap reduction of the ZOGN alloys was in Paper III investigated thoroughly both experimentally and theoretically using DFT and GW. Strong indications of a defect band formed above the VBM of ZnO when introducing GaN, and in its turn being responsible for the reduced absorption onset into the visible part of the spectrum. On the other hand, the near-edge-band emission of the alloys still resembled that of pure ZnO, indicating ZnO-like emission still being a viable route. The ZnO-like emission can be considered as an argument for the observed band bowing effect being caused by defect band formation, and not orbital repulsion.

An obvious continuation in future work on the ZOGN alloys is a more thoroughly investigation of the electrical properties, and tuning electrical conductivity through doping schemes. Compensating defects in the alloys should be overcome, paving the way for efforts towards a stable p-type conduction employing suitable dopants, as achieved in GaN. Furthermore, various structures and devices can be fabricated in order to further investigate the optoelectronic properties of the alloys; an absorber-structure with ohmic contacts where the current is measured as the monochromated light is incident on the alloys, scanned over wavelengths below the corresponding band gap of ZnO, may reveal information about the reduced absorption onset of the alloys and be exploited in sensor technologies. Another potential structure is to fabricate a pn junction with a suitable p-type material, and deposit a Schottky contact, allowing for deep level transient spectroscopy (DLTS) analysis. DLTS would open the possibility of exploring the evolution of deep level defects with band gap reduction.

Bibliography

[1] Sciences, T. R. S. A. of. *The Nobel Prize in Physics 1956*. English. The Royal Swedish Academy of Sciences. Oct. 1956. URL: https://www.nobelprize.org/prizes/physics/1956/summary/.

[2] Rahman, F. "Zinc oxide light-emitting diodes: a review." In: *Optical Engineering* vol. 58, no. 010901 (2019), pp. 1–20.

[3] Sze, S. M. and Kwok, K. N. *Physics of Semiconductor Devices*. Vol. 3. John Wiley & Sons, INC., 2007.

[4] Sciences, T. R. S. A. of. *The Nobel Prize in Physics 2014*. English. The Royal Swedish Academy of Sciences. Oct. 2014. URL: https://www.nobelprize.org/prizes/physics/2014/summary/.

[5] Maeda, K. et al. "Overall Water Splitting on $(Ga_{1-x}Zn_x)(N_{1-x}O_x)$ Solid Solution Photocatalyst: Relationship between Physical Properties and Photocatalytic Activity." In: *Journal of Physical Chemistry B* vol. 109, no. 43 (2005), pp. 20504–20510.

[6] Maeda, K. et al. "Photocatalyst releasing hydrogen from water." In: *Nature* vol. 440, no. 295 (2006).

[7] Özgür, Ü. et al. "A comprehensive review of ZnO materials and devices." In: *Journal of Applied Physics* vol. 98, no. 041301 (2005), pp. 1–103.

[8] Momma, K. and Izumi, F. "VESTA 3 for three-dimensional visualization of crystal, volumeric and morphology data." In: *Journal of Applied Crystallography* vol. 44 (2011), pp. 1272–1276.

[9] Sweeney, S. J. and Mukherjee, J. "Optoelectronic Devices and Materials." In: *Springer Handbook of Electronic and Photonic Materials*. Ed. by Kasap, S. and Capper, P. 2017.

[10] Burstein, E. "Anomalous Optical Absorption Limit in InSb." In: *Phys. Rev.* Vol. 93, no. 3 (1954), pp. 632–633.

[11] Moss, T. S. "The Interpretation of the Properties of Indium Antimonide." In: *Proc. Phys. Soc. London, Sect. B* vol. 67, no. 10 (1954), pp. 775–782.

[12] Sajeev, J. et al. "Theory of Electron Band Tails and Urbach Optical-Absorption Edge." In: *Physical Review Letters* vol. 57, no. 14 (1986), pp. 1777–1780.

[13] Urbach, F. "The Long-Wavelength Edge of Photographic Sensitivity and of the Electronic Absorption of Solids." In: *Physical Review* vol. 92, no. 5 (1953), pp. 1324–1324.

[14] Kouznetov, V. et al. "A novel pulsed magnetron sputter technique utilizing very high target power densities." In: *Surface and Coatings Technology* vol. 122 (1999), pp. 290–293.

[15] Ellmer, K. “Magnetron sputtering of transparent conductive zinc oxide: relation between the sputtering parameters and the electronic properties.” In: *Journal of Physics D: Applied Physics* vol. 33 (2000), R17–R32.

[16] Campbell, S. A. *Fabrication Engineering at the Micro- and Nanoscale*. 4th ed. Oxford University Press, 2013.

[17] Venables, J. A., Spiller, G. D. T., and Hanbucken, M. “Nucleation and growth of thin films.” In: *Rep. Prog. Phys.* Vol. 47, no. 4 (1984), pp. 399–459.

[18] Movchan, B. A. and Demchishin, A. V. “Structure and properties of thick condensates of nickel, titanium tungsten, aluminum oxides, and zirconium dioxide in vacuum.” In: *Physics of Metals and Metallography* vol. 28, no. 83 (1969).

[19] Thornton, J. A. “Influence of apparatus geometry and deposition conditions on the structure and topography of thick sputtered coatings.” In: *Journal of Vacuum Science and Technology* vol. 11, no. 4 (1974), pp. 666–670.

[20] Riise, H. N. et al. “Local homoepitaxy of zinc oxide thin films by magnetron sputtering.” In: *Thin Solid Films* vol. 601 (2016), pp. 18–21.

[21] Birkholz, M., Fewster, P. F., and Genzel, C. *Thin Film Analysis by X-Ray Scattering*. WILEY, 2006.

[22] Scherrer, P. “Bestimmung der Grösse und der inneren Struktur von Kolloidteilchen mittels Röntgenstrahlen.” In: *Nachrichten von der Gesellschaft der Wissenschaften zu Göttingen* (1918), pp. 98–100.

[23] Tauc, J., Grigorovici, R., and Vancu, A. “Optical Properties and Electronic Structure of Amorphous Germanium.” In: *Physica Status Solidi B* vol. 15 (1966), pp. 627–637.

[24] Kane, E. O. “Band Tails in Semiconductors.” In: *Solid-State Electronics* vol. 28, no. 1/2 (1985), pp. 3–10.

[25] Katahara, J. K. and Hillhouse, H. W. “Quasi-Fermi level splitting and sub-bandgap absorptivity from semiconductor photoluminescence.” In: *J. Appl. Phys.* Vol. 116, no. 173504 (2014), pp. 1–12.

[26] Olsen, V. S. et al. “Bandgap bowing in $(ZnO)_{1-x}(GaN)_x$ thin films; influence of composition and structural properties.” In: *Semiconductor Science and Technology* vol. 34, no. 015001 (2019), pp. 1–7.

[27] Fultz, B. and Howe, J. *Transmission Electron Microscopy and Diffractometry of Materials*. Ed. by Rhodes, W. T., Stanley, H. E., and Needs, R. 4. Springer, 2013.

[28] Bendersky, L. A. and Gayle, F. W. “Electron Diffraction Using Transmission Electron Microscopy.” In: *Journal of Research of the National Institute of Standards and Technology* vol. 106, no. 6 (2001), pp. 997–1012.

[29] Zhan, W. et al. “Nanoscale mapping of optical band gaps using monochromated electron energy loss spectroscopy.” In: *Nanotechnology* vol. 28, no. 105703 (2017), pp. 1–6.

[30] Gilliland, G. “Photoluminescence spectroscopy of crystalline semiconductors.” In: *Materials Science and Engineering: R: Reports* vol. 18, no. 3 (1997), pp. 99–399.

[31] Olsen, V. S. et al. “Evidence of defect band mechanism responsible for band gap evolution in $(ZnO)_{1-x}(GaN)_x$ alloys.” In: *Physical Review B* vol. 100, no. 165201 (2019), pp. 1–9.

[32] Schröder, D. K. *Semiconductor Material and Device Characterization*. 3rd ed. John Wiley & Sons, INC., 2006.

[33] Azarov, A. et al. “Defect stabilization and reverse annealing in ZnO implanted with nitrogen at room and cryogenic temperature.” In: *Journal of Applied Physics* vol. 123, no. 105701 (2018), pp. 1–6.

[34] Hohenberg, P. and Kohn, W. “Inhomogeneous Electron Gas.” In: *Physical Review* vol. 136, no. 3B (1964), B864–B871.

[35] Kohn, W. and Sham, L. J. “Self-Consistent Equations Including Exchange and Correlation Effects.” In: *Physical Review* vol. 140, no. 4A (1965), A1133–A1138.

[36] Perdew, J. P., Burke, K., and Ernzerhof, M. “Generalized Gradient Approximation Made Simple.” In: *Phys. Rev. Lett.* Vol. 77, no. 18 (1996), pp. 3865–3868.

[37] Perdew, J. P., Burke, K., and Ernzerhof, M. “Errata: Generalized grandient approximation made simple [Phys. Rev. Lett. 77, 3865 (1996)].” In: *Phys. Rev. Lett.* Vol. 78, no. 7 (1997), p. 1396.

[38] Heyd, J., Scuseria, G. E., and Ernzerhof, M. “Hybrid functionals based on a screened Coulomb potential.” In: *Journal of Chemical Physics* vol. 118, no. 18 (2003), pp. 8207–8215.

[39] Louie, S. G. and Rubio, A. “Quasiparticle and Optical Properties of Solids and Nanostructures: The GW-BSE Approach.” In: *Handbook of Materials Modeling: Methods*. Ed. by Yip, S. Dordrecht: Springer Netherlands, 2005, pp. 215–240.

[40] Look, D. C. et al. “Defect Donor and Acceptor in GaN.” In: *Physical Review Letters* vol. 79, no. 12 (1997), pp. 2273–2276.

[41] Look, D. C. et al. “On the nitrogen vacancy in GaN.” In: *Applied Physics Letters* vol. 83, no. 17 (2003), pp. 3525–3527.

[42] Moore, W. J. et al. “Identification of Si and O donors in hydride-vapor-phase epitaxial GaN.” In: *Applied Physics Letters* vol. 79, no. 16 (2001), pp. 2570–2572.

[43] Look, D. C., Fang, Z. Q., and Claflin, B. “Identification of donors, acceptors, and traps in bulk-like HVPE GaN.” In: *Journal of Crystal Growth* vol. 281 (2005), pp. 143–150.

[44] Pearton, S. J. et al. “GaN: Processing, defects and devices.” In: *Journal of Applied Physics* vol. 86, no. 1 (1999), pp. 1–78.

[45] Amano, H. et al. “P-type Conduction in Mg-Doped GaN Treated with Low-Energy Electron Beam Irradiation (LEEBI).” In: *Japanese Journal of Applied Physics* vol. 28, no. 12 (1989), pp. 2112–2114.

[46] Look, D. C. and Hemsky, J. W. “Residual Native Shallow Donor in ZnO.” In: *Physical Review Letters* vol. 82, no. 12 (1999), pp. 2552–2555.

[47] Liu, L. et al. “Oxygen vacancies: The origin of *n*-type conductivity in ZnO.” In: *Physical Review B* vol. 93, no. 235305 (2016), pp. 1–6.

[48] Van de Walle, C. G. “Hydrogen as a Cause of Doping in Zinc Oxide.” In: *Physical Review Letters* vol. 85, no. 5 (2000), pp. 1012–1015.

[49] Karzel, H. et al. “Lattice dynamics and hyperfine interactions in ZnO and ZnSe at high external pressures.” In: *Physical Review B* vol. 53, no. 17 (1996), pp. 11425–11438.

[50] Porowski, S. “Bulk and homoepitaxial GaN-growth and characterization.” In: *Journal of Crystal Growth* vol. 189-190 (1998), pp. 153–158.

[51] Denton, A. R. and Ashcroft, N. W. “Vegard’s law.” In: *Phys. Rev. A* vol. 43, no. 6 (1991).

[52] Jones, R. E. et al. “Band gap bowing parameter of $In_{1-x}Al_xN$.” In: *Journal of Applied Physics* vol. 104, no. 123501 (2008), pp. 1–6.

[53] Van de Walle, C. G. et al. “Large and composition-dependent band gap bowing in $In_xGa_{1-x}N$ alloys.” In: *Materials Science & Engineering, B: Solid-State Materials for Advanced Technology* vol. 59 (1999), pp. 274–278.

[54] Neumann, M. D. et al. “Inversion of absorption anisotropy and bowing of crystal field splitting in wurtzite MgZnO.” In: *Applied Physics Letters* vol. 108, no. 221105 (2016), pp. 1–5.

[55] Wassner, T. A. et al. “Optical properties and structural characteristics of ZnMgO grown by plasma assisted molecular beam epitaxy.” In: *Journal of Applied Physics* vol. 105, no. 023505 (2009), pp. 1–6.

[56] Jiang, J. et al. “Band gap modulation of ZnCdO alloy thin films with different Cd contents grown by pulsed laser deposition.” In: *Journal of Alloys and Compounds* vol. 547 (2013), pp. 59–62.

[57] Persson, C. et al. “Strong Valence-Band Offset Bowing of $ZnO_{1-x}S_x$ Enhances p-Type Nitrogen Doping of ZnO-like Alloys.” In: *Physical Review Letters* vol. 97, no. 146403 (2006), pp. 1–4.

[58] Baldissera, G. and Persson, C. “Understanding the optical properties of $ZnO_{1-x}S_x$ and $ZnO_{1-x}Se_x$ alloys.” In: *Journal of Applied Physics* vol. 119, no. 045704 (2016), pp. 1–13.

[59] Levinshtein, M., Rumyantsev, S. L., and Shur, M. S. *Properties of advanced semiconductor materials GaN, AlN, InN, BN, SiC, SiGe*. Ed. by Levinshtein, M., Rumyantsev, S. L., and Shur, M. S. John Wiley & Sons, INC., 2001.

[60] Lin, S.-H. et al. “Experimental Determination of Electron Affinities for InN and GaN Polar Surface.” In: *Appl. Phys Express* vol. 5, no. 031003 (2012), pp. 1–3.

[61] Liu, J., Fernández-Serra, M. V., and Allen, P. B. “Special quasiordered structures: Role of short-range order in the semiconductor alloy $(GaN)_{1-x}(ZnO)_x$.” In: *Physical Review B* vol. 93, no. 054207 (2016), pp. 1–8.

[62] Wei, W. et al. “Origin of the Visible Light Absorption of GaN-Rich $Ga_{1-x}Zn_xN_{1-x}O_x$ (x = 0.125) Solid Solution.” In: *Journal of Physical Chemistry C* vol. 112 (2008), pp. 15915–15919.

[63] Jensen, L. L., Muckerman, J. T., and Newton, M. D. “First-Principles Studies of the Structural and Electronic Properties of the $(Ga_{1-x}Zn_x)(N_{1-x}O_x)$ Solid Solution Photocatalyst.” In: *J. Phys. Chem. C* vol. 112 (2008), pp. 3439–3446.

[64] Valentin, C. D. “Electronic Structure of $(Ga_{1-x}Zn_x)N_{1-x}O_x$ Photocatalyst for Water Splitting by Hybrid Hartree-Fock Density Functional Theory Methods.” In: *Journal of Physical Chemistry C* vol. 114 (2010), pp. 7054–7062.

[65] Wang, Z. et al. “Hybrid density functional study of band alignment in ZnO-GaN and ZnO-$(Ga_{1-x}Zn_x)(N_{1-x}O_x)$-GaN heterostructures.” In: *Phys. Chem. Chem. Phys.* Vol. 14 (2012), pp. 15693–15698.

[66] Shan, W. et al. “Band Anticrossing in GaInNAs Alloys.” In: *Physical Review Letters* vol. 82, no. 6 (1999), pp. 1221–1224.

[67] Walukiewicz, W. et al. “Interaction of Localized Electronic States with the Conduction Band: Band Anticrossing in II-VI Semiconductor Ternaries.” In: *Physical Review Letters* vol. 85, no. 7 (2000), pp. 1552–1555.

[68] Dou, M., Baldissera, G., and Persson, C. “ZnO-InN nanostructures with tailored photocatalytic properties for overall water-splitting.” In: *International Journal of Hydrogen Energy* vol. 38 (2013), pp. 16727–16732.

[69] Li, L. et al. “Phase diagram, structure, and electronic properties of $(Ga_{1-x}Zn_x)(N_{1-x}O_x)$ solid solutions from DFT-based simulations.” In: *Physical Review B* vol. 83, no. 134202 (2011), pp. 1–6.

[70] Liu, J. et al. “Temperature and composition dependence of short-range order and entropy, and statistics of bond length: the semiconductor alloy $(GaN)_{1-x}(ZnO)_x$.” In: *Journal of Physics: Condensed Matter* vol. 26, no. 274204 (2014), pp. 1–9.

[71] Huang, D. and Persson, C. “Band gap change induced by defect complexes in Cu_2ZnSnS_4.” In: *Thin Solid Films* vol. 535 (2013), pp. 265–269.

[72] Maeda, K., Teramura, K., and Domen, K. “Effect of post-calcination on photocatalytic activity of $(Ga_{1-x}Zn_x)(N_{1-x}O_x)$ solid solution for overall water splitting under visible light.” In: *Journal of Catalysis* vol. 254 (2008), pp. 198–204.

[73] Chen, S. and Takata T. ad Domen, K. “Particulate photocatalysts for overall water splitting.” In: *Nature Review Materials* vol. 2, no. 17050 (2017), pp. 1–17.

[74] Adeli, B. and Taghipour, F. “A Review of Synthesis Techniques for Gallium-Zinc Oxynitride Solar-Activated Photcatalyst for Water Splitting.” In: *ECS Journal of Solid State Science and Technology* vol. 2, no. 7 (2013), Q118–Q126.

[75] Maeda, K. et al. “GaN:ZnO Solid Solution as a Photcatalyst for Visible-Light-Driven Overall Water Splitting.” In: *Journal of the American Chemical Society* vol. 127, no. 23 (2005), pp. 8286–8287.

[76] Maeda, K. and Domen, K. “New Non-oxide Photocatalysts Designed for Overall Water Splitting under Visible Light.” In: *Journal of Physical Chemistry C* vol. 111 (2007), pp. 7851–7861.

[77] Maeda, K. and Domen, K. “Solid Solution of GaN and ZnO as a Stable Photocatalyst for Overall Water Splitting under Visible Light.” In: *Chemistry of Materials* vol. 22 (2010), pp. 612–623.

[78] Mapa, M. et al. “Electronic Structure and Catalytic Study of Solid Solution of GaN in ZnO.” In: *Chemistry of Materials* vol. 21 (2009), pp. 2973–2979.

[79] Chen, H. et al. “In Situ XRD Studies of ZnO/GaN Mixtures at High Pressure and High Temperature: Synthesis of Zn-rich $(Ga_{1-x}Zn_x)(N_{1-x}O_x)$ Photocatalysts.” In: *J. Phys. Chem. C* vol. 114 (2010), pp. 1809–1814.

[80] Han, W. Q. et al. “Growth and electronic properties of GaN/ZnO solid solution nanowires.” In: *Applied Physics Letters* vol. 97, no. 083108 (2010), pp. 1–3.

[81] Zhong, M. et al. “A conductive ZnO-ZnGaON nanowire-array-on-a-film photoanode for stable and efficient sunlight water splitting.” In: *Energy and Environmental Science* vol. 7 (2014), pp. 1693–1699.

[82] Li, J. et al. “Solubility and crystallographic facet tailoring of $(GaN)_{1-x}(ZnO)_x$ pseudobinary solid-solution nanostructures as promising photocatalysts.” In: *Nanoscale* vol. 8 (2016), pp. 3694–3703.

[83] Li, J. et al. “Composition and Band Gap Tailoring of Crystalline $(GaN)_{1-x}(ZnO)_x$ Solid Solution Nanowires for Enhanced Photoelectrochemical Performance.” In: *Inorganic Chemistry* vol. 57 (2018), pp. 5240–5248.

[84] Lee, K. et al. “$(Ga_{1-x}Zn_x)(N_{1-x}O_x)$ Nanocrystals: Visible Absorbers with Tunable Composition and Absorption Spectra.” In: *Nano Letters* vol. 12 (2012), pp. 3268–3272.

[85] Wang, D. et al. “The photocatalytic properties of hollow $(GaN)_{1-x}(ZnO)_x$ composite nanofibers synthesized by electrospinning.” In: *Applied Surface Science* vol. 396 (2016), pp. 888–896.

[86] Wu, A. et al. “Band-gap tailoring and visible-light-driven photocatalytic performance of porous $(GaN)_{1-x}(ZnO)_x$ solid solution.” In: *Dalton Transactions* vol. 46 (2017), pp. 2643–2652.

[87] Shet, S. et al. “Effect of gas ambient and varying RF sputtering power for bandgap narrowing of mixed (ZnO:GaN) thin films for solar driven hydrogen production.” In: *Journal of Power Sources* vol. 232 (2013), pp. 74–78.

[88] Shet, S. et al. “Photoelectrochemical behavior of mixed ZnO and GaN (ZnO:GaN) thin films prepared by sputtering technique.” In: *Applied Surface Science* vol. 270 (2013), pp. 718–721.

[89] Yang, C. et al. “Epitaxy of $(GaN)_{1-x}(ZnO)_x$ Solid-Solution Thin Films with Widely Tunable Chemical Composition and Strong Visible Absorption.” In: *Physical Review Applied* vol. 10, no. 044001 (2018), pp. 1–9.

[90] Huda, M. N. et al. “Electronic structure of ZnO:GaN compounds: Asymmetric bandgap engineering.” In: *Physical Review B* vol. 78, no. 195204 (2008), pp. 1–5.

[91] Schifano, R. et al. “Comparison of the structural properties of Zn-face and O-face single crystal homoepitaxial ZnO epilayers grown by RF-magnetron sputtering.” In: *Journal of Applied Physics* vol. 121, no. 015304 (2017), pp. 1–8.

[92] Liu, M. et al. “Microscopic view of the role of repeated polytypism in self-organization of hierarchical nanostructures.” In: *Physical Review B* vol. 87, no. 085306 (2013), pp. 1–7.

[93] Nickel, N. H. and Gluba, M. A. "Defects in Compound Semiconductors Caused by Molecular Nitrogen." In: *Physical Review Letters* vol. 103, no. 145501 (2009), pp. 1–4.

[94] Lambrecht, W. R. L. and Boonchun, A. "Identification of a N-related shallow acceptor and electron paramagnetic resonance center in ZnO:N_2^+ on Zn site." In: *Physical Review B* vol. 87, no. 195207 (2013), pp. 1–5.

[95] Fons, P. et al. "Direct Observation of Nitrogen Location in Molecular Beam Epitaxy Grown Nitrogen-Doped ZnO." In: *Physical Review Letters* vol. 96, no. 045504 (2006), pp. 1–4.

[96] Granerød, C. S. et al. "The temperature-dependency of the optical band gap of ZnO measured by electron energy-loss spectroscopy in a scanning transmission electron microscope." In: *J. Appl. Phys.* Vol. 123, no. 145111 (2018), pp. 1–6.

[97] Wang, S. and Wang, L.-W. "Atomic and Electronic Structures of GaN/ZnO Alloys." In: *Physical Review Letters* vol. 104, no. 065501 (2010), pp. 1–4.

[98] Wang, J. P. et al. "Facile synthesis of Zn-rich $(GaN)_{1-x}(ZnO)_x$ solid solutions using layered double hydroxides as precursors." In: *J. Mater. Chem.* Vol. 21 (2011), pp. 4562–4567.

[99] Reinert, A. A. et al. "Synthesis and Characterization of Visible Light Absorbing $(GaN)_{1-x}(ZnO)_x$ Semiconductor Nanorods." In: *Inorganic Chemistry* vol. 52 (2013), pp. 8389–8398.

Paper I

Bandgap bowing in crystalline $(ZnO)_{1-x}(GaN)_x$ thin films; influence of composition and structural properties

---

V. S. Olsen, C. Bazioti, A. Azarov, B. G. Svensson, A. Yu. Kuznetsov, Ø. Prytz and L. Vines

Semiconductor Science and Technology 34, 015001 (2019)

My contribution: Planning and coordinating experiments, fabricate thin films, XRD and UV-VIS measurements, analysing results, and writing manuscript.

Paper II

Effect of Substrate and Post-Deposition Annealing on Structural and Optical Properties of $(ZnO)_{1-x}(GaN)_x$ Films

V. S. Olsen, C. Bazioti, G. Baldissera, A. Azarov, Ø. Prytz, C. Persson, B. G. Svensson, A. Yu. Kuznetsov and L. Vines

Physica Status Solidi B 256, 1800529 (2019)

My contribution: Planning and coordinating experiments, fabricate thin films, XRD and UV-VIS measurements, analysing results, and writing manuscript.

physica status solidi b
www.pss-b.com

Effects of Substrate and Post-Deposition Annealing on Structural and Optical Properties of $(ZnO)_{1-x}(GaN)_x$ Films

Vegard S. Olsen, Calliope Bazioti, Gustavo Baldissera, Alexander Azarov, Øystein Prytz, Clas Persson, Bengt G. Svensson, Andrej Y. Kuznetsov, and Lasse Vines*

The structural and optical properties of magnetron sputtered thin films of $(ZnO)_{1-x}(GaN)_x$ deposited on zinc oxide, sapphire, and silicon oxide are studied as a function of strain accumulation and post-deposition anneals at 600–800 °C. For the experimental conditions studied, we found that different amounts of tensile strain accumulated in the samples practically does not affect the strong bandbowing effect, that is, optical bandgap, observed in the as-deposited alloys. In its turn, post-deposition annealing results in a reduction of the tensile strain and dislocation density in the films, as measured by both X-ray diffraction and transmission electron microscopy, corroborating an increase in the crystal quality. In addition, the grain size is found to increase with annealing temperature, for example, mean values of 20 nm up to 50 nm were measured for the alloys with $x = 0.15$. Meanwhile, the full-width at half maximum of the (0002) X-ray diffraction reflection increases with annealing temperature, but with only a small increase in bandgap energies for the $x = 0.15$ sample. However, this observation was explained combining the experimental data and first-principles calculations based on density functional theory, showing that the increase in the amount of Ga-N bonds lowers the total energy of the system. As such, we conclude that the thermal treatments increase the Ga-N ordering, resulting in several contributions or a widening of the diffraction peaks.

1. Introduction

Controlling the functional properties is essential when developing novel semiconductor materials. ZnO and GaN are wide-bandgap semiconductors, with bandgap energies of ≈3.3 and ≈3.4 eV, respectively, at room temperature, making them applicable for optoelectronic devices such as light emitting diodes (LEDs) and lasers, solar blind detectors, and transparent conducting oxides.[1] When alloying ZnO and GaN in a $(ZnO)_{1-x}(GaN)_x$ alloy, a narrowing of the bandgap, E_g, has been found to occur, that is, a so-called bandbowing effect, well into the visible spectrum.[2] The origin of this bandbowing effect is still under debate, where orbital-repulsion within the valence band[3–6] and type-II band alignment[7,8] have both been suggested as plausible candidates. This bandgap narrowing has been exploited for water-splitting applications,[9–11] but is also a potential candidate for various optoelectronic applications as the alloy has been successfully fabricated as highly crystalline thin films as well.[12,13]

Experimentally, $(ZnO)_{1-x}(GaN)_x$ have mainly been grown using solid solution synthesis and for Ga and N rich compositions.[10,11,14,15] Shet et al. reported on sputtered alloy samples deposited on tin oxide substrates,[16] while Olsen et al. demonstrated alloyed films deposited by magnetron sputtering on sapphire substrates with up to 20% Ga and N incorporation.[12] Sapphire substrates were also used for depositing thin films utilizing pulsed-laser-deposition in the work by Yang et al.[13] However, the influence of the substrate on the structural and optical properties (in particular, the influence of the lattice mismatch and E_g properties) remains unexplored. In addition, the optical properties have been found theoretically to be affected by the local environment of the atoms, that is, the structural configuration.[3,17] There is on the other hand little experimentally obtained results exploring the effects of different structural configurations. Sputter deposition techniques result in films that are out of thermal equilibrium, thus post-deposition anneals may modify the material toward more thermally stable configuration.

In the present work, we have investigated the structural and optical dependencies of $(ZnO)_{1-x}(GaN)_x$ thin films with $0 \leq x \leq 0.2$ deposited on ZnO, Al_2O_3, and SiO_2, representing lattice-matched, lattice-mismatched, and amorphous substrates, respectively. Further, the influence of post-deposition annealing

V. S. Olsen, Dr. C. Bazioti, Dr. A. Azarov, Dr. Ø. Prytz, Prof. C. Persson, Prof. B. G. Svensson, Prof. A. Y. Kuznetsov, Dr. L. Vines
Department of Physics
Center for Materials Science and Nanotechnology
University of Oslo
P.O.Box 1048, Blindern, N-0316 Oslo, Norway
E-mail: v.s.olsen@smn.uio.no

G. Baldissera, Prof. C. Persson
Department of Materials Science and Engineering
Royal Institute of Technology
SE-100 44 Stockholm, Sweden

DOI: 10.1002/pssb.201800529

© 2019 WILEY-VCH Verlag GmbH & Co. KGaA, Weinheim

in nitrogen atmosphere on the structural and optical properties of the films deposited on the sapphire substrates was investigated, monitoring the evolution while shifting the balance toward thermal equilibrium.

2. Experimental Section

$(ZnO)_{1-x}(GaN)_x$ thin films were deposited on different lattice matched substrates, specifically O-faced ZnO, c-plane sapphire, and amorphous quartz, using a Moorfield Minilab magnetron sputtering system with separate ZnO (99.999% purity) and GaN (99.99% purity) 3 inch targets. The ZnO and sapphire substrates were cleaned by annealing in oxygen atmosphere for 1 h at 1150 °C, while the quartz substrates were cleaned using the RCA process, before the samples were loaded into the sputter chamber. The base pressure prior to deposition was below 2×10^{-6} Torr, while the pressure during deposition was kept at 7 mTorr. The substrate temperature was kept at 400 °C and the sample stage was rotated at 11 rpm to ensure good film uniformity. A pre-sputtering cleaning was carried out for 20 min before deposition to remove surface impurities from the targets. During the co-sputtering process, where the two targets are running simultaneously, the composition was controlled by applying different voltages to the targets, in addition to controlling the gas flows of N_2 and Ar in the chamber. For instance, to obtain $x = 0.15$ (see **Table 1**), 30 and 20 W were applied to the ZnO and GaN targets, respectively, while gas flows of 12.5 SCCM Ar and 5 SCCM N_2 were kept constant during deposition. The deposition times varied for the respective composition in order to obtain films with thicknesses of ≈1.5 μm, as measured by ellipsometry, see Table 1.

The Ga and N content in the alloy films were measured using scanning electron microscopy (SEM) in energy dispersive X-ray spectroscopy (EDS) mode. Utilizing secondary ion mass spectrometry (SIMS), the Ga and N concentrations were also measured as a function of film-depth by using a Cameca IMS 7f microanalyzer with either 15 keV Cs^+ or 10 keV O_2^+ ions as the primary beam. The depth of the sputtered crater was measured by a Veeco Dektak 8 stylus profilometer. Assuming a uniform and time-independent erosion rate, the measured crater depth was used to convert sputtering time to sample depth. Ga and N ion implanted reference samples were used to convert the recorded secondary ion intensities to concentration.

X-ray diffraction (XRD) characterization was made utilizing the Bruker AXS D8 Discover system. The X-ray source was Cu Kα ($\lambda = 1.5406$ Å), and a Ge (220) double bounce monochromator was implemented to filter out the Kα_2 signal ($\lambda = 1.5444$ Å). The instrumental broadening of the diffraction peaks of 0.008° is included in the standard error bar while analyzing the results. Transmission measurements were carried out using a Shimadzu SolidSpe-3700 DUV spectrophotometer. The wavelength range of this instrument is 175–2600 nm, with 0.1 nm resolution.

Rutherford backscattering spectroscopy (RBS) analysis of the thin films were realized using the National Electrostatics Corporation (NEC) tandem ion accelerator employing 1.62 MeV He^+ ions, incident along the [0001] direction. The backscattered beam was analyzed at an angle of 165° with respect to the incident beam.

Transmission electron microscopy (TEM) thin foil preparation for cross-sectional observations was performed by mechanical grinding using the tripod wedge polishing method in the Allied Multiprep, followed by Ar^+ ion milling in the Gatan PIPS II. Finally the samples were plasma cleaned using a Fichione Model 1020 plasma cleaner in order to minimize carbon contamination. (Scanning) TEM ((S)TEM) observations were performed in a probed-corrected FEI Titan G2 60–300 microscope, operated at 300 kV.

3. Computational Methods

The crystalline structures of $(ZnO)_{1-x}(GaN)_x$ alloys were also determined theoretically using the Perdew-Burke-Ernzerhof (PBE) generalized gradient approximation[18,19] within the density functional theory (DFT), as provided by the VASP software package.[20,21] A 72-atom unit cell structure was modeled for the alloys, where the Ga-N concentration of $x = 14/72 \approx 0.194$ were obtained by replacing seven Zn-O pairs. We choose different configurations for this concentration, for which we calculate the differences in formation energies. Although PBE does not generate accurate absolute values of the bandgap energy, we can still analyze if various alloy configuration yield changes in the gap energies. With a cut-off energy of 700 eV, the relaxation was carried out alternating between volume and atom position relaxation until the final force in the atoms were smaller than 5 meV Å^{-1}. Thereafter, a cut-off energy of 400 eV was used in the PBE calculations together with a Γ-centered 8 × 8 × 8 **k**-mesh in the final calculations.

Table 1. Survey of the samples prepared for this study, together with the growth parameters, as well as the measured thicknesses using ellipsometry.

Concentration			Power		Flow			
x	Ga [at%]	N [at%]	ZnO [W]	GaN [W]	Ar [SCCM]	N_2 [SCCM]	Thickness [nm]	Time [min]
0	0	0	30	0	12.5	0	1380	1440
0.02	1.1 ± 0.1	3.0 ± 0.3	30	7	12.5	0.7	1110	1440
0.07	3.5 ± 0.2	3.4 ± 0.3	30	10	12.5	0.7	1690	1440
0.15	7.5 ± 0.4	5.7 ± 0.4	30	20	12.5	5	1330	1200
0.19	9.5 ± 0.5	6.5 ± 0.5	20	20	10	20	1880	1800
0.20	10.0 ± 0.5	7.9 ± 0.5	30	30	10	20	1290	1200

© 2019 WILEY-VCH Verlag GmbH & Co. KGaA, Weinheim

4. Results and Discussion

$(ZnO)_{1-x}(GaN)_x$ thin films with x ranging from 0 to 0.20 were manufactured using co-sputtering deposition, as previously reported.[12] The composition, x, is taken twice the measured Ga content using SEM, see Table 4. In addition, the $x = 0.15$ thin film was measured using SIMS, both to ensure that there were no large variations in Ga- and N concentration as a function of the film depth, as well as to have a supporting result for the composition, x, by averaging the Ga- and N concentrations over the film thickness. The films were found to be highly crystalline and yield a good heteroepitaxial relationship to the sapphire substrate. The optical absorption onset of the films shift toward lower energies with increasing GaN content x, as expected due to E_g lowering. Hence, in the following a redshift of the optical onset will be interpreted as a decrease in E_g.

4.1. Influence of Different Lattice-Matched Substrates

$(ZnO)_{1-x}(GaN)_x$ thin films with x varying from 0.02 to $x = 0.20$ were deposited on ZnO (O-faced), c-sapphire and quartz substrates, representing a lattice-matched, a lattice-mismatched and an amorphous substrate, respectively. Using the (0002) XRD reflection of the $(ZnO)_{1-x}(GaN)_x$ films, the c-lattice constants were calculated and plotted as a function of GaN content, x, for the films grown on the different lattice-matched substrates, as shown in **Figure 1**. The lattice constants of the alloy, both a and c, are expected to follow Vegard's law,[22] decreasing linearly from ZnO to GaN, where the expected linear decrease in c-lattice constant is represented by a dashed line in Figure 1. The expected decrease in a-lattice constant yields an increase in the in-plane lattice mismatch of the $(ZnO)_{1-x}(GaN)_x$ alloy on ZnO substrate from 0 to 2.8% with increasing GaN content, x. The same in-plane lattice mismatch will vary from 31.7 to 33.6% when deposited on c-sapphire substrate, assuming that there is no in-plane rotation of the film's unit cell with respect to the the unit cell of the substrate. $(ZnO)_{1-x}(GaN)_x$ films were found, utilizing TEM, to exhibit 30° rotation of the unit cell with respect to that of the c-sapphire substrate.[12] This orientation relationship is common since it results in a favorable mismatch (close to 18%[23–25] for ZnO on c-sapphire).

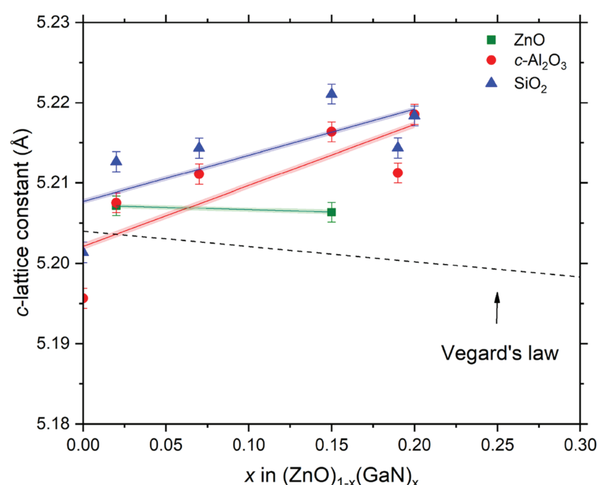

Figure 1. c-lattice constants as deduced from the XRD data as a function of GaN concentration, x, for $(ZnO)_{1-x}(GaN)_x$ grown on different substrates. The dashed line illustrates the change in the c-lattice parameter in the alloy as predicted by Vegard's law. Linear fits for the deduced lattice constants for ZnO, Al_2O_3, and SiO_2 are shown as green, red, and blue lines respectively, whereas semitransparent areas surrounding the lines are present for better visual representation.

The strain along the c-axis in a thin film is defined as $\varepsilon_c = (c - c_0)/c_0$, where c is the measured c-parameter, and c_0 is a reference lattice parameter.[26] Therefore, for a specific composition, x, ε_{c_x} may be estimated as $\varepsilon_{c_x} = (c_{\text{measured}_x} - c_{\text{vegard}_x})/c_{\text{vegard}_x}$ where c_{measured_x} is the measured c-parameter, and c_{vegard_x} is an approximated c-parameter for that composition, x, predicted by Vegard's law. As can be seen in Figure 1, the measured c-lattice constants of all alloy thin films are larger than those predicted by Vegard's law, indicating the accumulation of tensile strain. This situation is observed regardless of the substrate used, but the magnitude of the strain is substrate-dependent. The films deposited on the O-faced ZnO substrates exhibit the lowest tensile strain, with the c-lattice constant slightly decreasing from $x = 0.02$ to 0.15. Further, the films deposited on c-sapphire substrates yield higher tensile strain. For the $x = 0.02$, the c-lattice constant is close to that of the film deposited on O-faced ZnO. Notably, instead of a decrease in c-lattice constant with increasing GaN concentration, as predicted by Vegard's law[22] and observed on the O-faced ZnO substrates, the c-lattice constant increases when incorporating more GaN on c-sapphire substrates. The highest tensile strain is observed in the alloy thin films deposited on the amorphous quartz substrates. Also in these films, an increase in the c-lattice constant is observed for increasing GaN content.

Figure 2 displays the full width at half maximum (FWHM) of the (0002) peak using $\theta/2\theta$ and rocking curve scans. Similar to the measurements of the c-lattice constant, the FWHM of the $\theta/2\theta$ scans (square markers in Figure 2) show the lowest values for the films deposited on O-faced ZnO substrates, while the FWHM increase for the films deposited on c-sapphire and quartz. An increase in FWHM is typically interpreted in terms of a decrease in the grain size, for example, as calculated by the Scherrer equation,[27] and thus as a downturn in crystal quality. Evaluating the rocking curve FWHM data again (triangles in Figure 2), there is a clear trend for the lowest values on the lattice-matched substrate, while the films deposited on the amorphous substrate yield the largest FWHM. Notably, the broadening in rocking curve peaks is often related to the increase in dislocation density. Thus, the FWHM data trend indicates an increase in the dislocation density in the films as a function of the substrate mismatch.

Figure 3 is a Tauc plot as constructed from the optical transmission data for $(ZnO)_{1-x}(GaN)_x$ films with $x = 0.02$ and $x = 0.15$ grown on the different substrates; the raw data are included in the inset. The transmittance of the films (inset in Figure 3) deposited on sapphire substrates is somewhat lower than that for the two other substrates since the sapphire substrates were only one-side polished, provoking higher reflection. In contrast to the difference observed for the c-lattice constant and FWHM values, E_g is found to be similar for each

© 2019 WILEY-VCH Verlag GmbH & Co. KGaA, Weinheim

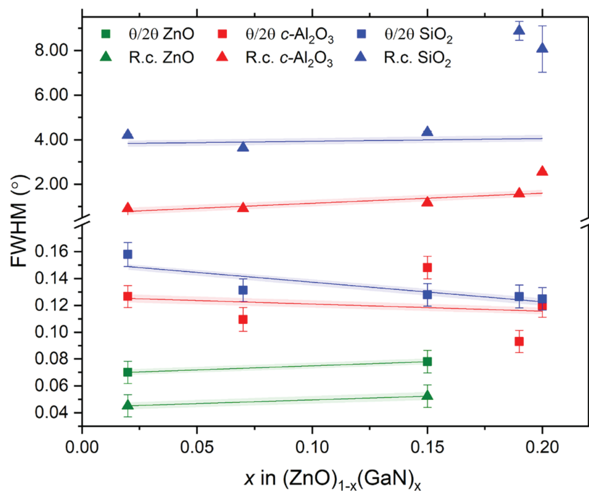

Figure 2. FWHM values from the $\theta/2\theta$-scans (squares) and rocking curve scans (triangles) for the films deposited on O-faced ZnO (green), c-sapphire (red), and amorphous quartz (blue). Linear fits for $\theta/2\theta$-scans (lines) and rocking curve scans (dashed lines) are shown, in addition semitransparent areas surrounding the fits for better visual representation.

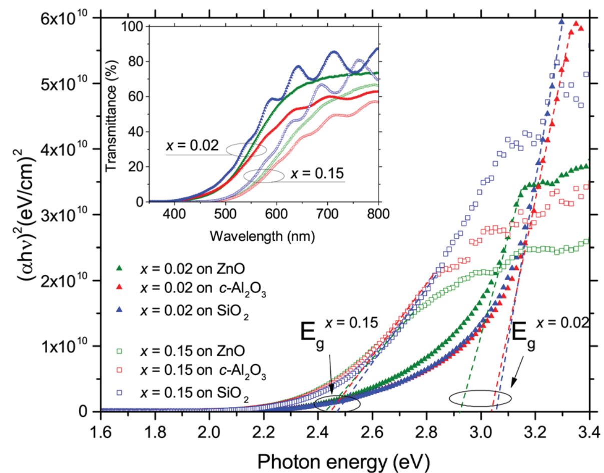

Figure 3. Tauc plot as constructed from the optical transmission data assuming direct E_g. The filled triangles represent the $x = 0.02$, the empty squares represent the $x = 0.15$, and the films were deposited on ZnO (green), Al_2O_3 (red), and SiO_2 (blue). The dotted lines represent the extension of the linear region of the absorption edge, indicating E_g at the intersect with the energy-axis. The inset shows raw transmittance data as a function of wavelength from the same samples and using the same type of legend.

alloy composition independently of the substrates used, specifically $\approx$2.9–3.1 eV and $\approx$2.4–2.5 eV for $x = 0.02$ and $x = 0.15$, respectively. The large Urbach-tail observed for $x = 0.02$, and the smaller Urbach-tail observed for $x = 0.15$, were also independent of the substrate. A large Urbach-tail is interpreted as an increased concentration of localized states within E_g, again indicating that the optical properties of the alloy do not change significantly with the substrate used. Notably, pure ZnO and GaN exhibit bandgaps of $\approx$3.3 and $\approx$3.4 eV, respectively, at room temperature.

Summarizing the data of the subsection, the tensile strain and dislocation density occurring in the films depend strongly on the choice of substrate, while the optical properties do not vary significantly with substrate.

4.2. Influence of Post-Deposition Annealing

The influence of the post-deposition annealing on the properties of $(ZnO)_{1-x}(GaN)_x$ films deposited on c-Al_2O_3 substrates was investigated using three annealing steps. Each thin film was annealed for one hour in nitrogen atmosphere at 600, 700, and 800 °C, with structural and optical characterization after each annealing step. **Figure 4** shows the c-lattice constant versus composition for as-deposited and 800 °C annealed samples as measured with XRD (triangles) and HRTEM (circles), compared to the c-lattice constants obtained by Chen et al.,[11] who observed an upward bowing of the c-lattice constant as a function of x, in good agreement with our as-grown films. This upward c-lattice constant bowing was also theoretically predicted.[4] The inset in Figure 4 shows the (0002) XRD reflection of the $x = 0.15$ film after deposition (as-grown), as well as after each annealing step. The reflection is shifted toward higher 2θ-angles with annealing temperature, indicating a decrease in c-lattice constant. After the anneals the c-lattice constant comes closer to the values predicted by Vegard's law compared to that of the as-grown samples, indicating a significant lowering of the tensile strain in the films. Sputtering is in general a non-equilibrium process, thus post-deposition annealing is expected to modify the thin films, bringing the alloy toward thermal equilibrium. Indeed, the relaxation observed in Figure 4 can be explained by the increase

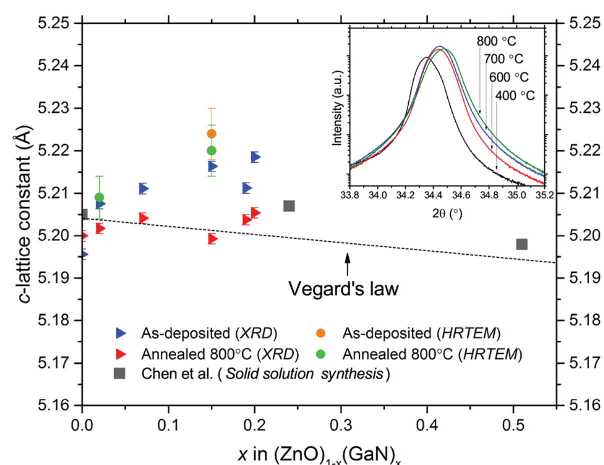

Figure 4. c-lattice constants as deduced from the XRD data (triangles) and HRTEM (circles) as a function of GaN concentration, x, for $(ZnO)_{1-x}(GaN)_x$ before and after the post-deposition anneals. The results are compared to the lattice constants obtained by Chen et al.[11] The dashed line illustrates the change in the c-lattice parameter in the alloy as predicted by Vegard's law. The inset shows the (0002) reflection of the $x = 0.15$ film after each annealing step, measured by XRD.

© 2019 WILEY-VCH Verlag GmbH & Co. KGaA, Weinheim

in atomic mobility, giving the atoms a higher probability to find more energetically favorable configurations in the lattice, and hence lowering the total energy of the system. Another observation that can be made from Figure 4 is that there is a discrepancy between the *c*-lattice constants measured with XRD and TEM. The lattice constants obtained from TEM measurements are extracted from smaller, more local areas of the film, whereas the lattice constants measured with XRD are statistically averaged over a larger area. This can imply that for the $x = 0.15$ composition, there is a larger local variation in lattice constants compared to for instance the $x = 0.02$ composition, where the results from the two methods are in more agreement.

Figure 5 illustrates HAADF (high-angle annular dark-field)-STEM images taken from the upper part of the $x = 0.15$ films (a) before and (b) after the 800 °C annealing step. A columnar grain structure is evident and diffraction patterns showed a heteroepitaxial relationship described by $[0001]_{(ZnO)_{1-x}(GaN)_x}//[0001]_{Al_2O_3}$ (out-of-plane) and $[10\bar{1}0]_{(ZnO)_{1-x}(GaN)_x}//[11\bar{2}0]_{Al_2O_3}$ (in-plane), indicating a 30° in-plane rotation of the film's unit cell with respect to the unit cell of the substrate. The TEM investigations also revealed a reduced threading dislocation (TD) density after annealing (Figure S1, Supporting Information), as well as an increase in the width of the grains with mean values of 20 up to 50 nm for as-grown and 800 °C annealed samples, respectively. This could be attributed to the grain coalescence during the annealing process, resulting in the formation of larger grains, with fewer defects, and an overall improved crystalline quality. On the other hand, no clear improvement of the disorder was found after annealing by RBS measurements, see Figure S3, Supporting Information. Nano-sized inclusions of lower density (dark spots), as can be seen in Figure S2, Supporting Information, were also observed after annealing, with the majority of them being located along grain boundaries and TDs.

Figure 6 summarizes the FWHM data taken from the (0002) XRD peak for several alloy compositions as a function of annealing temperature. Interestingly, the FWHM for the pure ZnO film decreases with annealing temperature, while the alloy FWHM exhibits an increase. The narrowing of the (0002) XRD reflection for pure ZnO is expected, as post-deposition annealing enhances the overall crystal quality of the film. An ancrease in FWHM, on the other hand, as observed for the alloy can happen either due to i) a decrease in the crystalline quality or ii) because the (0002) peak in the alloy sample may consist of several overlapping contributions evaluated as a single peak.

Considering explanation (i), the measured rocking curve FWHM (see Figure S4, Supporting Information) show in general a decreasing trend with annealing temperature, a trend especially clear for the low-*x* compositions, indicating a decrease in dislocation density, as such not supporting hypothesis (i). Thus, this argument, together with the considerations of the TEM results above suggest that the crystalline quality increases after post-deposition annealing.

Figure 7 plots the variation of E_g as extracted from the transmission measurements (see Figure S5, Supporting Information) as a function of annealing temperature, for the samples with different GaN-content. In accordance with previously reported measurements of the as-deposited samples, the measured optical E_g of pure ZnO and $x = 0.02$ alloy is ≈3.3 and ≈2.9 eV, respectively, while the higher GaN-content films show E_g energies ≈2.4–2.5 eV.[12] By monitoring E_g (i.e., onset of optical absorption) after each annealing step there is an unsystematic change for the different compositions. After the 800 °C anneal, there is no large change in E_g for $x = 0.02$, whereas there is a larger spread in E_g for $0.07 \leq x \leq 0.20$. Interestingly, a change in the bandgap is predicted by theory,

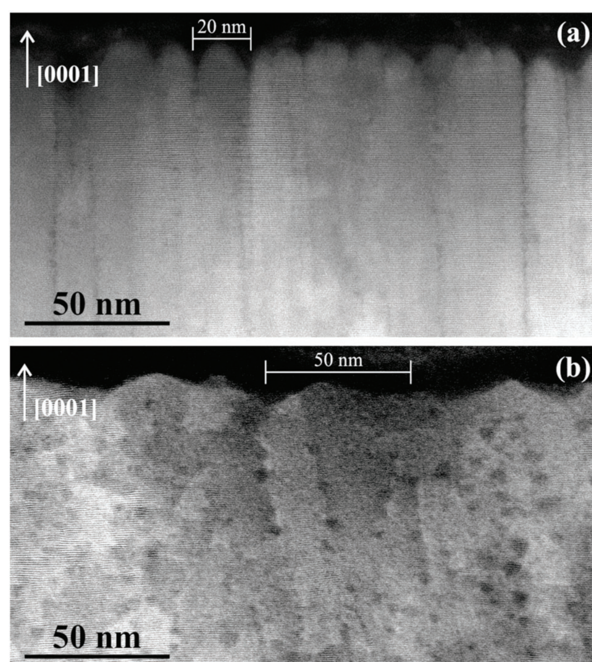

Figure 5. HAADF-STEM images of the $x = 0.15$ films grown on *c*-Al_2O_3 (a) before and (b) after the 800 °C thermal annealing step. A clear increase in the grain size is observed after annealing, resulting in an improved overall crystal quality of the films, with lower TD density.

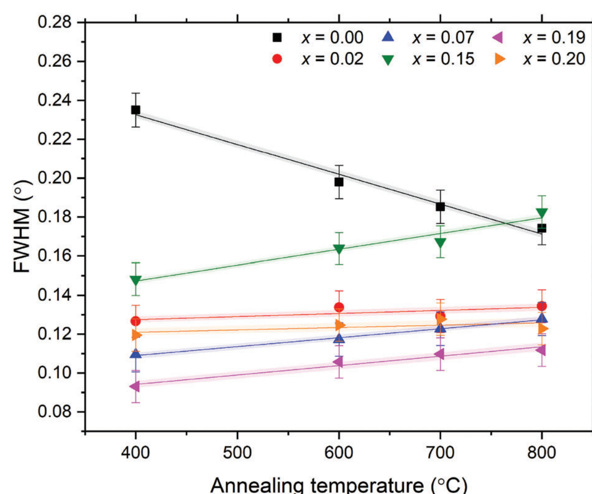

Figure 6. FWHM of the (0002) peak measured using $\theta/2\theta$ scans as a function of post-deposition annealing temperature for different alloy compositions. Linear fits are presented as lines, with a semitransparent area surrounding for better visual representation.

© 2019 WILEY-VCH Verlag GmbH & Co. KGaA, Weinheim

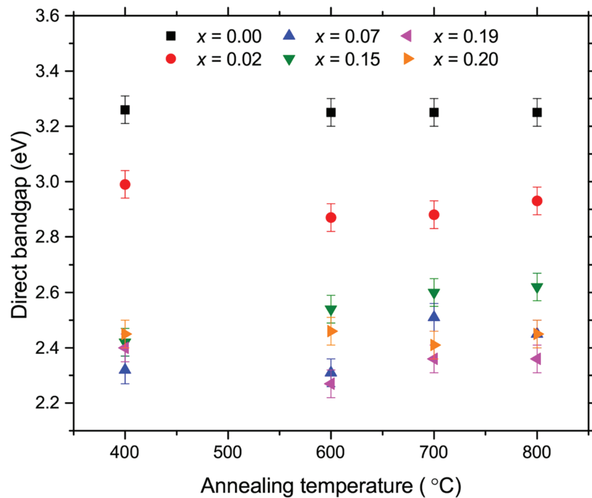

Figure 7. E_g as a function of annealing temperature for the alloys with different GaN concentration, x. The data are taken from transmission measurements.

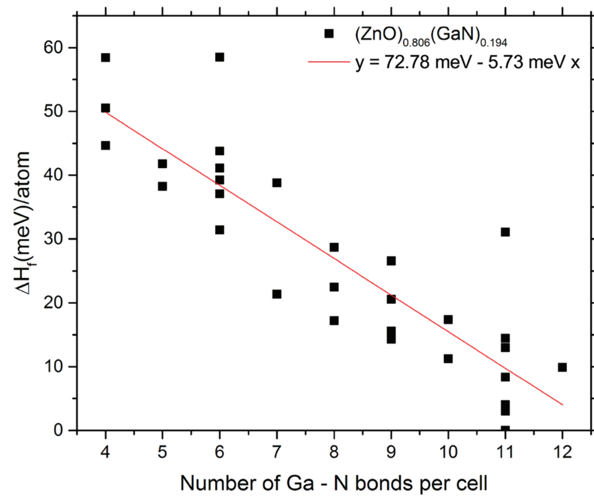

Figure 8. The calculated change in formation energy per atom, ΔH_f/atom, as a function of Ga–N bonds for $x = 0.194$.

where a blueshift in the E_g is predicted when the disorder in the alloy decreases, corroborated by an increase in short-range order using Monte Carlo simulations,[3,8] whereas Maeda et al.[28] observed a red-shift in the absorption onset with annealing.

One possible explanation for the change in E_g with annealing temperature is increased crystal quality, where non-radiative defects can be annealed out. A reduced concentration of non-radiative contributions results in a steeper slope in the Tauc plots, increasing the absorption onset. A supporting argument for the reduced number of non-radiative contributions was found when E_g was estimated assuming indirect allowed transitions (i.e., $r = 1/2$ in the Tauc analysis). This estimate resulted in significantly lower E_g, than those from the direct transitions (not shown), but increasing with the annealing temperature, approaching those of the direct E_g. This corroborates that non-radiative contributions are annealed out.

Another possible explanation for the evolution of E_g, seen in Figure 7, is related to cluster formation in the alloys. As discussed above, an alternative explanation to the increase in FWHM of the (0002) peak in the $\theta/2\theta$ scans in Figure 6 may be due to the overlapping of several closely located peaks. In particular, this can occur if clusters with different bond lengths are formed during annealing, where clustering for the $(ZnO)_{1-x}(GaN)_x$ alloy has been predicted to be energetically favorable.[6] Indeed, cluster formation in an alloy is expected to change the optical properties of the alloy, for example, a decrease in E_g was found for the ZnO–InN system.[29] In our theoretical calculations using the PBE functional, 30 configurations were constructed for $(ZnO)_{1-x}(GaN)_x$ with $x = 0.194$. This composition has been found to be in the steady-bandgap regime ($0.07 \leq x \leq 0.20$),[12] whereas lower concentrations yield strong bandgap bowing. Many of the other alloy configurations have total energies that are substantially higher than the most stable one, and they are therefore not thermodynamically feasible. Thus, the change in the formation energy can be calculated for different configurations of the alloy, so that the change in the formation energy per atom, ΔH_f/atom, for a specific $x = 0.194$ cell, is given by

$$\frac{\Delta H_f}{\text{atom}} = \frac{E_{\text{Tot}}(x = 0.194)_{\text{conf}} - E_{\text{Tot}}(x = 0.194)_{\text{ms}}}{72}$$

where $E_{\text{Tot}}(x = 0.194)_{\text{conf}}$ is the total energy of a configuration, while $E_{\text{Tot}}(x = 0.194)_{\text{ms}}$ is the total energy of the most stable configuration of the $x = 0.194$ cell. The calculated ΔH_f is divided by the number of atoms in the super cell, that is, 72, to find ΔH_f per atom. In **Figure 8**, the change in the formation energy per atom is plotted against the number of Ga–N bonds in the cell. Indeed, there is a decrease in ΔH_f with increasing number of Ga–N bonds, indicating that more Ga–N bonds yield more stable configurations, which also has been found in other studies.[4,6,17,30] This result makes the formation of nano-sized GaN clusters to be a probable consequence of the post-deposition anneals, so that more Ga–N bonds are formed to lower the energy of the system, assuming that Ga and N are sufficiently mobile during the post-deposition annealing to find a more energetically favorable position. This can explain the broadening of the (0002) peak in Figure 6 and the unsystematic variations in the bandgap, (in Figure 7) as different alloy configurations may have different bandgaps superimposed during the measurement. Since the Ga–N and Zn–O bonds have different strengths reflected in different lattice constants, the more Ga–N bonds are formed during the annealing processes, the broader the (0002) reflection is, supporting hypothesis (ii).

5. Conclusion

In conclusion, $(ZnO)_{1-x}(GaN)_x$ thin films with x ranging from 0 to 0.2 were deposited on different lattice-matched substrates. Structurally, the alloy thin films deposited on ZnO substrate yield lowest tensile strain and dislocation density compared to the films deposited on c-sapphire and quartz. Optically, there were no significant variations in

© 2019 WILEY-VCH Verlag GmbH & Co. KGaA, Weinheim

either the estimated E_g nor in the size of the Urbach tail among the samples. The films were also post-deposition annealed to investigate the effects of heat-treatment. In the course of anneals, the overall crystalline quality of the films was found to increase, while a significant relaxation in the *c*-lattice constant was observed, lowering the tensile strain of the films. In addition, the grain size was found to increase with annealing, with the mean values of 20 nm up to 50 nm found for $x = 0.15$ sample before and after annealing respectively, as well as a decrease in dislocation density after annealing. The broadening of the $(ZnO)_{1-x}(GaN)_x$ (0002) diffraction peak indicate that the alloy's crystal structure undergoes a change during the post-deposition annealing, where DFT calculations suggest Ga–N cluster-formation to be responsible for this observation.

Supporting Information

Supporting Information is available from the Wiley Online Library or from the author.

Acknowledgements

This work is funded by the Norwegian Research Council (NFR) and is acknowledged for the support to the SALIENT project, project number 239895/F20. NFR is also acknowledged for the projects PVLife, NFR project 243642 and FUNDAMENT, NFR project 251131. The Research Council of Norway is also acknowledged for the support to the Norwegian Micro- and Nano-Fabrication Facility, NorFab, project number 245963/F50 and the Norwegian Center for Transmission Electron Microscopy, NORTEM, project number 19705/F50. We acknowledge access to high-performance computing resources through the Norwegian and Swedish infrastructures NOTUR and SNIC, as well as through DECI within the Partnership for Advanced Computing in Europe.

Conflict of Interest

The authors declare no conflict of interest.

Keywords

alloying, annealing, density functional theory (DFT), magnetron sputtering, substrate dependency, thin films

Received: September 29, 2018
Revised: April 9, 2019
Published online:

[1] A. Janotti, C. G. Van de Walle, *Rep. Prog. Phys.* **2009**, *72*, 126501.
[2] K. Maeda, K. Teramura, D. Lu, T. Takata, N. Saito, Y. Inoue, K. Domen, *Nature* **2006**, *440*, 295.
[3] J. Liu, M. V. Fernández-Serra, P. B. Allen, *Phys. Rev. B* **2016**, *93*, 1.
[4] L. L. Jensen, J. T. Muckerman, M. D. Newton, *J. Phys. Chem. C* **2008**, *112*, 3439.
[5] S. H. Wei, A. Zunger, *Phys. Rev. B* **1988**, *37*, 8958.
[6] C. D. Valentin, *J. Phys. Chem. C* **2010**, *114*, 7054.
[7] M. N. Huda, Y. Yan, S. H. Wei, M. M. Al-Jassim, *Phys. Rev. B* **2008**, *78*, 195204.
[8] S. Wang, L. W. Wang, *Phys. Rev. Lett.* **2010**, *104*, 1.
[9] K. Maeda, K. Teramura, T. Takata, M. Hara, N. Saito, K. Toda, Y. Inoue, H. Kobayashi, K. Domen, *J. Phys. Chem. B* **2005**, *109*, 20504.
[10] K. Maeda, K. Domen, *Chem. Mater.* **2010**, *22*, 612.
[11] H. Chen, L. Wang, J. Bai, J. C. Hanson, J. B. Warren, J. T. Muckerman, E. Fujita, J. A. Rodriguez, *J. Phys. Chem. C* **2010**, *114*, 1809.
[12] V. S. Olsen, K. Bazioti, A. Azarov, B. G. Svensson, A. Kuznetsov, O. Prytz, L. Vines, *Semicond. Sci. Technol.* **2019**, *34*, 1.
[13] C. Yang, Y. Hirose, T. Wakasugi, N. Kashiwa, H. Kawai, K. Yamashita, T. Hasegawa, *Phys. Rev. Appl.* **2018**, *10*, 1.
[14] M. Mapa, K. S. Thushara, B. Saha, P. Chakraborty, C. M. Janet, R. P. Viswanath, C. M. Nair, K. V. G. K. Murty, C. S. Gopinath, *Chem. Mater.* **2009**, *21*, 2973.
[15] J. Li, B. Liu, A. Wu, B. Yang, W. Yang, F. Liu, X. Zhang, V. An, X. Jiang, *Inorg. Chem.* **2018**, *57*, 5240.
[16] S. Shet, Y. Yan, J. Turner, M. Al-Jassim, *J. Power Sources* **2013**, *232*, 74.
[17] L. Li, J. T. Muckerman, M. S. Hybertsen, P. B. Allen, *Phys. Rev. B* **2011**, *83*, 134202.
[18] J. P. Perdew, K. Burke, M. Ernzerhof, *Phys. Rev. Lett.* **1996**, *77*, 3865.
[19] J. P. Perdew, K. Burke, M. Ernzerhof, *Phys. Rev. Lett.* **1997**, *78*, 1396.
[20] P. E. Blöchl, *Phys. Rev. B* **1994**, *50*, 17953.
[21] G. Kresse, D. Joubert, *Phys. Rev. B* **1999**, *59*, 1758.
[22] A. R. Denton, N. W. Ashcroft, *Phys. Rev. A* **1991**, *43*, 3161.
[23] P. Fons, K. Iwata, S. Niki, A. Yamada, K. Matsubara, *J. Cryst. Growth* **1999**, *201–202*, 627.
[24] Y. Chen, D. M. Bagnall, H. J. Koh, K. T. Park, K. Hiraga, Z. Zhu, T. Yao, *J. Appl. Phys.* **1998**, *84*, 3912.
[25] D. Singh, R. Kumar, T. Ganguli, S. S. Major, *Mater. Res. Express* **2017**, *4*, 096405.
[26] M. A. Moram, M. E. Vickers, *Rep. Prog. Phys.* **2009**, *72*, 1.
[27] P. Scherrer, *Nachrichten von der Gesellschaft der Wissenschaften zu Göttingen, Mathematisch-Physikalische Klasse,* pp. 98–100, **1918**.
[28] K. Maeda, K. Teramura, K. Domen, *J. Catal.* **2008**, *254*, 198.
[29] M. Dou, G. Baldissera, C. Persson, *Int. J. Hydrogen Energy* **2013**, *38*, 16727.
[30] J. Liu, L. S. Pedroza, C. Misch, M. V. Fernández-Serra, P. B. Allen, *J. Phys.: Condens. Matter* **2014**, *26*, 1.

© 2019 WILEY-VCH Verlag GmbH & Co. KGaA, Weinheim

Supplemental Materials

The supplementary materials includes data that has not been included in the main article. Structurally, TEM images, RBS measurements and the measured FWHM from the rocking curve scans are included.

Figure S1 illustrates the $(ZnO)_{0.85}(GaN)_{0.15}/Al_2O_3$ heterostructure recorded under two-beam conditions with g0002 (a) before and (b) after post-deposition annealing. It is evident that in the case of the as-grown sample there is a high density of c-type TDs that is clearly decreased after annealing. It is worth noting that the comparison was made in areas having the same thickness along the viewing direction. The thickness was evaluated working in EELS-STEM, according to the $t/\lambda = \ln(I_t/I_0)$, where t is the thickness, λ the inelastic mean free path, I_t the intensity of the entire spectrum and I_0 the intensity of the zero loss peak. Figure S2 illustrates a high-resolution HAADF-STEM

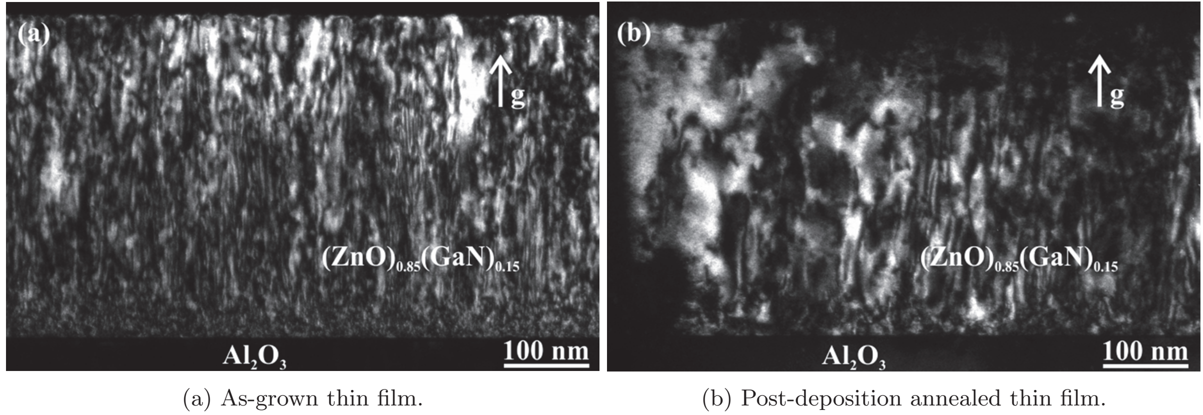

(a) As-grown thin film.

(b) Post-deposition annealed thin film.

FIG. S1: The $(ZnO)_{0.85}(GaN)_{0.15}$ composition measured using the weak-beam dark field g/3g method to investigate the dislocation density.

image of the $(ZnO)_{0.85}(GaN)_{0.15}$ thin film deposited on Al_2O_3 substrate after annealing at 800 °C, recorded along the $[11\bar{2}0]$ zone axis. By comparing this film wo the as-grown one (not shown here), the stacking sequence along the [0001] direction is retained following the ABABAB stacking of the hexagonal structure after annealing, indicating no structural change. Furthermore, imaging in both TEM and STEM-mode did not reveal any Moiré fringes. Since in HAADF-STEM image the intensity is proportional to the atomic number and the thickness of the sample, the dark areas correspond to areas with lower Z. RBS measurements in random and channeling modes were undertaken for the $x = 0.15$ as-deposited and annealed samples, see Figure S3. The depth scale of 3.8 nm/channel is also depicted in the figure. Notably, the density of the films was assumed to be similar to pure ZnO (8.3×10^{22} at/cm^3) and the depth scale was found to be identical for Zn and Ga atoms due to similarity in masses. The channeled spectra for the 800°C annealed film (blue) almost resembles the as-grown one, indicating that the thermal heat treatment does not lead to a substantial improvement of the disorder, as measured by RBS. In turn, minor changes can be attributed to the defect reconstruction and increase in grain size as clearly demonstrated by TEM results.

As for the rocking curve scans, the FWHM of the rocking curve scans was measured after each annealing step (as-grown, annealed at 600°C, 700°C and 800°C). The measured FWHM for the different compositions as a function of annealing temperature can be seen in Figure S4.

Optically, the measured transmittance for $x = 0.0$, $x = 0.02$ and $x = 0.15$ can be seen as a function of wavelength in Figure S5.

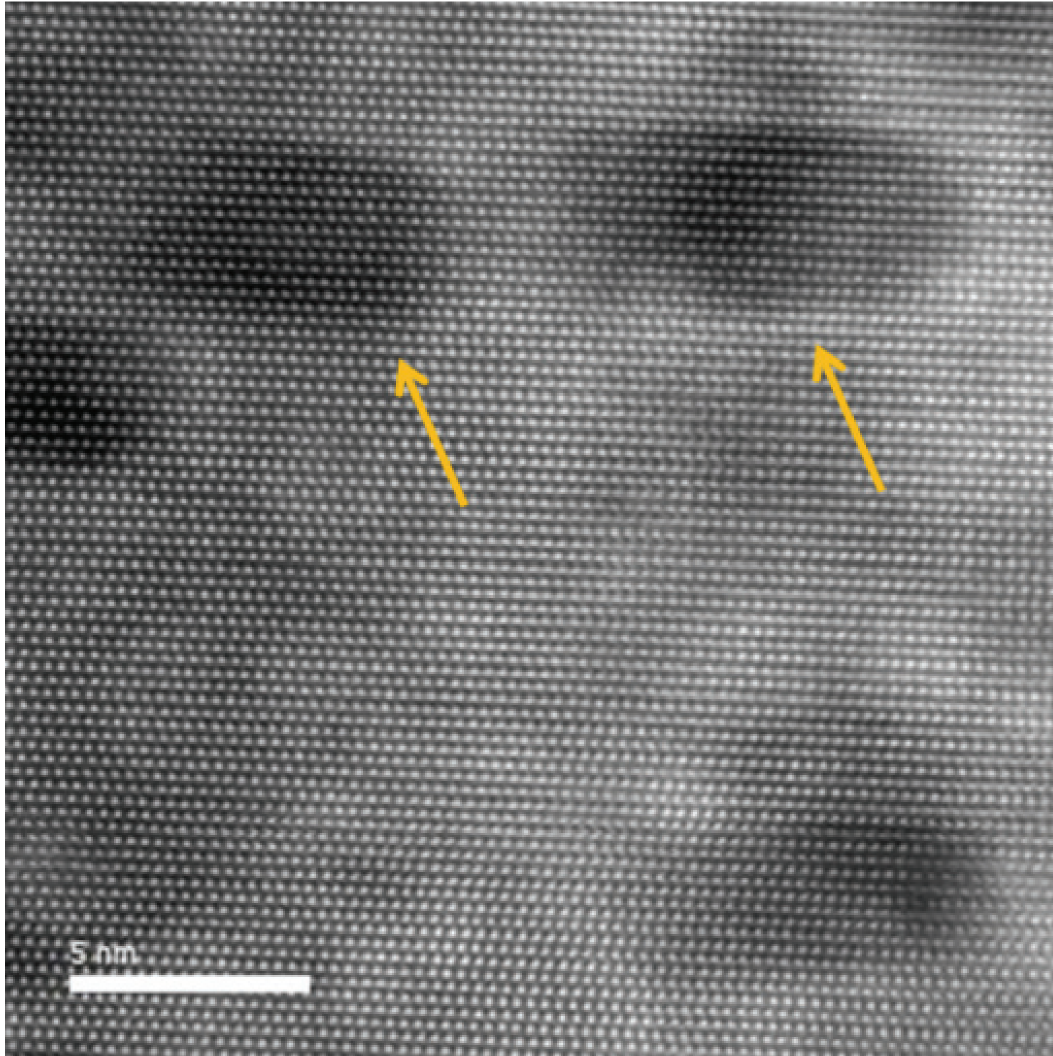

FIG. S2: High-resolution HAADF-STEM image along the [11$\bar{2}$0] z.a. of the $(ZnO)_{0.85}(GaN)_{0.15}$ thin film on Al_2O_3 substrate after annealing at 800 °C. The yellow arrows marks the voids observed in the films.

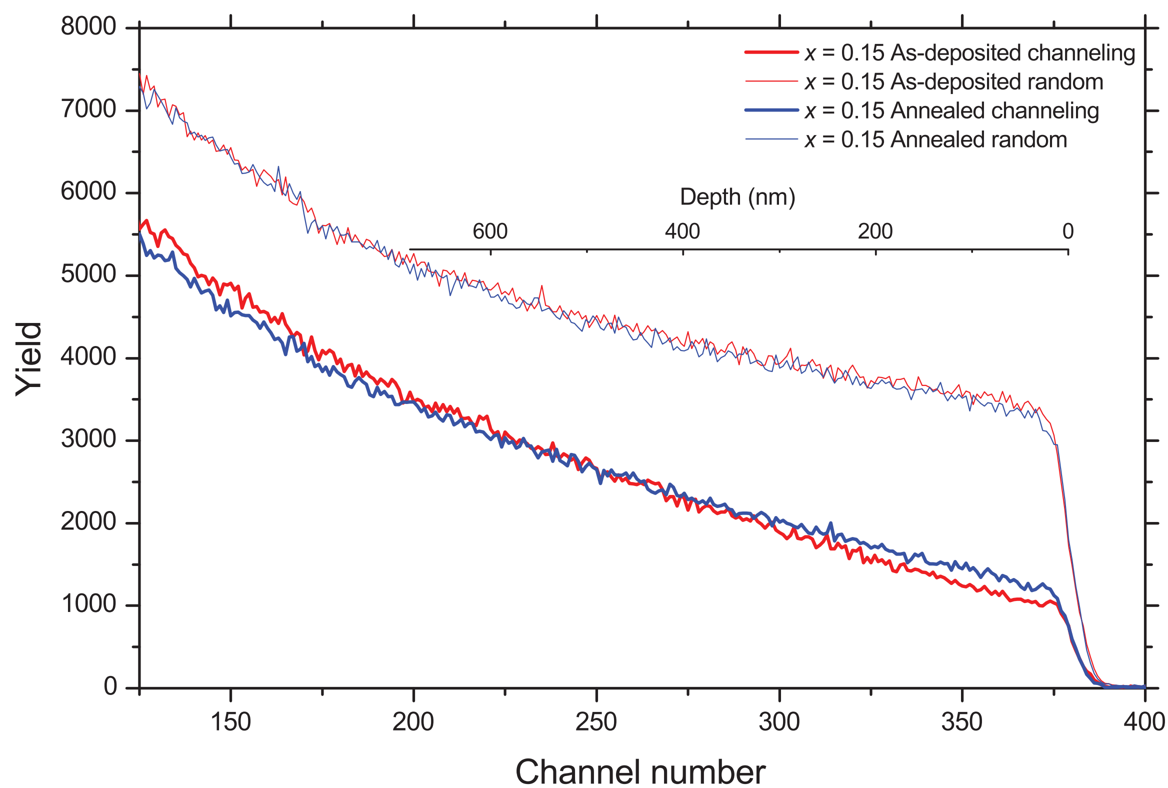

FIG. S3: RBS spectra acquired in random and channeling modes. The thick lines represent measurements done in channeling mode, while the thin ones represent random mode. The film surface is at channel 379, and the depth scale is included in the panel.

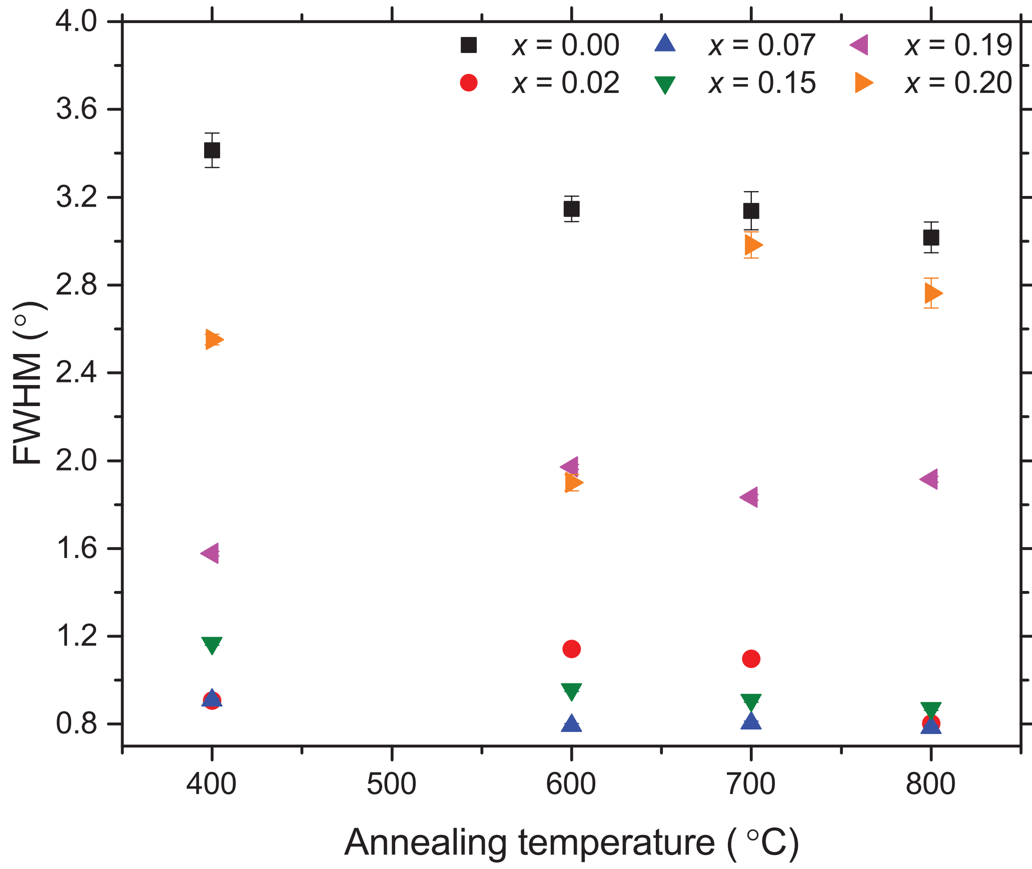

FIG. S4: FWHM of the (0002) reflection measured with rocking curve scans as a function of post-deposition annealing temperature for different alloy compositions.

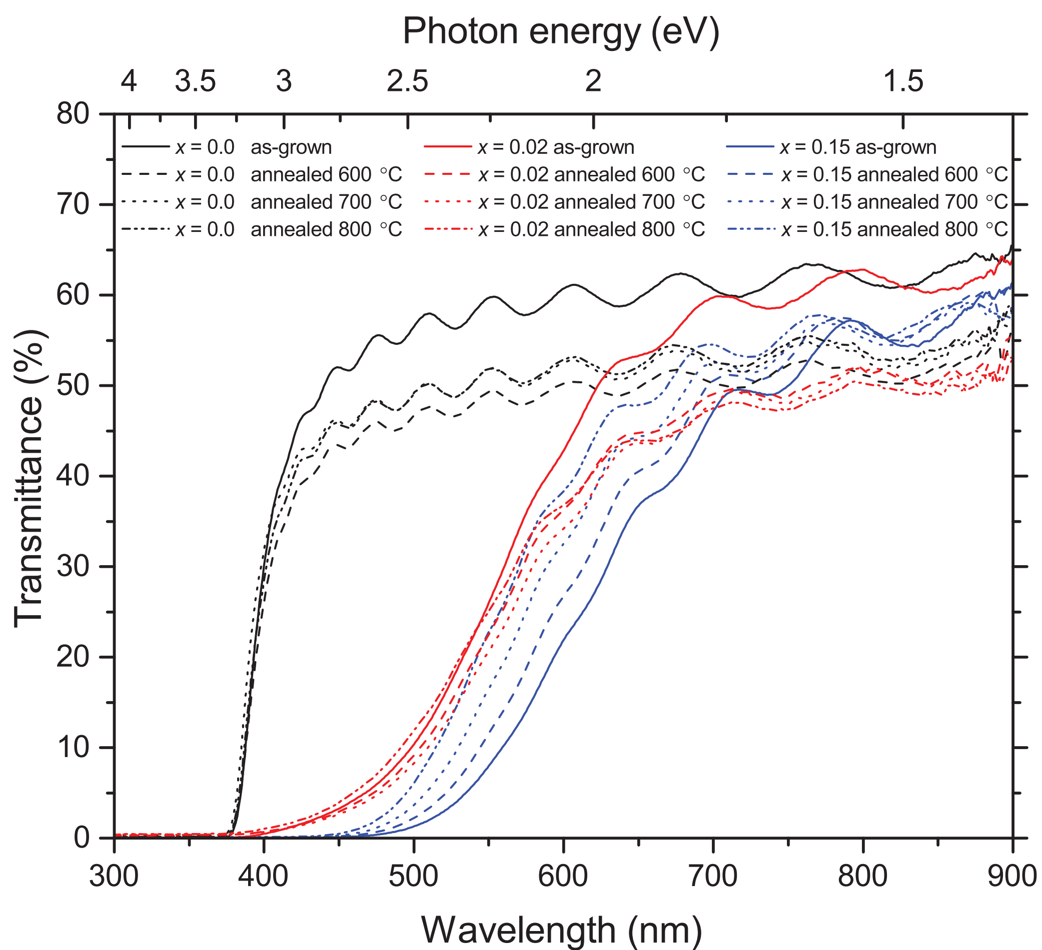

FIG. S5: Measured transmittance as a function of wavelength for three compositions $x = 0.0$, 0.02 and 0.15.

Paper III

Evidence of defect band mechanism responsible for band gap evolution in $(ZnO)_{1-x}(GaN)_x$ alloys

---

V. S. Olsen, G. Baldissera, C. Zimmermann, C. S. Granerød, C. Bazioti, A. Galeckas, B. G. Svensson, A. Yu. Kuznetsov, C. Persson, Ø. Prytz and L. Vines

Physical Review B 100, 165201 (2019)

My contribution: Planning and coordinating experiments, XRD and UV-VIS measurements, analysing results, and writing manuscript.

Evidence of defect band mechanism responsible for band gap evolution in $(ZnO)_{1-x}(GaN)_x$ alloys

V. S. Olsen,[1] G. Baldissera,[2] C. Zimmermann,[1] C. S. Granerød,[1] C. Bazioti,[1] A. Galeckas,[1] B. G. Svensson,[1] A. Yu. Kuznetsov,[1] C. Persson,[1,2] Ø. Prytz,[1] and L. Vines[1]

[1]*Department of Physics, Center for Materials Science and Nanotechnology, University of Oslo, P. O. Box 1048, Blindern, N-0316 Oslo, Norway*

[2]*Department of Materials Science and Engineering, KTH Royal Institute of Technology, SE-100 44 Stockholm, Sweden*

(Received 20 May 2019; revised manuscript received 30 August 2019; published 4 October 2019)

It is known that $(ZnO)_{1-x}(GaN)_x$ alloys demonstrate remarkable energy band bowing, making the material absorb in the visible range, in spite of the binary components being classical wide band gap semiconductors. However, the origin of this bowing is not settled; two major mechanisms are under debate: Influence of the orbital repulsion and/or formation of a defect band. In the present work, we applied a combination of the absorption and emission measurements on the samples exhibiting an outstanding nanoscale level of $(ZnO)_{1-x}(GaN)_x$ homogeneity as monitored by the high resolution electron microscopy equipped with the energy dispersive x-ray analysis and the electron energy loss spectroscopy; moreover the experimental data were set in the context of the computational analysis of the alloys employing density functional theory and quasiparticle *GW* approximation. A prominent discrepancy in the band gap values as deduced from the absorption and emission experiments was observed systematically for the alloys with different compositions and interpreted as evidence for the absorption gap shrinking due to the defect band formation. Computational data support the argument, revealing only minor variations in the bulk of the conduction and valence band structures of the alloys, except for a characteristic "tail" in the vicinity of the valence band maximum. As such, we conclude that the energy gap bowing in $(ZnO)_{1-x}(GaN)_x$ alloys is due to the defect band formation, presumably at the top of the valence band maximum.

DOI: 10.1103/PhysRevB.100.165201

I. INTRODUCTION

Due to the band bowing effect, the optical absorption of the $(ZnO)_{1-x}(GaN)_x$ (ZOGN) alloy system can be tuned from the UV range well into the visible part of the spectrum [1,2]. This intriguing optical property makes the system interesting for photovoltaic and solar water-splitting applications. The band bowing effect occurs when the apparent band gap of the alloy is reduced as a function of composition, in a nonlinear fashion, with respect to the two unmodified materials. Various synthesis routes have been used to fabricate the ZOGN alloy, targeting the absorption tunability to meet the specific needs of different applications; for example nanowires were deposited using a sol-gel method [3] and high-temperature vapor-phase diffusion reactions [4], whereas pulsed-laser deposition [5] and magnetron sputtering [6] resulted in highly crystalline thin films. Solid solution synthesis was utilized to fabricate bulk samples for water-splitting applications [1,7–9]. In previous work, density functional theory (DFT) has been employed to investigate the origin of the band bowing effect observed for the ZOGN alloys; specifically repulsion between the N 2*p* and Zn 3*d* orbitals [10–13] and type II band alignment [14,15] were suggested as possible explanations; in its turn Hirai *et al.* suggested that the absorption of visible light occurs via Zn-related acceptor levels [16].

While several theoretical explanations for the origin of the observed band bowing effect in the ZOGN have been discussed in the literature [10–15], experimental investigations of the mechanisms governing the band bowing effect are rather limited. Yang *et al.* combined transmission and reflection measurements with DFT calculations, finding that the absorption spectra do not match with the direct band gap Tauc plots and explained this observation with localization of the valence band maximum (VBM) on N atoms bonded with Zn [5]. Hirai *et al.* used photoluminescence (PL) in the wavelength range of 400–800 nm (3.1–1.55 eV) to argue that Zn-acceptor levels in GaN are responsible for the absorption in the visible range [16]. However, the majority of the experimentally obtained band gap energies were extracted from transmission and/or reflectance measurements, while other type of band gap measurements employing complementary techniques have rarely been applied to ZOGN.

In the present work we investigate the band bowing effect in highly crystalline thin films of ZOGN deposited by magnetron sputtering. Band gaps were extracted using both photon absorption and electron energy loss spectra and compared to emission measurements. Furthermore, we use DFT together with the beyond-DFT hybrid functional HSE06 and quasiparticle *GW* approximation to investigate the absorption, density of states (DOS), and band structure of the alloy in order to gain better understanding of the physical mechanisms responsible for the observed band bowing effect.

II. EXPERIMENTAL DETAILS

ZOGN thin films with different GaN content *x* were synthesized using RF magnetron sputtering on *c*-plane Al_2O_3 substrates. During sputtering, the voltage was simultaneously applied to two separate targets: ZnO (99.99% purity) and GaN (99.99% purity). Both Ar and N_2 were mixed in the

 ©2019 American Physical Society

chamber to tune the stoichiometry of the films. To obtain $x = 0.02$, 30 and 7 W were applied to the ZnO and GaN targets, respectively, while the Ar and N_2 flows were set to 12.5 and 0.7 sccm, respectively. For $x = 0.15$, the parameters were adjusted to 30 W (ZnO), 20 W (GaN), 12.5 sccm (Ar), and 5 sccm (N_2)—for the summary of the synthesis details, see Table I in the Supplemental Material [17]. A substrate temperature at 400 °C and rotation at 11 rpm was used for all depositions. The growth duration was adjusted to obtain film thickness of ~1.5 μm. Post-deposition isochronal anneals at 600, 700, and 800 °C in nitrogen atmosphere were employed to improve structural and optical properties. More detailed descriptions of the sample preparation, annealing, and structural characterization can be found elsewhere [6,18].

The optical transmission measurements were carried out using the Shimadzu SolidSpec-3700 DUV spectrophotometer. The instrument utilizes a grating monochromator, as well as a range of detectors. The wavelength range of this instrument is 175–2600 nm, with a resolution of 0.1 nm. The measured transmittance curves were corrected for the spectral response of the instrument. The PL measurements were performed at 10 K keeping the samples inside a continuously pumped Janis Research helium refrigerator. The following continuous-wave excitation sources were used for the measurements: He-Cd laser (325 nm, nominal optical power approximately 5 mW, IK Series from Kimmon), Ar laser (488 nm, nominal optical power approximately 5 mW, from Melles Griot), and solid-state laser (405 nm, nominal optical power approximately 5 or 100 mW, from Oxxius). The PL emission was collected by a microscope, and afterwards either directed into the imaging spectrometer (Horiba Jobin Yvon, iHR320) coupled to a CCD camera (Luca DL-658M EMCCD from Andor), or into an optical fiber connected to a spectrometer (USB4000 from Ocean Optics) acting as two different detectors. The wavelength resolution in both cases was approximately 2–3 nm. Low-pass filters were used for the laser sources with excitation wavelengths of 488 and 405 nm in order to prevent scattered laser light from entering into the detection path. A correction scheme was used to transfer the measured data to PL intensity vs photon energy, instead of the PL intensity vs wavelength [19]. In addition, the PL spectra were also corrected for an exponential background originating from the scattered laser light entering the detection path even though low-pass filters were employed. PL data were collected as a function of excitation power using a neutral density filter wheel.

Samples were prepared for transmission electron microscopy (TEM) investigations as cross-section wedges by standard cutting, grinding, and polishing methods. Final sample thinning by Ar ion milling was done using the Gatan PIPS II. Prior to the TEM experiments, the samples were plasma cleaned using the Fishione Model 1020. TEM investigation, scanning TEM (STEM) imaging, energy dispersive x-ray (EDX) analysis, and electron energy loss spectroscopy (EELS) were performed using a FEI Titan G2 60-300 kV TEM, equipped with a monochromator, a CEOS DCOR probe-corrector, and Super-X EDX detectors. All STEM imaging and EDX investigations were performed at an acceleration voltage of 300 kV with a probe convergence angle of 21 mrad and a resulting spatial resolution of approximately 0.08 nm. For band gap measurements in EELS an acceleration voltage of 60 kV was used to reduce relativistic effects that might otherwise mask the band gap signal [20]. The spectra were acquired using a Gatan GIF 965 spectrometer, with a collection angle of approximately 20 mrad. A full with half maximum of the EELS zero-loss peak (ZLP) of 0.13 eV was achieved, and the data for different samples were calibrated by aligning all ZLPs. Applying principal component analysis (PCA) [21] with 25 components, the noise in the EELS signal was reduced and the background was subtracted using a decaying power-law model [22].

III. COMPUTATIONAL METHODS

The computations of the ZOGN alloys were based on the DFT using the hybrid functional HSE06 and quasiparticle *GW* approximation, i.e., the method employing the Green function and the screened Coulomb potential, using the VASP software package [23,24]. The hybrid functional HSE06 [25,26] uses 25% Fock short-ranged exact exchange in conjunction with the exchange and full correlation energy from the local DFT potential. The *GW* method relies on many-body self-consistent calculations where the independent single particle equation contains a self-energy term. In our calculations, the partial self-consistent method sc*GW*0 [27] was used, in which the screened dielectric function was kept constant while the Green functions were updated. A cut-off energy of 400 eV was used in the first two steps for the DFT and HSE06 parts, and a cutoff of 100 eV to describe the response function in the *GW* part. A 72-atom unit cell structure was modeled for the alloys. This somewhat small cell is justified by the fact that we study alloys (and not defects), and that we employ computationally expensive techniques which have the advantages to reproduce interesting optical features as well as to generate band gap energies much closer to the experimental results. From this cell, seven ZnO pairs where randomly exchanged by GaN pairs, giving a concentration of $x = 14/72 = 0.194 \approx 0.2$, as seen on the right-hand side in Fig. 1. Tests have been conducted with more than 30 different configurations. Within all the relaxed structures, the most thermodynamically stable

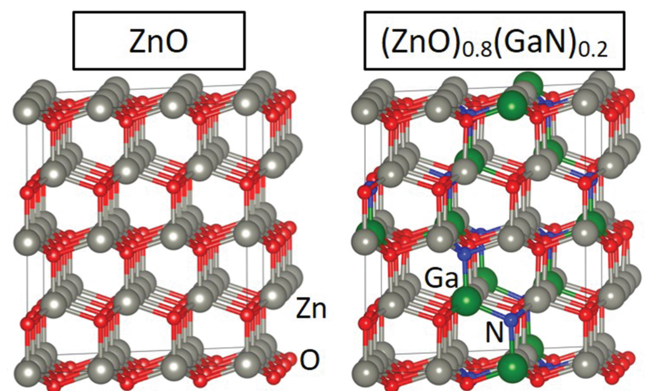

FIG. 1. Crystal structures for (left) binary ZnO and (right) for the most thermodynamic stable ZOGN alloy of the considered configurations with $x = 7/36 \approx 0.2$.

structures presented wider band gaps and more Ga-N bonds, with the final structures having an average close to 1.6 Ga-N bonds per GaN pair. A test with genetic algorithms [28] to find the best structure for the specific concentration, resulted in a configuration with total energy and band gap in the same range as the one presented. With this, only the most stable structure was selected for further simulation with the sc*GW*0 and the optical routines. Using a cut-off energy of 700 eV, the relaxation was done alternating between the volume and atom position relaxations, until the interaction remains <5 meV/Å. A Γ-centered k mesh of $2 \times 2 \times 2$ was used in all calculations. The data for energy dispersion (Fig. 7) were obtained with the PBE functional [29], though gap energy has been corrected to the results from the *GW* calculations. The optical properties were computed according to the linear response theory; the complex dielectric function were obtained from the optical matrix elements and the *GW* energies for direct transitions from valence to conduction bands [30]. The optical spectra were calculated with a 25 mV broadening. Our *GW* calculations overestimate the band gap of pure ZnO with $E_g(GW) = 3.66$ eV which is ∼0.3 eV higher experimental data; as such the calculated band gap energies were shifted to fit the experimental band gap of ZnO for better comparison (e.g., Figs. 3 and 8).

IV. RESULTS

A. Experimental results

The deposited ZOGN films consist of a highly crystalline single domain with no secondary or amorphous phases present, as seen in Figs. S1(c) and S1(d) in the Supplemental Material [17]. In addition, the films form an atomically sharp interface with the Al_2O_3 substrate, as seen in Fig. S1(a). Furthermore, EDX analyses indicated a homogeneous random alloy without elemental clustering at the meso- and nanoscale, as can be seen in Fig. S2 in the Supplemental Material [17].

Figure 2 shows the measured photon absorption and electron energy loss data for ZOGN films with $x = 0$, 0.02, and 0.15. Notably, the optical data in Fig. 2 are presented as Tauc plots assuming direct allowed transitions, while the EELS data are scaled linearly. A distinct shift towards lower energies is observed in Fig. 2 with a reference to $x = 0$, i.e., pure ZnO. Considering the optical data; $x = 0.02$ and 0.15 results in onset shifts of ∼0.3 and ∼0.8 eV, respectively, comparing to that of ZnO. These shifts can readily be attributed to a reduction of the band gap of the alloy relative to the binary compositions. The evolution of the EELS data resembles that of the optical absorption, especially for $x = 0$ and 0.15, thereby confirming the trend for the band gap reduction in the alloys. The tail of the optical absorption onset is normally related to disorder, localized states, or compensation [31,32]. In Fig. 2 the tails are more prominent for the optical absorption compared to the electron energy loss; altogether it may indicate a significant amount of localized states inside the band gap, compensation, or disorder. This prominently holds specifically for $x = 0.02$, where the optical absorption tail is significantly larger, indicating a high concentration of defects. Most importantly, the band gaps were estimated from the data in Fig. 2 (and similar data for $x = 0.07$, 0.19, 0.20 not shown) and used in further analysis.

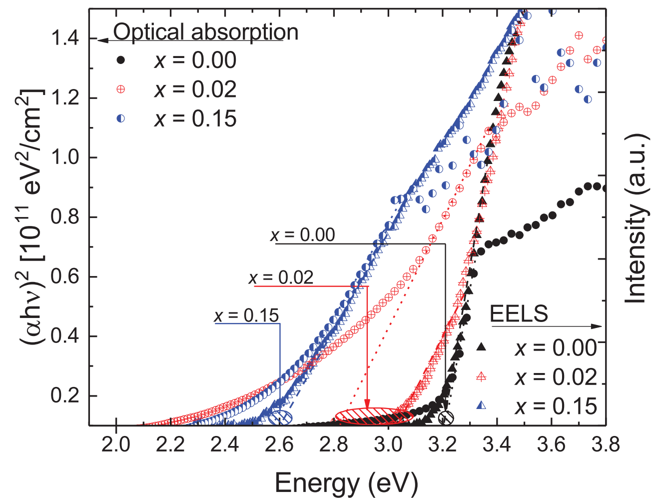

FIG. 2. Optical absorption and electron energy loss spectra for $x = 0$, 0.02, and 0.15—see corresponding symbols in the legend. The optical data are presented in the form of Tauc plots assuming direct allowed transitions, while the EELS data are linearly scaled. Dotted (optical absorption) and dashed (EELS) lines represents a extrapolation of the linear region intersecting the x axis. The point of intersection marks E_g.

The band gaps of the alloys as a function of composition are plotted in Fig. 3 together with the values calculated in the present study. In addition, the literature data are also included in Fig. 3 [2,8,9,33,34]. As shown in Fig. 3, a strong band gap reduction is observed at the initial stages of the alloying, terminated by a "plateau" at 2.6–2.4 eV. Notably, the calculated data predict a somewhat lower plateau of (2.4–2.2 eV). The general trends unveiled in our measurement are in accordance with the literature data displayed in Fig. 3, even though the lower x range has not been investigated

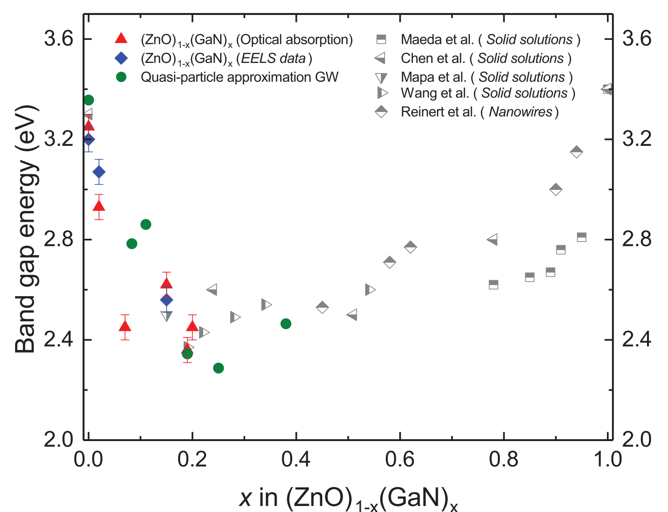

FIG. 3. The band gap magnitude as a function of x, as determined by the transmission measurements (filled triangles), STEM EELS (filled diamonds), and theory using *GW* approximation (filled circles). The results are compared to the literature data (partly filled symbols) [2,8,9,33,34].

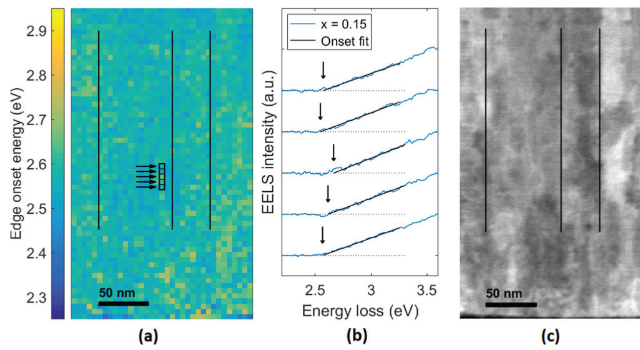

FIG. 4. STEM EELS data for $x = 0.15$; (a) the band gap map, (b) EELS signal onset at specific pixels as indicated by arrows in (a), and (c) a dark-field image of the band gap map area. The vertical black lines [in (a) and (c)] are to emphasize the presence of the grain boundaries.

that much previously. The strong band gap reduction with increasing alloy composition is observed for both the GaN- and ZnO-rich sides of Fig. 3, revealing a relatively flat region in between. To divide the band bowing effect into these three regions of different band gap reduction, i.e., low (high)-x regions with large E_g reduction and a more E_g-stable region in between, has also been proposed as a model explaining the band bowing effect for $(ZnO)_{1-x}(S)_x$ and $(ZnO)_{1-x}(Se)_x$ [35]. Opposing to the trends in Fig. 3, the $(ZnO)_{1-x}(S)_x$ alloys have also been found to yield a gradual variation of the band gap through a wider range of compositions [36–38].

The optical absorption and the EELS data in Fig. 2 probe regions of ~150 μm in diameter and 200×400 nm^2, respectively. The EELS data can also be presented in the form of spatially resolved maps discriminating ~5 nm pixels [39]. Figure 4 shows (a) an example of such map for $x = 0.15$, (b) onset for a number of pixels as indicated by arrows in the map, and (c) corresponding dark-field image of the mapped area of the sample. As seen already from the EELS map itself, i.e., Fig. 4(a), the distribution of the signal is quite homogeneous, even over the columnar grain boundaries [marked by the vertical lines for clarity in Figs. 4(a) and 4(c)]. Moreover, plotting the signals from several pixels, see Fig. 4(b), demonstrates a close to uniform energy loss onset among the pixels, as indicated by the vertical arrows. The maximum variance over the whole of the mapped area is ±0.25 eV. As such, these results indicate that the apparent band gap is the result of a homogeneous alloy, and not an average of a mixture of phases. Any such clustering or phase separation would have to be at length scales below ~5–10 nm. To further investigate potential cluster formation, STEM EDX analyses were performed. Figure 5 shows a nanoscale EDX map of an 26×26 nm^2 area and 0.4 nm pixel size for $x = 0.15$. Figure 5 reveals a random alloy, although a small inhomogeneity in the compositional distribution was observed, specifically by averaging the signals of four pixels (0.8×0.8 nm^2), However, according to the calculated standard deviations, only chemical variations higher than 20% could be detectable with this method, which does not seem to be the case. It might seem somewhat surprising that Ga-N pairs will form a cluster, considering that the defect pairs are isovalent to the ZnO host, and the Ga-N bond length is very similar to that of Zn-O. For example, the relaxation effect is very small when incorporating GaN; see Fig. 1. Of course, the trust to find a perfectly random alloy configuration with only isolated Ga-N pairs is ambiguous, and somewhat smaller clusters may not be excluded. Meanwhile, it has been demonstrated that formation of neutral and valence-conserving larger complexes is also driven by the octet rule for the atoms [40]. Indeed, theory predicts that the volume allowed each atom neighboring to a Ga-N pair does not perfectly match the octet rule; so that it is slightly more favorable that two Ga-N pairs form a complex to minimize the total deviation from the octet rule in the alloy.

Furthermore, PL data collected at an excitation wavelength of 325 nm (3.82 eV) are presented in Fig. 6 for $x = 0$, 0.02, and 0.15. All three samples reveal strong near-band emission (NBE) at 3.3–3.4 eV, corresponding to free- and acceptor-bound excitons, exhibiting the highest intensity at $x = 0.02$. The lower PL response for the $x = 0.15$ sample can be due to experimental conditions, as well as the sample containing more nonradiative defects. The pure ZnO film differs from the two alloy compositions in showing excitonic features related to donor- and acceptor-bound excitons, potentially originating from Ga and N acting as dopants in ZnO [41]. Such contaminations may arise from the deposition chamber, due to cross contamination from previous depositions. However, quite surprisingly no significant redshift in this NBE is observed in

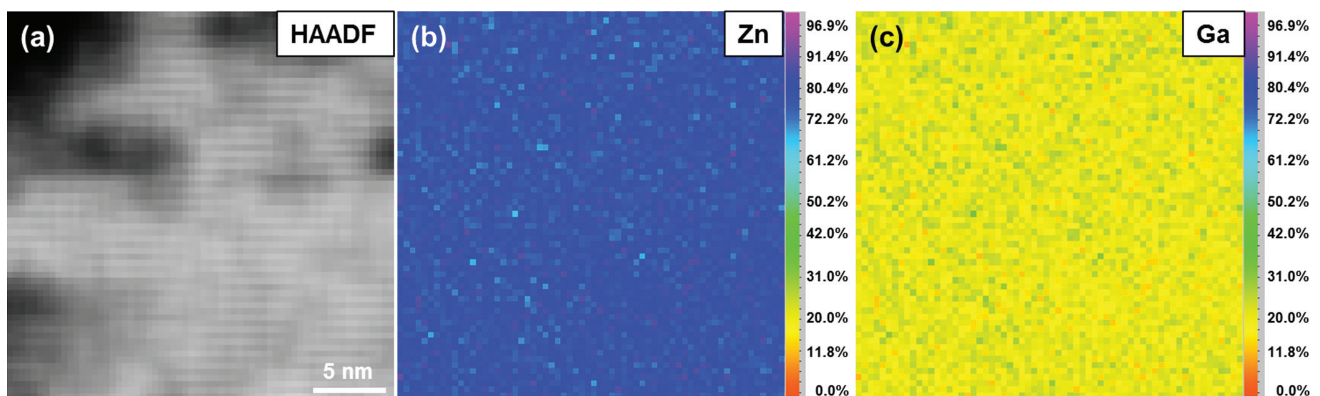

FIG. 5. (a) High-magnification HAADF-STEM image of the $x = 0.15$ thin film and the corresponding EDX maps of (b) Zn and (c) Ga atomic percent.

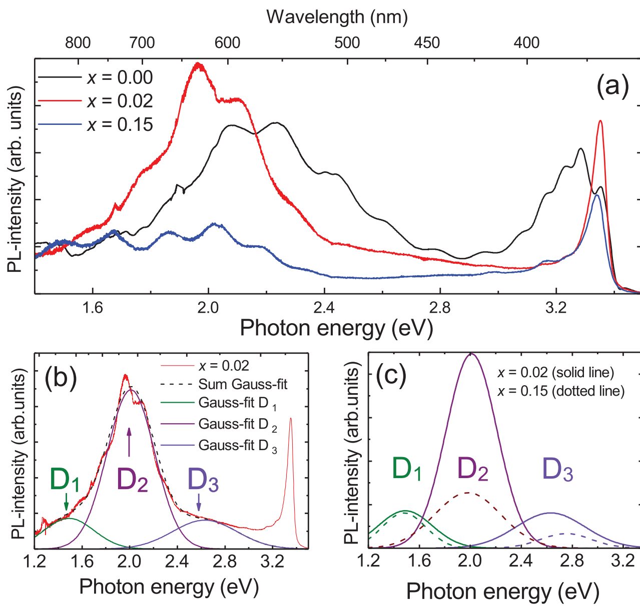

FIG. 6. (a) PL spectra recorded at 10 K for samples with different alloy compositions. (b) A deconvolution of the broad band emission part of the spectrum for $x = 0.02$. (c) The deconvoluted contributions for $x = 0.02$ (solid lines) and $x = 0.15$ (dotted lines).

Fig. 6(a) as a function of x; which might be expected based on the data in Figs. 2–4, where the shifting onset in optical absorption and EELS data are interpreted in terms of a reduction in the band gap. Interestingly, the NBE still resembles that of pure ZnO films originating from excitonic transitions, unveiling no further structure compared to pure ZnO. As it holds to the deep level emission of pure ZnO, it shows a broad band between 1.8 and 2.6 eV, where contributions from native defects in ZnO including V_O [42,43], O_i [44], and O_{Zn} [45], in addition to contributions from nitrogen-related defects, e.g., N_O [46] are expected. In its turn, the deep level emission of the alloys is significantly altered and was found to be modeled by three Gaussian-like contributions. The deconvoluted contribution for $x = 0.02$ are displayed in Fig. 6(b) revealing mean energy positions of 1.56–1.59 eV (D1), 1.81–1.98 eV (D2), and 2.23–2.46 eV (D3). The relative contributions of D1, D2, and D3 depends on x, as seen in Fig. 6(c). For example, the intensity of D1 is similar for both $x = 0.02$ and 0.15, whereas D2 is significantly more intense for the $x = 0.02$ thin film. To identify the origin of these dominant contributions, the PL intensity was measured for different excitation powers; indeed the PL intensity is known to follow the power law: $I_{PL} \sim P^k$, where $k > 1$ for band-to-band or excitonic emission and < 1 for emission related to defects [47]. Both D1 and D2 result in $k < 1$ for the $x = 0.02$ and $x = 0.15$ thin film, indicating that these emissions are indeed defect related. The energy positions of D1–D3 were also measured as a function of excitation wavelength, using excitation wavelengths of 325 nm (3.82 eV), 405 nm (3.06 eV), and 488 nm (2.54 eV) lasers, respectively (see Fig. S3 in the Supplemental Material [17]). Interestingly, the energy position of D1 was constant when increasing the excitation wavelength, whereas D2 and D3 shifted towards lower photon energies.

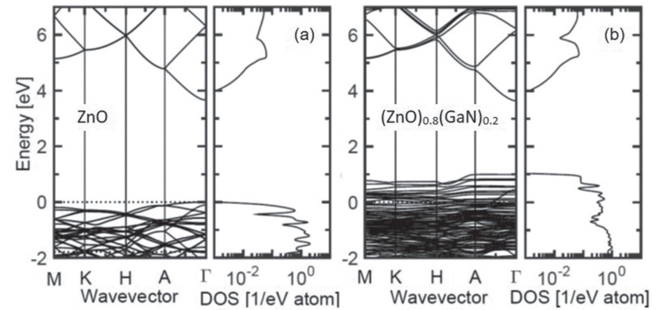

FIG. 7. Electronic band structures for (a) binary ZnO and (b) for the most thermodynamic stable ZOGN alloy with $x = 7/36 \approx 0.2$. Notice that the density-of-states (DOS) is presented on a logarithmic scale in order to better visualize the states near the conduction band minimum. The energy zero scale is set at the VBM of binary ZnO.

Summarizing experimental data, the evolution of the absorption onsets display a systematic and significant redshift, reaching ~0.8 eV at $x = 0.15$, see Figs. 2–4. This redshift was also found to be quite uniform over the sample, within the accuracy of the STEM EELS corresponding to 5 nm. On the other hand, the PL near-band-edge emission resembles that of pure ZnO, revealing no redshift as a function of the alloy composition. Meanwhile, the shapes of the PL near-band-edge and broad band emissions are quite different as a function of x.

B. Theoretical calculations

As mentioned above, the band gap energies obtained from our theoretical calculations are included in Fig. 3 (circles). These data represent estimates for the most stable configurations, however, not all possible configurations have been simulated and other configurations could potentially be more energetically favorable. Indeed, a strong band bowing effect, as seen from Fig. 3, is confirmed for $x \leqslant 0.25$; very importantly, in spite of significant experimental and theoretical uncertainties, the data are in a remarkable agreement.

The theoretical analysis of the electronic structure (see Fig. 7 showing the data for pure ZnO and ZOGN alloy with $x = 7/36 \approx 0.2$) reveals a fairly similar band structures and DOS. The band gap energy of the alloy is smaller, but the conduction bands are very similar, resembling that of ZnO. The main difference is the valence band structure, where the valence band maximum (VBM) of $x \approx 0.2$ [see Fig. 7(b)] lies ~1 eV above that of pure ZnO [see Fig. 7(a)]. The topmost bands become very flat in the alloy, especially in the (001) direction; this trend holds both for Γ-A and H-K symmetry lines. Therefore, the VBM for the $x \approx 0.2$ sample is at the A-point [0,0,1], whereas the conduction band minimum (CBM) is a the Γ point just like for pristine ZnO.

The absorption coefficient α of the ZOGN alloy for $x \approx 0.2$ was calculated directly from the complex dielectric function: $\alpha(\omega) = \omega/c[2 \mid \epsilon(\omega) \mid -2\epsilon_1(\omega)]^{1/2}$. Figure 8 shows the calculated absorption spectra of several selected concentrations. As seen from Fig. 8, there are no features indicating localized defect states from the GaN pairs; instead it reveals a smooth absorption as an average of α of the ZnO and GaN binary

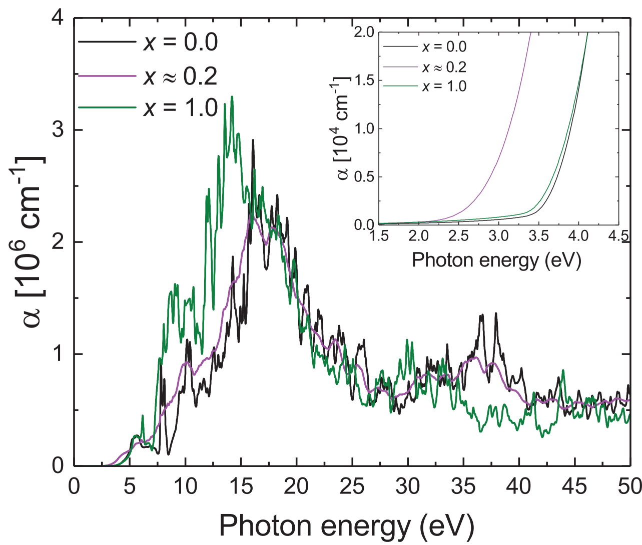

FIG. 8. Calculated absorption coefficients of ZOGN for $x = 0$, 0.2, and 1, obtained with the *GW* electronic structures. The inset shows the absorption coefficient in the region close to the band gap.

fractions. For the lower energy part of the data there are two main features: First, the remaining absorption peak around 5.5–6.5 eV present for both ZnO and GaN; second, the spectrum for $x \approx 0.2$ is shifted by ~1 eV towards lower energies (see inset in Fig. 8). This combination of two features indicates that ZOGN has a similar electronic structure as its binary constituents, however the effective band gap is changed by ~1 eV. From the electronic structure we know the energetically lowest energy transition for the $x \approx 0.2$ sample is the indirect transition from the highest occupied state at the *A* point to the lowest empty state at the Γ point. However, the energy for the indirect transition is only 30 meV smaller than the direct transition at the Γ point. While the optical transitions considers only direct transitions, the very flat topmost valence bands implies a stronger absorption near E_g. That is also seen in the absorption coefficient.

To further analyze the opposing results obtained from absorption and emission measurements (Figs. 2–4 versus Fig. 6), the partial atom-resolved density-of-states (PDOS) was calculated for $x \approx 0$, 0.02, and 0.2, where VBM of $x = 0$ is used as reference. The orbital-projected PDOS is presented in the Supplemental Material [17] (Fig. S4). Figure 9 shows both the total DOS for ZnO compared to that of ZOGN, as well as the PDOS of the Zn + O atoms and the Ga + N atoms for the alloy, for $x \approx 0.02$ in Fig. 9(a) and $x \approx 0.2$ in Fig. 9(b). In the upper panel of Fig. 9(a), the $x \approx 0.02$ shows DOS above the VBM of binary ZnO (dotted vertical line), which from the lower panel can be seen to originate from Ga and N orbitals. What is obvious from the PDOS is that Zn *d*-like states at about −6 eV are aligned between ZnO and ZOGN. Also the main character of the O *p*-like states are similar in ZnO and ZOGN. However, for the alloy, there is a clear contribution from rather localized Ga + N states in the energy region near the VBM. This is a consequence of the energetically higher N *p* states. The upper panel in Fig. 9(b) shows the total DOS for ZnO compared to that of $x \approx 0.2$, and the lower panel shows the PDOS for the Zn + O orbitals and Ga + N orbitals for the alloy. For this composition the DOS for the alloy is more intense and broader in the energy region above the VBM of ZnO (dotted vertical line). From the semicore states below −10 eV in Fig. 9(b) we estimate roughly the valence band offset (VBO) to be about 1 eV, which is expected since N *p* states are typically 1 eV higher in energy than O *p* states [48,49]. Again, there is a pronounced contribution from rather localized Ga + N states in the energy region near the VBM,

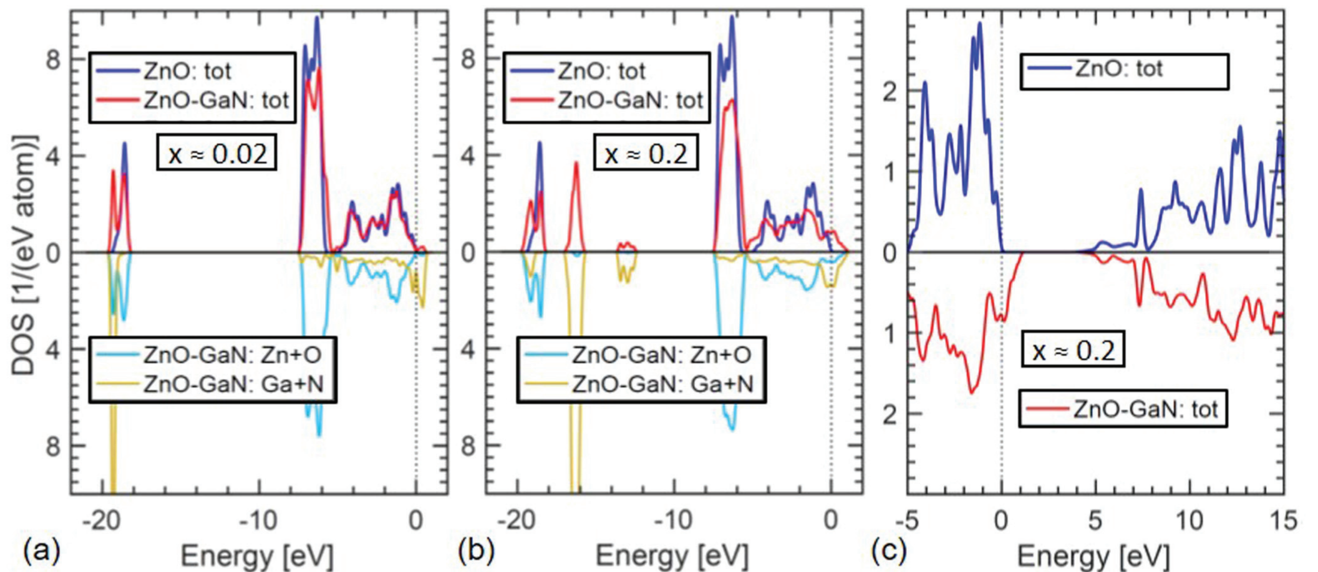

FIG. 9. (a) Total DOS of the valence and semicore states for $x = 0$ (blue) and $x \approx 0.02$ (red) in the upper panel, whereas the PDOS from Zn and O atoms (light blue) and Ga and N atoms (orange) in the $x \approx 0.02$ sample are shown in the lower panel. (b) Same as in (a) but for $x \approx 0.2$. (c) Total DOS for $x = 0$ (blue) and $x \approx 0.2$ (red), scaled to lower energies, in order to emphasize that the effect on the electronic structure due to GaN incorporation occurs mainly near the VBM. The dotted line indicates the VBM of pure ZnO.

originating from the energetically higher N p states, also observed for $x \approx 0.02$. These localized states explain why the topmost valence bands have the flat character (Fig. 7). A similar result has also been observed for the $ZnO_{1-x}S_x$ system, where the VBM has been found to consist of mainly Zn and S for $x > 0$, where S p states are energetically higher than the O p states [36].

In Fig. 9(c) the total DOS for $x = 0$ and $x \approx 0.2$ are again shown, but for the energy region relevant for optical absorption. With the VBO of about 1 eV, the main DOS peaks in both the valence bands and the conduction bands coincide for both compounds. The CBM is roughly at the same energy, and thus the band gap reduction of about 1 eV in the ZOGN alloy is caused by an upward shift in VBM. This gap reduction is in good agreement with our experimental results in Fig. 3 and our calculated absorption in Fig. 8.

V. DISCUSSION

The data in Sec. IV showed that a strong band bowing effect is observed in the ZOGN alloy, even at relatively modest Ga-N pair concentrations. Several theories have been proposed to explain the origin of the band bowing effect, while the two prevailing explanations are (i) the alloy valence band is pushed upward in energy due to orbital repulsion, and (ii) a defect band is formed within the band gap of the binary compound, effectively reducing the apparent optical band gap of the alloy. Starting with (i), one would expect that a shift of the VBM towards higher energies (upward) would cause the near-band-edge emission (NBE) measured in PL to occur at lower energies compared to that of binary ZnO, i.e., a gradual change in the energetic position of the NBE from that of pure ZnO towards lower energies. However, independently of x, the NBE remain similar to that of binary ZnO (Fig. 6). Furthermore, for other alloy materials with a strong band bowing effect, and where an upward shift of the VBM is expected to cause the band bowing, e.g., in $ZnO_{1-x}S_x$ alloys [36], a more gradual change in the band gap is observed [36] upon alloying, in contrast to the present results for ZOGN. Meanwhile, the explanation in terms of the hypothesis (ii), is in a better agreement with the experimental observations; indeed the defect band would not alter the NBE observed in PL, since the ZnO VBM to CBM transitions would remain a viable route for emission. Similar arguments can be put forth for the broad band emission, since the introduction of a defect band may not affect the energy position of the defect levels, opposite to what has been reported for defect levels following an upwards shift in VBM [36]. The fact that the energy position of the contributions D1–D3 remains unchanged in Fig. 6 is an additional argument in favor of (ii). Furthermore, the strong shift in the apparent band gap from ∼3.3 to ∼2.4 is in accordance with the introduction of a band with a specific energy arising in the material, where the apparent band gap absorption is related to a transition between conduction and defect bands. This further corroborates why no change in the absorption onset with increasing GaN content of the alloy is seen over the so called plateau in Fig. 3.

The theoretical calculations show a similar strong band gap reduction at modest GaN incorporations (i.e., below 25%), although not as rapid as the experimental measurements indicate. Figure 9 shows that the states at the VBM in the alloy composition mainly consist of states formed by N p-like orbitals, and that these DOS shift upward in energy and broaden, when increasing x from 0.02 to 0.2. Thus, N incorporation introduces defect states at a higher energy compared to that of binary ZnO (mainly arising from the O p orbitals), which can be interpreted as nitrogen-related defects forming a band at higher energy than the VBM of ZnO, in accordance with our experimental observations. Figure 7 display the calculated band structure of the binary ZnO and the ZOGN alloy with $x \approx 0.2$, normalized to the VBM. From Fig. 7 one can observe a significantly reduced dispersion of the valence band of the alloy compared to the binary ZnO, especially in the Γ-A direction. The reduced dispersion arises since states are not required to be degenerate at the A point for the alloy with lower crystallographic symmetry. Moreover, Fig. 7 indicates that an indirect transition has the lowest energy, as stated previously, with the top of the valence band at the A point.

VI. CONCLUSION

In conclusion, a significant redshift in both optical absorption and electron energy loss spectra is observed for the highly crystalline ZOGN thin films with $x \leqslant 0.20$. On the other hand, the measured near-band-edge emissions show no indication of the corresponding redshifts, still resembling what is expected for pure ZnO, as a result of acceptor-bound and free exciton interactions. This discrepancy is interpreted in terms of the defect band formed within the band gap, and being responsible for the absorption within the visible spectrum in the alloys. The theoretical arguments were in agreement with the experimental facts.

ACKNOWLEDGMENTS

This work is funded by The Research Council of Norway (RCN) and is acknowledged for the support to the SALIENT project, Project No. 239895/F20. RCN is also acknowledged for the projects PVLife, Project No. 243642 and FUNDAMENT, Project No. 251131. RCN is also acknowledged for the support to the Norwegian Micro- and Nano-Fabrication Facility, NorFab, Project No. 245963/F50 and the Norwegian Center for Transmission Electron Microscopy, NORTEM, Project No. 197405/F50. We acknowledge access to high-performance computing resources through the Norwegian and Swedish infrastructures NOTUR and SNIC, as well as through DECI within the Partnership for Advanced Computing in Europe.

[1] K. Maeda, K. Teramura, T. Takata, M. Hara, N. Saito, K. Toda, Y. Inoue, H. Kobayashi, and K. Domen, Overall water splitting on $(Ga_{1-x}Zn_x)(N_{1-x}O_x)$ solid solution photocatalyst: Relationship between physical properties and photocatalytic activity, J. Phys. Chem. B **109**, 20504 (2005).

[2] A. A. Reinert, C. Payne, L. Wang, J. Ciston, Y. Zhu, and P. G. Khalifah, Synthesis and characterization of visible light absorbing $(GaN)_{1-x}(ZnO)_x$ semiconductor nanorods, Inorg. Chem. **52**, 8389 (2013).
[3] W.-Q. Han, Y. Zhang, C.-Y. Nam, C. T. Black, and E. E. Mendez, Growth and electronic properties of GaN/ZnO solid solution nanowires, Appl. Phys. Lett. **97**, 083108 (2010).
[4] M. Zhong, Y. Ma, P. Oleynikov, K. Domen, and J.-J. Delaunay, A conductive ZnO-ZnGaON nanowire-array-on-a-film photoanode for stable and efficient sunlight water splitting, Energy Environ. Sci. **4**, 1693 (2014).
[5] C. Yang, Y. Hirose, T. Wakasugi, N. Kashiwa, H. Kawai, K. Yamashita, and T. Hasegawa, Epitaxy of $(GaN)_{1-x}(ZnO)_x$ Solid-Solution Thin Films with Widely Tunable Chemical Composition and Strong Visible Absorption, Phys. Rev. Appl. **10**, 044001 (2018).
[6] V. S. Olsen, C. Bazioti, A. Azarov, B. G. Svensson, A. Kuznetsov, Ø. Prytz, and L. Vines, Bandgap bowing in crystalline $(ZnO)_{1-x}$ $(GaN)_x$ thin films; influence of composition and structural properties, Semicond. Sci. Technol. **34**, 015001 (2019).
[7] K. Maeda and K. Domen, Solid solution of GaN and ZnO as a stable photocatalyst for overall water splitting under visible light, Chem. Mater. **22**, 612 (2010).
[8] H. Chen, L. Wang, J. Bai, J. C. Hanson, J. B. Warren, J. T. Muckerman, E. Fujita, and J. A. Rodriguez, In situ XRD studies of ZnO/GaN mixtures at high pressure and high temperature: Synthesis of Zn-rich $(Ga_{1-x}Zn_x)(N_{1-x}O_x)$ photocatalysts, J. Phys. Chem. C **114**, 1809 (2010).
[9] M. Mapa, K. S. Thushara, B. Saha, P. Chakraborty, C. M. Janet, R. P. Viswanath, C. M. Nair, K. V. G. K. Murty, and C. S. Gopinath, Electronic structure and catalytic study of solid solution of GaN in ZnO, Chem. Mater. **21**, 2973 (2009).
[10] J. Liu, M. V. Fernández-Serra, and P. B. Allen, Special quasiordered structures: Role of short-range order in the semiconductor alloy $(GaN)_{1-x}(ZnO)_x$, Phys. Rev. B **93**, 054207 (2016).
[11] L. L. Jensen, J. T. Muckerman, and M. D. Newton, First-principles studies of the structural and electronic properties of the $(Ga_{1-x}Zn_x)(N_{1-x}O_x)$ solid solution photocatalyst, J. Phys. Chem. C **112**, 3439 (2008).
[12] S. H. Wei and A. Zunger, Role of *d* states in II-VI semiconductors, Phys. Rev. B **37**, 8958 (1988).
[13] C. D. Valentin, Electronic structure of $(Ga_{1-x}Zn_x)N_{1-x}O_x$ photocatalyst for water splitting by hybrid hartree-fock density functional theory methods, J. Phys. Chem. C **114**, 7054 (2010).
[14] M. N. Huda, Y. Yan, S.-H. Wei, and M. M. Al-Jassim, Electronic structure of ZnO: GaN compounds: Asymmetric bandgap engineering, Phys. Rev. B **78**, 195204 (2008).
[15] S. Wang and W. Lin-Wang, Atomic and Electronic Structures of GaN/ZnO Alloys, Phys. Rev. Lett. **104**, 065501 (2010).
[16] T. Hirai, K. Maeda, M. Yoshida, J. Kubota, S. Ikeda, M. Matsumura, and K. Domen, Origin of visible light absorption in GaN-Rich $(Ga_{1-x}Zn_x)(N_{1-x}O_x)$ photocatalysts, J. Phys. Chem. C **111**, 18853 (2007).
[17] See Supplemental Material at http://link.aps.org/supplemental/10.1103/PhysRevB.100.165201 for a full survey table of all samples prepared for this study. In addition, high-resolution STEM images, STEM EDX analyses, TEM selected area diffraction patterns are presented to address the crystal quality and relative elemental composition. The deconvolution of PL spectra for $x = 0.15$ is shown, as well as the orbital-projected PDOS for ZnO, Zn and O atoms in ZOGN $x \approx 0.2$, and Ga and N atoms for ZOGN $x \approx 0.2$.
[18] V. S. Olsen, C. Bazioti, G. Baldissera, A. Azarov, O. Prytz, C. Persson, B. G. Svensson, A. Y. Kuznetsov, and L. Vines, Effects of substrate and post-deposition annealing on structural and optical properties of $(ZnO)_{1-x}(GaN)_x$ films, Phys. Status Solidi (b) **256**, 1800529 (2019).
[19] J. R. Lakowicz, *Principles of Fluorescence Spectroscopy*, 2nd ed. (Kluwer Academic/Plenum, Amsterdam, 1999).
[20] W. Zhan, C. S. Granerød, V. Venkatachalapathy, K. M. H. Johansen, I. J. T. Jensen, A. Yu. Kuznetsov, and Ø. Prytz, Nanoscale mapping of optical band gaps using monochromated electron energy loss spectroscopy, Nanotechnology **28**, 105703 (2017).
[21] M. Bosman, M. Watanbe, D. T. L. Alexander, and V. J. Keast, Mapping chemical and bonding information using multivariate analysis of electron energy-loss spectrum images, Ultramicroscopy **106**, 1024 (2006).
[22] C. S. Granerød, W. Zhan, and O. Prytz, Automated approaches for band gap mapping in STEM-EELS, Ultramicroscopy **184**, 39 (2018).
[23] P. E. Blöchl, Projector augmented-wave method, Phys. Rev. B **50**, 17953 (1994).
[24] G. Kresse and D. Joubert, From ultrasoft pseudopotentials to the projector augmented-wave method, Phys. Rev. B **59**, 1758 (1999).
[25] J. Heyd, G. E. Scuseria, and M. Ernzerhof, Hybrid functionals based on a screened Coulomb potential, J. Chem. Phys. **118**, 8207 (2003).
[26] A. V. Krukau, O. A. Vydrov, A. F. Izmaylov, and G. E. Scusiera, Influence of the exchange screening parameter on the performance of screened hybrid functionals, J. Chem. Phys. **125**, 224106 (2006).
[27] M. Shishkin, M. Marsman, and G. Kresse, Accurate Quasiparticle Spectra from Self-Consistent *GW* Calculations with Vertex Corrections, Phys. Rev. Lett. **99**, 246403 (2007).
[28] L. Vilhelmsen and B. Hammer, A generic algorithm for first principles global structure optimization of supported nano structures, J. Chem. Phys. **141**, 044711 (2014).
[29] J. P. Perdew, K. Burke, and M. Ernzerhof, Generalized Gradient Approximation Made Simple, Phys. Rev. Lett. **77**, 3865 (1996).
[30] M. Gajdoš, K. Hummer, G. Kresse, J. Furthmüller, and F. Bechstedt, Linear optical properties in the projector-augmented wave methodology, Phys. Rev. B **73**, 045112 (2006).
[31] E. O. Kane, Band tails in semiconductors, Solid-State Electron. **28**, 3 (1985).
[32] J. K. Katahara and H. W. Hillhouse, Quasi-Fermi level splitting and sub-bandgap absorptivity from semiconductor photoluminescence, J. Appl. Phys. **116**, 173504 (2014).
[33] K. Maeda, K. Teramura, D. Lu, T. Takata, N. Saito, Y. Inoue, and K. Domen, Photocatalyst releasing hydrogen from water, Nature (London) **440**, 295 (2006).
[34] J. P. Wang, B. Huang, Z. Wang, P. Wang, H. Cheng, Z. Zheng, X. Qin, X. Zhang, Y. Dai, and M.-H. Whangbo, Facile

synthesis of Zn-rich $(GaN)_{1-x}(ZnO)_x$ solid solutions using layered double hydroxides as precursors, J. Mater. Chem. **21**, 4562 (2011).

[35] G. Baldissera and C. Persson, Understanding the optical properties of $ZnO_{1-x}S_x$ and $ZnO_{1-x}Se_x$ alloys, J. Appl. Phys. **119**, 045704 (2016).

[36] C. Persson, C. Platzer-Björkman, J. Malmström, T. Törndahl, and M. Edoff, Strong Valence-Band Offset Bowing of $ZnO_{1-x}S_x$ Enhances *p*-Type Nitrogen Doping of ZnO-like Alloys, Phys. Rev. Lett. **97**, 146403 (2006).

[37] B. K. Meyer, A. Polity, B. Farangis, Y. He, D. Hasselkamp, T. Krämer, and C. Wang, Structural properties and bandgap bowing of $ZnO_{1-x}S_x$ thin films deposited by reactive sputtering, Appl. Phys. Lett. **85**, 4929 (2004).

[38] R. R. Thankalekshmi and A. C. Rastogi, Structure and optical band gap of $ZnO_{1-x}S_x$ thin films synthesized by chemical spray pyrolysis for application in solar cells, J. Appl. Phys. **112**, 063708 (2012).

[39] C. S. Granerød, A. Galeckas, K. M. Johansen, L. Vines, and O. Prytz, The temperature-dependency of the optical band gap of ZnO measured by electron energy-loss spectroscopy in a scanning transmission electron microscope, J. Appl. Phys. **123**, 145111 (2018).

[40] D. Huang and C. Persson, Band gap change induced by defect complexes in Cu_2ZnSnS_4, Thin Solid Films **535**, 265 (2013).

[41] L. Vines and A. Y. Kuznetsov, *Oxide Semiconductors* (Semiconductor and Semimetals, 2013), Vol. 88, pp. 67–99.

[42] T. M. Børseth, B. G. Svensson, A. Y. Kuznetsov, P. Klason, Q. X. Zhao, and M. Willander, Identification of oxygen and zinc vacancy optical signals in ZnO, Appl. Phys. Lett. **89**, 262112 (2006).

[43] D. M. Hofmann, D. Pfisterer, J. Sann, B. K. Meyer, R. Tena-Zaera, V. Munoz-Sanjose, T. Frank, and G. Pensl, Properties if the oxygen vacancy in ZnO, Appl. Phys. A **88**, 147 (2007).

[44] X. L. Wu, G. G. Siu, C. L. Fu, and H. C. Ong, Photoluminescence and cathodoluminescence studies of stoichiometric and oxygen-deficient ZnO films, Appl. Phys. Lett. **78**, 2285 (2001).

[45] B. Lin and Z. Fu, Green luminescent center in undoped zinc oxide films deposited on silicon substrates, Appl. Phys. Lett. **79**, 943 (2001).

[46] M. C. Tarun, M. Z. Iqbal, and M. D. McCluskey, Nitrogen is a deep acceptor in ZnO, AIP Adv. **1**, 022105 (2011).

[47] T. Schmidt, K. Lischka, and W. Zulehner, Excitation-power dependence of the near-band-edge photoluminescence of semiconductors, Phys. Rev. B **45**, 8989 (1992).

[48] T. D. Veal, P. D. C. King, S. A. Hatfield, L. R. Bailey, C. F. McConville, B. Martel, J. C. Moreno, E. Frayssinet, F. Semond, and J. Zúñiga-Pérez, Valence band offset of the ZnO/AIN heterojunction determined by x-ray photoemission spectroscopy, Appl. Phys. Lett. **93**, 202108 (2008).

[49] F. Oba and Yu. Kumagai, Design and exploration of semiconductors from first principles: A review of recent advances, Appl. Phys. Express **11**, 060101 (2018).

Supplemental Material

The supplementary materials includes data that has not been included in the main article. Table I shows a full description of the growth parameters used for sputtering for the different composition, x, $(ZnO)_{1-x}(GaN)_x$ thin films, including the film thicknesses, measured using ellipsometry.

TABLE I: Full survey of all samples prepared for this study, together with the growth parameters, as well as the measured film thicknesses using ellipsometry.

Conc.			**Power**	**Power**	**Flow**	**Flow**	**Thickness**
x	Ga at.%	N at.%	ZnO (W)	GaN (W)	Ar (SCCM)	N_2 (SCCM)	(nm)
0	0	0	30	0	12.5	0	1380
0.02	1.1±0.1	3.0±0.3	30	7	12.5	0.7	1110
0.07	3.5±0.2	3.4±0.3	30	10	12.5	0.7	1690
0.15	7.5±0.4	5.7±0.4	30	20	12.5	5	1330
0.19	9.5±0.5	6.5±0.5	20	20	10	20	1880
0.20	10.0±0.5	7.9±0.5	30	30	10	20	1290

The crystal quality and orientation relationship of the films with respect to the substrates were investigated by high-resolution STEM imaging and selected-area electron diffraction patterns (SAED) in TEM. Figure S1 shows a high-resolution HAADF-STEM image viewed along the $[11\bar{2}0]_{film}$ projection, close to the interface, along with the corresponding fast Fourier transform (FFT) diffractogram (inset). A film of high crystalline quality of wurtzite structure was verified, forming an atomically sharp interface with the c-Al_2O_3 substrate. SAED patterns show that both films are single domain with no secondary or amorphous phases, exhibiting a preferred orientation relationship with the substrate described by $[0001]_{ZOGN}//[0001]_{Al_2O_3}$ (out-of-plane) and $[11\bar{2}0]_{ZOGN}//[1\bar{1}00]_{Al_2O_3}$ (in-plane). This relationship implies a 30° in-plane rotation of the film unit cell with respect to that of the substrate (the so-called "alligned domain") in order to reduce the mismatch.

Energy dispersive x-ray (EDX) analysis was carried out in STEM-mode, to examine the relative elemental composition and homogeneity of the ZOGN alloys. Quantitative EDX maps of the atomic ratio (%) were extracted based on the relative intensity between the Zn-K and Ga-K spectral lines. The average elemental composition for the $x = 0.15$ film was very close to the nominal value, since the measured atomic ratio was 13.8_{Ga}:86.2_{Zn}. Similarly, for the $x =$ 0.02 film, the average measured atomic ratio was 2.8_{Ga}:97.2_{Zn}. Results are presented in Fig. S2, where an overall area of approximately 0.7×1.8 μm^2 was scanned with a 5 nm pixel size. Both low and high magnification EDX analysis showed that there is a rather homogeneous elemental distribution with no indication of phase separation phenomena and intense elemental clustering at meso- and nano-scale.

In Figure S3, the deep level emission from a thin film with $x = 0.15$ is displayed. The spectra were recorded at three different excitation wavelengths, i.e. 325 nm (~3.82 eV), 405 nm (~3.06 eV) and 488 nm (~2.54 eV). For an excitation wavelength of 325 nm, three contributions to the deep level PL spectra are observed, with similar energy positions as that of $x = 0.02$ (in the main article), i.e. 1.56 - 1.59 eV (D1), 1.81 - 1.98 eV (D2) and 2.23 - 2.46 eV (D3). Interestingly, the energy position of D1 remains constant, whereas that of D2 and D3 shifts towards lower photon energies, as the excitation wavelength is increased, i.e. the excitation occurs below the band gap of pure ZnO.

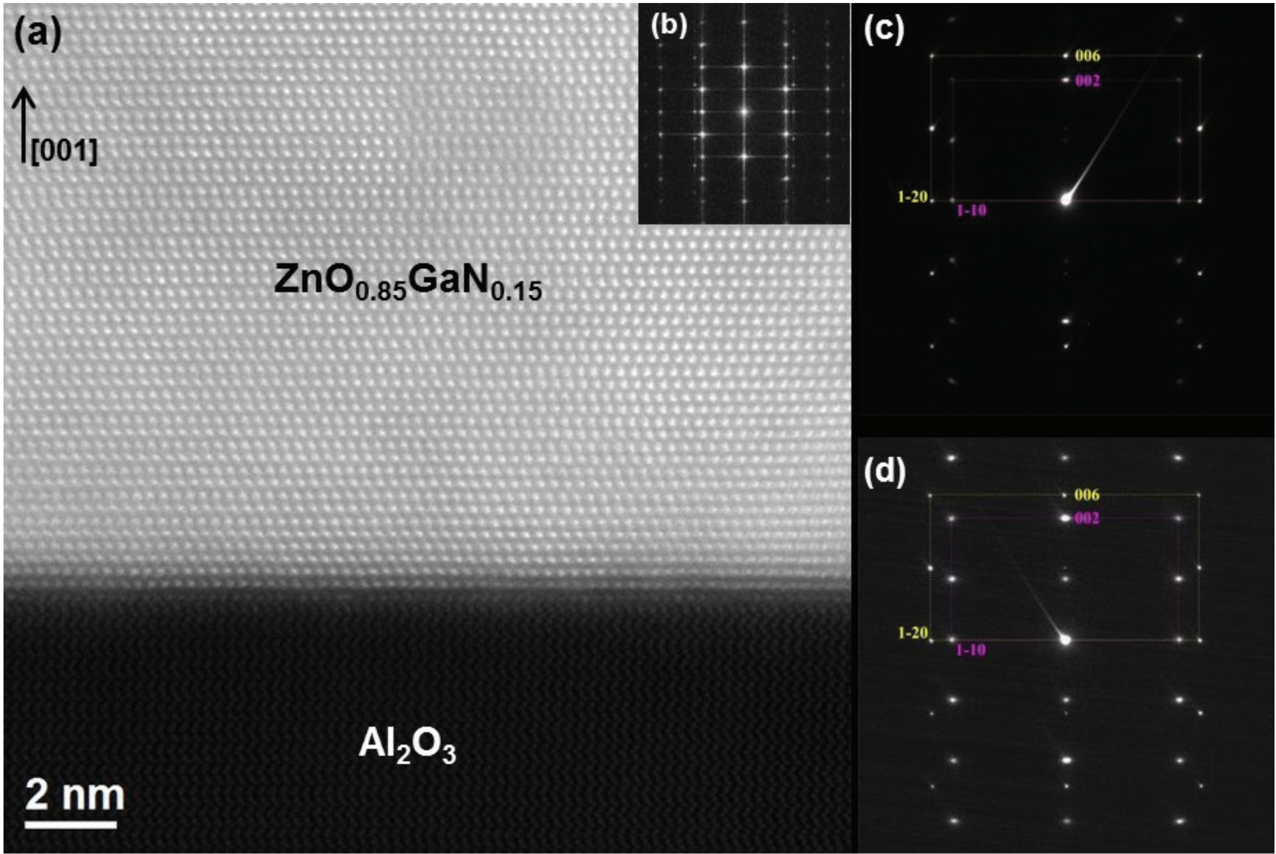

FIG. S1: (a) High resolution HAADF STEM image of the $x = 0.15$ thin film close to the interface and (b) the corresponding FFT diffractogram (inset), (c)-(d) SAED patterns of the $ZOGN_{0.15}/Al_2O_3$ and $ZOGN_{0.02}/Al_2O_3$ heterostructures, respectively. The high crystal quality of single-domain thin films is revealed, with no secondary or amorphous phases observed.

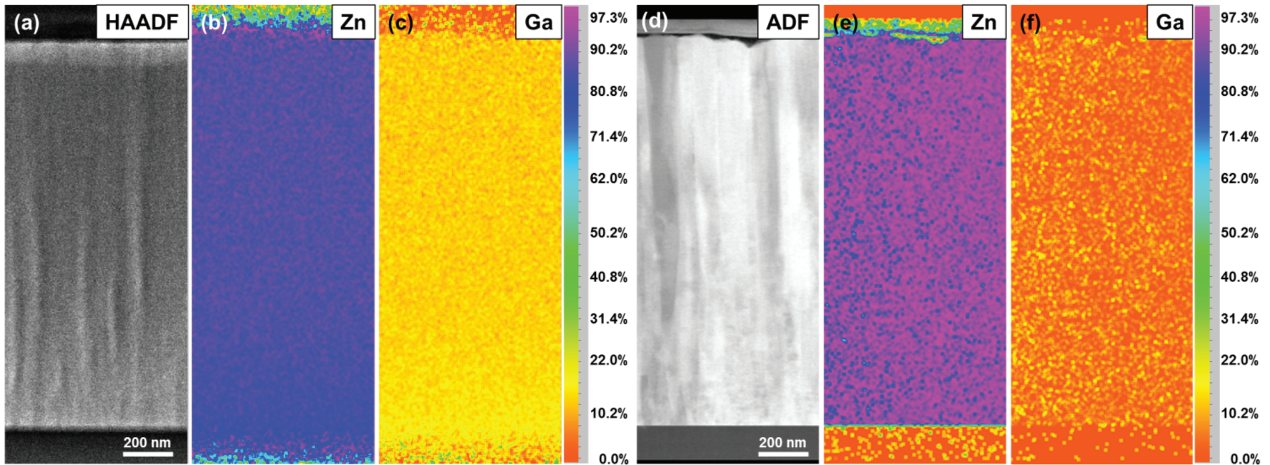

FIG. S2: (a)-(d) Low-magnification HAADF-STEM image of the $x = 0.15$ thin film and the corresponding EDX maps of Zn and Ga atomic %. (d)-(f) Low-magnification ADF-STEM image of the $x = 0.02$ thin film and the corresponding EDX maps of Zn and Ga atomic %. Homogeneous random alloys are illustrated, with no indication of large or medium-scale phase separation and elemental clustering.

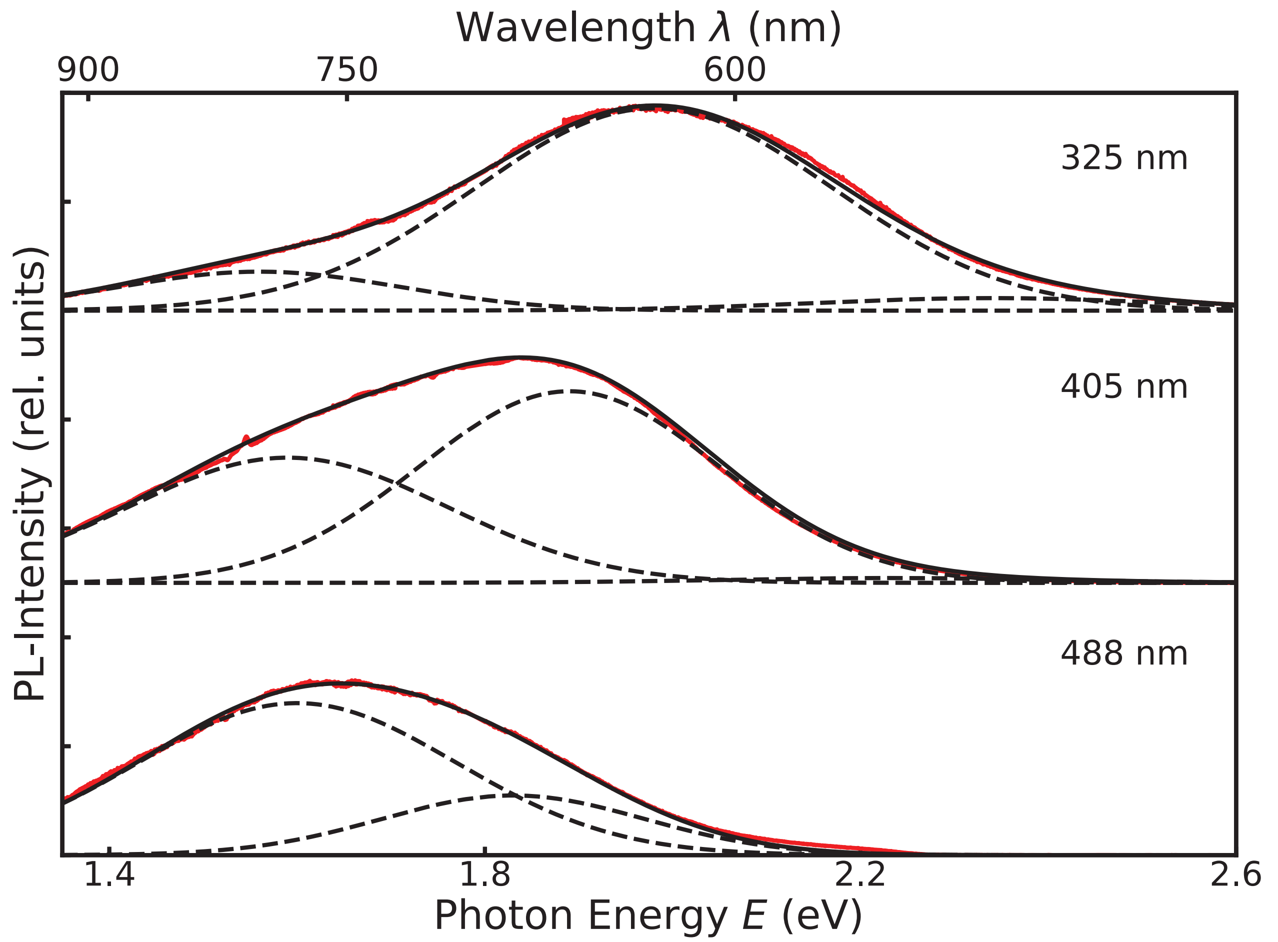

FIG. S3: Deconvolution of PL spectra recorded for $x = 0.15$ thin film at different excitation wavelengths, i.e. 325 nm, 405 nm and 488 nm. The deconvolution was performed using three Gaussians.

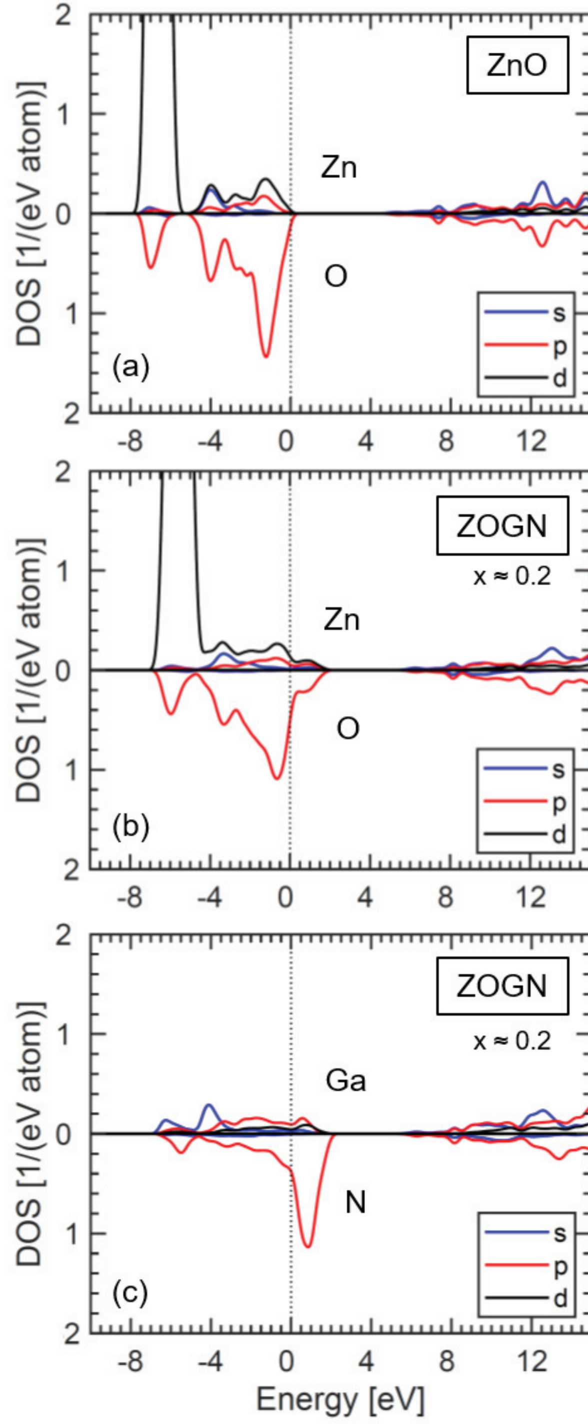

FIG. S4: Orbital-projected PDOS for (a) ZnO, (b) Zn and O atoms in ZOGN for x ≈ 0.2, and corresponding (c) Ga and N atoms in ZOGN. The upper (lower) panels in the subfigures show the cations (anions). Energies refer to the VBM of pristine ZnO.

Paper IV

Formation of N_2 bubbles along grain boundaries in $(ZnO)_{1-x}(GaN)_x$: nanoscale STEM-EELS studies

C. Bazioti, V. S. Olsen, A. Yu. Kuznetsov, L. Vines and Ø. Prytz

Physcial Chemistry Chemical Physics Communications, 2019

My contribution: Planning experiments, fabricate thin films, thin film post-growth processing, discussing results, contributing to manuscript and proof-reading.

PCCP

ROYAL SOCIETY OF CHEMISTRY

COMMUNICATION

View Article Online
View Journal

Cite this: DOI: 10.1039/c9cp06025a

Received 6th November 2019,
Accepted 7th January 2020

DOI: 10.1039/c9cp06025a

rsc.li/pccp

Formation of N_2 bubbles along grain boundaries in $(ZnO)_{1-x}(GaN)_x$: nanoscale STEM-EELS studies†

Calliope Bazioti, * Vegard S. Olsen, Andrej Y. Kuznetsov, Lasse Vines and Øystein Prytz

Open Access Article. Published on 31 January 2020. Downloaded on 2/10/2020 4:22:46 PM.
This article is licensed under a Creative Commons Attribution-NonCommercial 3.0 Unported Licence.

Direct evidence of N_2 formation after annealing of $(ZnO)_{1-x}(GaN)_x$ alloys was revealed. N_2 was trapped by V_{Zn+Ga}-clusters, forming faceted voids along grain boundaries. This study shows that N–N bonding is a competitive path for nitrogen after annealing, in addition to the increasing Ga–N bonds, indicating that N in O substitution sites (N_O) is not a stable configuration.

$(ZnO)_{1-x}(GaN)_x$ (ZOGN) alloys are intriguing candidates for bandgap engineering, since the bandgap energy (E_g) of the system is reduced in comparison to its binary compounds (E_g^{ZnO} ~ 3.3 eV, E_g^{GaN} ~ 3.4 eV) due to a strong band bowing effect.[1] By tuning the alloy composition (x), E_g can be tailored from the UV-range into the visible part of the spectrum, making ZOGN a strong candidate for photovoltaic[2,3] and solar water-splitting[4–6] applications. However, the overall micro and nano-structure can strongly affect the semiconductor properties and device performance.[7,8] In particular, the presence of grain boundaries and segregation of point defects along them has been linked to potential-barrier variations in polycrystalline ZnO, and variations in dislocation density have been related to changes in the photoluminescence spectra of ZnO.[9–12] Moreover, chemically induced phenomena such as phase separation and elemental clustering can play a detrimental role in the functional properties of an alloy system. Post-deposition annealing usually improves the crystalline quality[13–16] and recently Olsen *et al.*[2,17,18] conducted a comprehensive study on magnetron sputtered ZnO-rich ZOGN thin films, elucidating the influence of composition and post-deposition annealing on the film properties, as well as investigating the mechanisms governing the band bowing effect. In the same study,[17] DFT calculations revealed that the total energy of the system decreased by increasing the amount of Ga–N bonds, predicting a re-arrangement of the nitrogen bonds during post-deposition annealing. However, the behaviour of N in these alloys is not yet understood, and the proposed Ga–N bonds are not confirmed, warranting a detailed analysis on the nanoscopic scale.

In the present work, a detailed nanoscale investigation was conducted for the first time on magnetron sputtered $(ZnO)_{0.85}(GaN)_{0.15}$ thin films deposited on (0001) α-Al_2O_3 substrates. In this respect, (Scanning) Transmission Electron Microscopy ((S)TEM) was employed, combined with Electron Energy-Loss Spectroscopy (EELS) and Energy-Dispersive X-ray spectroscopy (EDX). Taking advantage of the possibility to use multiple detectors simultaneously, a direct correlation of the atomic structure to chemical information and bonding type gave valuable insight into the elemental and bonding distribution on the atomic scale and its correlation to defects. The influence of post-deposition annealing was investigated, as well as the impact of variations in the N_2 gas flow during sputter deposition.

The formation of single-domain thin films exhibiting columnar grain structure was illustrated (S1, ESI†). (S)TEM imaging before and after annealing, showed an increase in the width of the grains, as well as a reduction in the threading dislocation (TD) density. EDX analysis on the meso-scale showed that the films are random alloys, exhibiting a homogeneous elemental distribution (S2, ESI†).

Despite this meso-scale improvement of the crystalline quality of the films, thermally induced nano-sized volumes were detected on the nano-scale. STEM-imaging was conducted using simultaneously high-angle annular dark field (HAADF), annular dark field (ADF) and annular bright field (ABF) detectors, to obtain complementary views of these volumes. Fig. 1a presents an ADF-STEM image showing a thin area of the film after annealing. Nano-sized areas exhibiting darker contrast are observed, preferentially formed along grain boundaries and TDs. High-resolution ADF-STEM images recorded along the $[1\bar{1}00]$ and $[11\bar{2}0]$ zone axes (Fig. 1b and c) illustrate a close-up of these regions, with a size ranging from ~5 to ~10 nm. These areas

Department of Physics, Centre for Materials Science and Nanotechnology, University of Oslo, PO Box 1048, Blindern, N-0316 Oslo, Norway. E-mail: kalliopi.bazioti@smn.uio.no

† Electronic supplementary information (ESI) available: Experimental methods employed including Magnetron Sputtering deposition, (Scanning) Transmission Electron Microscopy, Electron Energy-Loss Spectroscopy, TEM sample preparation, evaluation of sample thickness by low-loss EELS, Selected Area Diffraction Patterns, Weak-Beam Dark Field g/3g method, Energy-Dispersive X-ray spectroscopy meso-scale maps, simultaneous imaging with HAADF-ADF-ABF detectors, polarity investigation, and impact of changes in the N_2 flow. See DOI: 10.1039/c9cp06025a

Open Access Article. Published on 31 January 2020. Downloaded on 2/10/2020 4:22:46 PM.
This article is licensed under a Creative Commons Attribution-NonCommercial 3.0 Unported Licence.

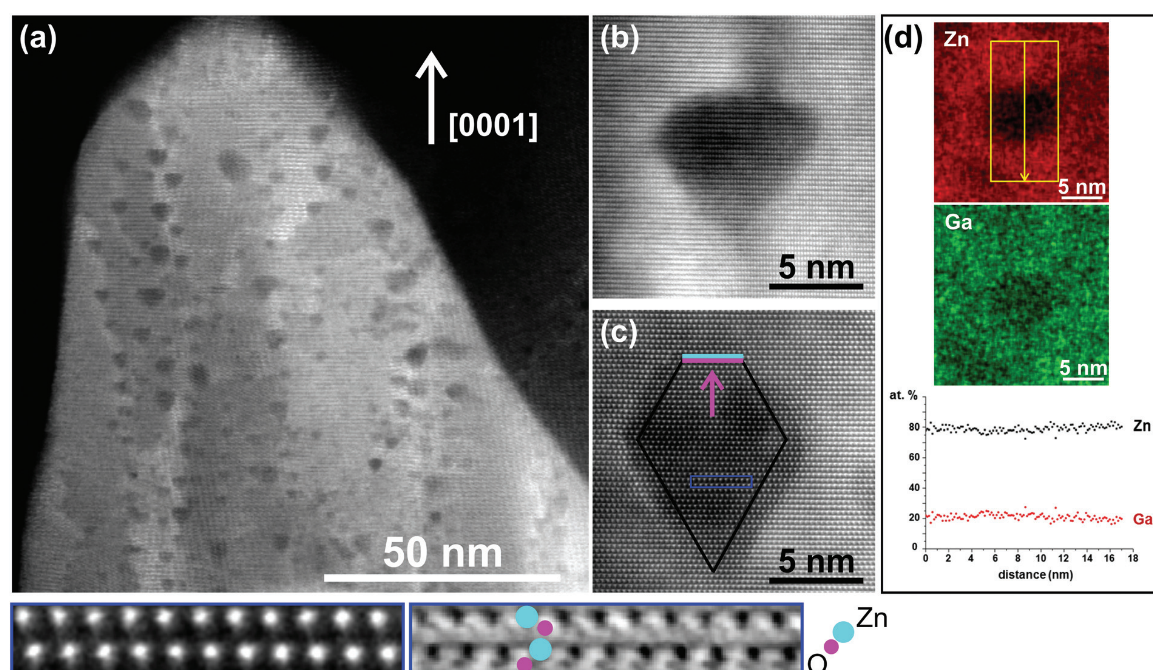

Fig. 1 (a) ADF-STEM image, showing formation of thermally-induced nano-sized voids along grain boundaries and threading dislocations. (b) and (c) High-resolution ADF-STEM images along the [1$\bar{1}$00] and [11$\bar{2}$0] zone axes respectively, illustrating that the voids are not amorphous areas and they are surrounded by well-defined facets. The enlarged insets of the area annotated by the blue box show the corresponding HAADF and ABF images recorded simultaneously. By resolving the Zn–O dumbbells the polarity was identified showing that only the O-terminated internal polar facets are stabilized (purple line) along with the semi-polar facets (black lines). (d) EDX maps carried out in STEM-mode, show a reduction in both Zn and Ga counts and the void formation is attributed to agglomeration of Zn-vacancies (V_{Zn}) and Ga-vacancies (V_{Ga}). It is important that elemental quantification extracted by EDX line profiles crossing the voids, showed no changes in the relative at% ratio between Ga and Zn, indicating no phase separation phenomena or elemental clustering.

are not amorphous and there is no structural change observed, since the ABABAB stacking sequence of the hexagonal structure along the [0001] direction is retained. Moreover, imaging did not reveal any Moiré fringes. Evidently, these regions are surrounded by well-defined facets mainly on semi-polar planes ({10$\bar{1}$1}, {11$\bar{2}$2}), along with truncations on the polar {0001} planes. The enlarged insets are the corresponding HAADF and ABF images of the area annotated by the blue box in Fig. 1c. By resolving the Zn–O dumbbells, the polarity of the films is identified as Zn-faced (growth along the [0001] direction), indicating that the O-terminated internal polar facets of these regions are more stable, compared to the Zn-terminated polar facets (also S3, ESI†). Accounting that in HAADF-STEM imaging (S4, ESI†), contrast depends on Z and at high collection angles is formed by scattering from heavy elements, these dark regions indicate volumes with lower atomic density and their formation is attributed to agglomeration of vacancies (V).[19] Since the concentration of Zn in the alloy is ~85 at%, agglomeration of Zn-vacancies (V_{Zn}) is expected to contribute more in the formation of these volumes, however we cannot exclude a smaller contribution of Ga-vacancies (V_{Ga}) as well. Indeed, EDX-STEM maps of a lower-contrast volume, showed a reduction in both Zn and Ga counts (Fig. 1d). Elemental quantification extracted by EDX line profiles crossing these volumes showed no changes in the relative at% ratio between Zn and Ga, indicating no phase separation phenomena and no elemental clustering. Based on the size and lower atomic density of these areas, we hereafter label them nano-sized voids.

Hence, EDX-STEM that is sensitive for the detection of heavy elements revealed no inhomogeneities in Zn and Ga distribution in both meso and nano-scale. However EDX is not ideal for the analysis of light elements due to the low fluorescence yield (less X-rays are produced because the formation of Auger electrons is favoured) and due to the background X-ray (Bremsstrahlung). Therefore, for the detection of light elements we employed EELS in STEM-mode that offers superior spatial and energy resolution and enables access to chemical bonding information. Fig. 2 shows a high-resolution ADF-STEM image (inset) where EELS spectra of the N–K and O–K edges were acquired by 2D scans from (1) a void and (2) the surrounding ZOGN matrix. EELS revealed that these voids are N-rich regions. Moreover, the shape and energy-position of the N–K edge indicate the presence of molecular nitrogen (N_2), as shown by the comparison with N_2 reference spectra.[20] EELS spectra acquired from the ZOGN matrix revealed a different shape of the N–K peak compared to that of N_2, indicating that N is bonded to the metal atoms. A comparison with spectra from a wz-GaN reference sample indicates that the Ga–N bonds proposed by DFT[17] are also present. It should be clarified that the shape of spectrum 1 is the result of overlapped signals along the beam path (void + the surrounding ZOGN matrix).

Open Access Article. Published on 31 January 2020. Downloaded on 2/10/2020 4:22:46 PM.
This article is licensed under a Creative Commons Attribution-NonCommercial 3.0 Unported Licence.

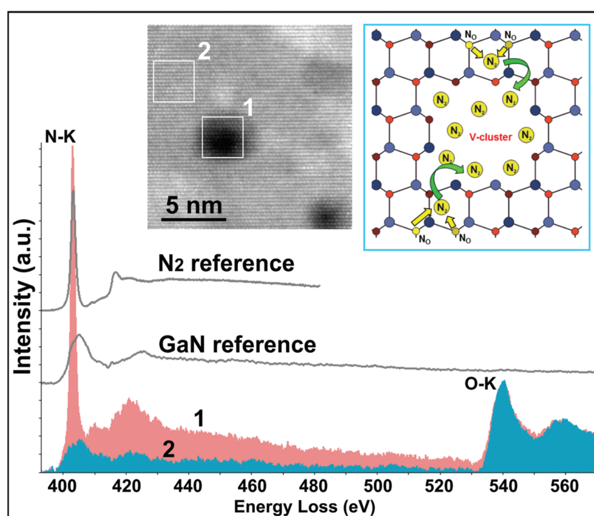

Fig. 2 EELS-spectra acquired from 2D scans (1) inside a void and (2) the surrounding matrix, as annotated in the high-resolution STEM image (inset). Voids are N-rich regions and the shape and energy-position of the N–K edge indicate the existence of N–N bonds in the voids along with Ga–N bonds in the ZOGN matrix. A second inset shows a model describing the N_O instability, formation of N_2 molecules and trapping by V-clusters.

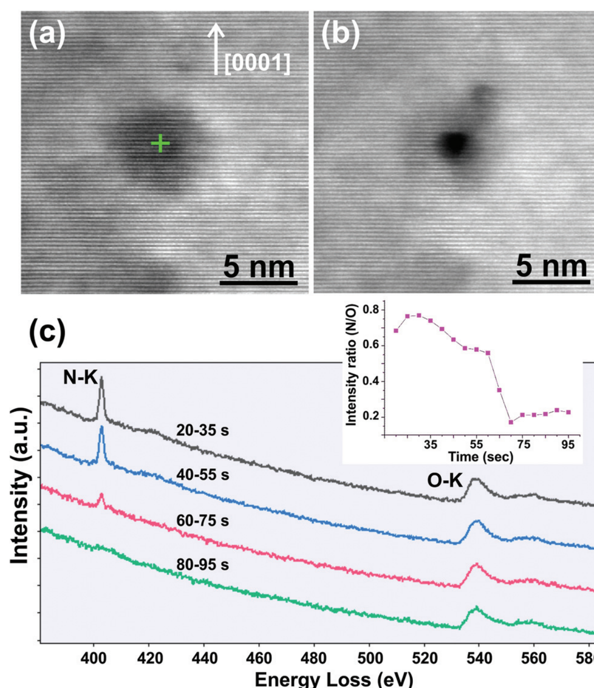

Fig. 3 (a) and (b) ADF-STEM images of a N_2-filled void recorded before and after drilling a hole *in situ* using a focused electron beam. (c) Time resolved EELS spectra acquired while drilling the hole, showing an abrupt decrease in the intensity ratio of N–K/O–K peaks after 70 s. After the release of the N_2-bubble, the O–K peak is still present, indicating that there is still ZOGN matrix left.

A time resolved electron beam irradiation experiment was also performed in order to drill a hole *in situ* at the position of a void, while simultaneously recording an EELS spectrum every 0.5 s. A focused electron beam of sub-Å diameter and 350 pA current was used. Fig. 3a and b show ADF-STEM images of a void before and after the hole-drilling, respectively. The intensity ratio of the N–K/O–K peaks decreases abruptly after irradiation for 70 s (Fig. 3c), indicating a sudden removal of N_2. After the release of the N_2-bubble, the O–K peak is still present, indicating that there is still ZOGN matrix left. For ease of comparison, the EELS spectra were normalized to the O–K edge.

In addition to the post-annealing effect, we also examined the influence of the N_2 gas flow that is applied during film deposition. In this respect, we studied annealed ZOGN films that were deposited under the same conditions but with reduced N_2 gas flow (from 5 to 2.5 sccm). Nano-sized voids along grain boundaries and threading dislocations are still present, however EELS spectra reveal a significantly lower N–K signal (or absence of N–K signal), indicating that less N has been incorporated in the films and therefore trapped by the voids (non-stoichiometric conditions). The empty voids are found to be sharply faceted even at small sizes, while the N_2-filled voids are more round and the well-defined facets appear as the voids grow in size (S5, ESI†). Furthermore, the O-terminated internal polar facets disappear as the voids grow in size and only the semi-polar facets ($\{10\bar{1}1\}$, $\{11\bar{2}2\}$) prevail.

This study shows that post-deposition thermal annealing results in a meso-scale crystal quality enhancement, as revealed by the grain enlargement and the TD-density reduction. However, in addition to the aforementioned line defects, a high concentration of point defects is expected (vacancies and atoms at interstitial positions) and our study goes further in terms of the comprehensive picture regarding the elemental distribution and bonding arrangement on the nano-scale. In particular, our results showing that after annealing large amounts of nitrogen are trapped by the voids as N_2, indicate that N is not stable on the O substitutional site (N_O). N_O would be easily kicked out to an interstitial site (N_i) and due to the large N_i–N_i binding energy, N_2 molecules can easily form.[21] At the same time upon annealing, agglomeration of Zn-vacancies (V_{Zn}) and Ga-vacancies (V_{Ga}) along grain boundaries and TDs occurs. These vacancy-clusters act as traps for N_2 molecules and gradually grow in size, ultimately forming faceted nano-voids. Nijikovsky *et al.*[19] suggested that void formation can also be facilitated by pipe diffusion of the generated vacancies through dislocations that define the low-angle grain boundaries. After exceeding a critical size, the voids reach an equilibrium shape in order to minimize their energy state. This shape is determined by the surface energy of different facets. In our study the voids exhibited an asymmetric diamond shape related to the different surface energy for facets of opposite polarity. In particular, the O-terminated internal polar facets are more stable than the Zn-terminated, in agreement with previous observations.[22] This polar facet disappears as the voids grow in size and finally only the semi-polar facets prevail. This is in agreement with calculations showing that the polar planes in ZnO exhibit higher surface formation energy compared to the non-polar planes.[23,24] Trapping of large amounts of N at the voids leads to formation of overpressurized bubbles. Under the pressure of the accumulated gas,

Open Access Article. Published on 31 January 2020. Downloaded on 2/10/2020 4:22:46 PM.

This article is licensed under a Creative Commons Attribution-NonCommercial 3.0 Unported Licence.

the N_2-filled voids undergo plastic deformation, resulting in more rounded-shape facets. It should be emphasized that while our results show that large amounts of nitrogen are trapped in the voids as N_2, there is also a significant amount of N in the ZOGN matrix, bonded to Ga and presumably Zn. This is also in agreement with our previous DFT calculations that suggest an increase in the number of Ga–N bonds after thermal treatment.[17] However, the present study reveals that N–N bonding is an alternative path for nitrogen after annealing. It is also important that our results show that the increase in the Ga–N bonds did not lead to phase separation phenomena or clustering (*e.g.* GaN *vs.* ZnO phases). This means that our previously shown bandgap measurements on the nanoscale with EELS-STEM, are the result of a homogeneous alloy and not an average of a mixture of phases.[18]

Our findings support previous theoretical and experimental reports regarding the behaviour of N in ZnO. In particular, Fons *et al.*[25] attributed the low p-type doping efficiency of N in ZnO to the low stability of N_O, and showed the presence of N–N bonds by X-ray absorption experiments. DFT calculations by Gao *et al.*[21] showed that N_O can be easily deactivated to an interstitial site and form N–N bonds. Calculations by Nickel and Gluba[26] showed that the O site is energetically unfavourable for the localization of N_2, and calculations by Lambrecht and Boonchun[27] showed that N_2 may occupy a V_{ZN} site. However, these studies calculate energetics of single molecules in the lattice and X-ray absorption cannot provide information regarding the spatial distribution of the N-signal. In this study, STEM-EELS provides the advantage of both imaging and spectroscopy on the atomic scale, correlating simultaneously the atomic structure, chemical information and bonding type. Recently Bazioti *et al.*[28] showed with STEM-EELS stabilization of V_{Zn}-clusters by N_2 molecules and suppression of V_{zn}–Zn_i recombination in N-implanted ZnO after annealing.

In summary, the first comprehensive nanostructural and chemical report on magnetron sputtered ZOGN alloys was conducted. The elemental distribution and bonding re-arrangement was elucidated as a function of growth conditions and the evolution of thermally-induced defects was described. In particular, the meso-scale crystalline quality was improved after thermal annealing, as revealed by the enlargement of grains and the reduction of threading dislocation density. However, nano-sized voids were formed mainly along grain boundaries and STEM-EELS analysis showed direct evidence of molecular nitrogen (N_2) filling the voids, indicating that N is not stable on the O substitution site (N_O). Their formation is attributed to N_2-trapping by V_{zn+Ga} clusters that upon annealing further agglomerate ultimately forming nano-voids. The voids reached an equilibrium shape defined by the energetically favourable facets, mainly on the semi-polar planes and the O-terminated internal polar plane. This study reveals that the N–N bonding is an alternative path for nitrogen after annealing, in addition to the increase in the Ga–N bonds that reduces the total energy of the system. Despite this re-arrangement of N-bonds, no phase separation phenomena were observed (GaN *vs.* ZnO) indicating that the previously reported bandgap of the system is the result of a homogeneous ZOGN alloy and not an average of a mixture of different phases.

Conflicts of interest

There are no conflicts to declare.

Acknowledgements

Research Council of Norway is acknowledged for support to the Norwegian Center for Transmission Electron Microscopy (NORTEM) (no. 197405/F50), the top-tier research project FUNDAMeNT (no. 251131), the Norwegian Micro and Nano-Fabrication Facility (NorFab) (no. 245963/F50) and the SALIENT project (no. 239895).

Notes and references

1 K. Maeda, K. Teramura, D. Lu, T. Takata, N. Saito, Y. Inoue and K. Domen, *Nature*, 2006, **440**, 295.
2 V. S. Olsen, C. Bazioti, A. Azarov, B. G. Svensson, A. Kuznetsov, Ø. Prytz and L. Vines, *Semicond. Sci. Technol.*, 2019, **34**, 1.
3 C. Yang, Y. Hirose, T. Wakasugi, N. Kashiwa, H. Kawai, K. Yamashita and T. Hasegawa, *Phys. Rev. Appl.*, 2018, **10**, 1.
4 K. Maeda, K. Teramura, T. Takata, M. Hara, N. Saito, K. Toda, Y. Inoue, H. Kobayashi and K. Domen, *J. Phys. Chem. B*, 2005, **109**, 20504.
5 K. Maeda and K. Domen, *Chem. Mater.*, 2010, **22**, 612.
6 H. Chen, L. Wang, J. Bai, J. C. Hanson, J. B. Warren, J. T. Muckerman, E. Fujita and J. A. Rodriguez, *J. Phys. Chem. C*, 2010, **114**, 1809.
7 D. B. Holt and B. G. Yacobi, *Extended Defects in Semiconductors*, Cambridge University Press, Cambridge, 2007.
8 H. J. Queisser and E. E. Haller, *Science*, 1998, **281**(5379), 945.
9 Y. Ohno, H. Koizumi, T. Taishi, I. Yonenaga, K. Fujii, H. Goto and T. Yao, *J. Appl. Phys.*, 2008, **104**(7), 073515.
10 W. R. Liu, W. F. Hsieh, C. H. Hsu, K. S. Liang and F. S. S. Chien, *J. Cryst. Growth*, 2006, **297**(2), 294.
11 M. A. McCoy, R. W. Grimes and W. E. Lee, *J. Mater. Res.*, 1996, **11**(8), 2009.
12 H. S. Domingos, P. D. Bristowe, J. Carlsson and B. Hellsing, *Interface Sci.*, 2001, **9**(3), 231.
13 S. R. Aghdaee and V. Soleimanian, *J. Cryst. Growth*, 2010, **312**, 3050.
14 B. Y. Oh, M. C. Jeong, D. S. Kim, W. Lee and J. M. Myoung, *J. Cryst. Growth*, 2005, **281**, 475.
15 B. D. Ahn, S. H. Oh, C. H. Lee, G. H. Kim, H. J. Kim and S. Y. Lee, *J. Cryst. Growth*, 2007, **309**, 128.
16 S. Y. Kuo, W. C. Chen, F. I. Lai, C. P. Cheng, H. C. Kuo, S. C. Wang and W. F. Hsieh, *J. Cryst. Growth*, 2006, **287**, 78.
17 V. S. Olsen, C. Bazioti, G. Baldissera, A. Azarov, Ø. Prytz, C. Persson, B. G. Svensson, A. Y. Kuznetsov and L. Vines, *Phys. Status Solidi B*, 2019, 1800529.
18 V. S. Olsen, G. Baldissera, C. Zimmermann, C. S. Granerød, C. Bazioti, A. Galeckas, B. G. Svensson, A. Yu. Kuznetsov,

C. Persson, Ø. Prytz and L. Vines, *Phys. Rev. B: Condens. Matter Mater. Phys.*, 2019, **100**, 165201.
19 B. Nijikovsky, J. J. Richardson, M. Garbrecht, S. P. DenBaars and W. D. Kaplan, *J. Mater. Sci.*, 2013, **48**, 1614.
20 A. Kovács, B. Schaffer, M. S. Moreno, J. R. Jinschek, A. J. Craven, T. Dietl, A. Bonanni and R. E. Dunin-Borkowski, *J. Appl. Phys.*, 2013, **114**, 033530.
21 J. Gao, R. Qin, G. Luo, J. Lu, Y. Leprince-Wang, H. Ye, Z. Liao, Q. Zhao and D. Yu, *Phys. Lett. A*, 2010, **374**, 3546.
22 K. S. Chan, L. Vines, L. Li, C. Jagadish, B. G. Svensson and J. Wong-Leung, *Appl. Phys. Lett.*, 2015, **106**, 212102.
23 Y. J. Hong, J. Yoo, Y.-J. Doh, S. H. Kang, K.-j. Kong, M. Kim, D. R. Lee, K. H. Oh and G.-C. Yi, *J. Mater. Chem.*, 2009, **19**, 941.
24 B. Meyer and D. Marx, *Phys. Rev. B: Condens. Matter Mater. Phys.*, 2003, **67**, 035403.
25 P. Fons, H. Tampo, A. V. Kolobov, M. Ohkubo, S. Niki, J. Tominaga, R. Carboni and S. Friedrich, *AIP Conf. Proc.*, 2007, **882**, 381.
26 N. H. Nickel and M. A. Gluba, *Phys. Rev. Lett.*, 2009, **103**, 145501.
27 W. R. L. Lambrecht and A. Boonchun, *Phys. Rev. B: Condens. Matter Mater. Phys.*, 2013, **87**, 195207.
28 C. Bazioti, A. Azarov, K. M. Johansen, B. G. Svensson, L. Vines, A. Y. Kuznetzov and Ø. Prytz, *J. Phys. Chem. Lett.*, 2019, **10**, 4725.

Open Access Article. Published on 31 January 2020. Downloaded on 2/10/2020 4:22:46 PM.
This article is licensed under a Creative Commons Attribution-NonCommercial 3.0 Unported Licence.

Electronic Supplementary Material (ESI) for Physical Chemistry Chemical Physics.
This journal is © the Owner Societies 2020

Supplementary material

Experimental

$(ZnO)_{1-x}(GaN)_x$ thin films were deposited on (0001) a-Al_2O_3 substrates, using a Moorfield Minilab magnetron sputtering system with separate ZnO (99.999% purity) and GaN (99.99% purity) 3 inch ceramic targets. Prior to deposition, the sapphire substrates were cleaned by annealing in oxygen atmosphere for 1 h at 1150 ^oC, before the samples were loaded into the sputter chamber. The base pressure prior to deposition was below $2x10^{-6}$ Torr before deposition was started, while the pressure during deposition was kept at 7 mTorr. The substrate temperature was kept at 400 ^oC and the sample stage was rotated at 11 rpm to ensure good film uniformity. In order to remove surface impurities from the targets, a pre-sputtering cleaning was carried out for 20 min before deposition. During the co-sputtering process, where the ZnO and GaN targets are running simultaneously, the composition of the film was controlled by applying different voltages to the two targets, in addition to controlling the gas flows of Ar and N_2 in the chamber. In particular, the x = 0.15 composition was obtained by applying 30W and 20W to the ZnO and GaN targets respectively, while gas flows of 12.5 sccm Ar and 5 sccm N_2 (required in the sputtering chamber for a stoichiometric composition) were kept constant during deposition. Furthermore, a reduced N_2 gas flow at 2.5 sccm -while keeping the other deposition parameters the same- was applied in order to investigate its influence on the film properties. Post-deposition isochronal anneals were performed for one hour in nitrogen atmosphere at 600, 700, and 800 ^oC.

STEM, EELS and EDX investigations were conducted on an FEI Titan G2 60-300 kV equipped with a CEOS DCOR probe-corrector, monochromator and Super-X EDX detectors. Observations were performed at 300 kV with a probe convergence angle of 24 mrad. The camera length was set to 77 mm and simultaneous STEM imaging was conducted with 3 detectors: HAADF (collection angles 98.7-200 mrad), ADF (collection angles 21.5-98.7 mrad) and ABF (collection angles 10.6-21.5 mrad). The resulting spatial resolution achieved was approximately 0.08 nm. EELS was performed using a Gatan Quantum 965 imaging filter. The energy dispersion was 0.1 eV/channel and the energy resolution measured using the full width at half maximum (FWHM) of the zero-loss peak was 1.1 eV. Electron transparent TEM samples with a cross-sectional wedge geometry were prepared by mechanical grinding and polishing (Allied MultiPrep). Final thinning was performed by Ar ion milling with a Fishione Model 1010, and plasma cleaning was applied directly before the TEM investigations, with a Fishione Model 1020. The sample thickness (t) was evaluated by low-loss EELS according to $\frac{t}{\lambda} = \ln\left(\frac{I_t}{I_0}\right)$, where λ is the inelastic mean free path, I_t the intensity of the entire spectrum and I_0 the intensity of the zero loss peak. The sample thickness was estimated to be ~10 nm using this method.

Results

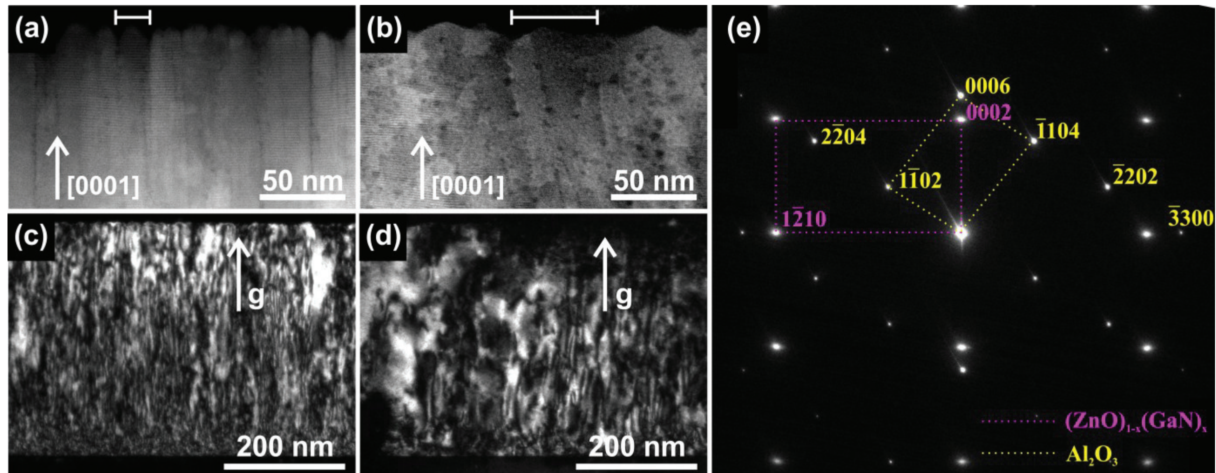

S1: (a)-(b) ADF-STEM images recorded close to the surface of the $(ZnO)_{0.85}(GaN)_{0.15}$ thin films before and after thermal annealing respectively. (c)-(d) TEM WBDF g/3g images obtained under two-beam conditions with g0002 before and after thermal annealing respectively. A clear increase in the grain size is observed after annealing, resulting in an improved crystal quality of the films, with lower threading dislocation (TD) density. (e) Selected Area Electron Diffraction (SAED) pattern revealing a highly crystalline single-domain film of wurtzite phase, exhibiting a good heteroepitaxial relationship with the (0001) a-Al_2O_3 substrate described by: $[0001]_{(ZnO)0.85(GaN)0.15}$//$[0001]_{Al2O3}$ (out-of-plane) and $[10\text{-}10]_{(ZnO)0.85(GaN)0.15}$//$[11\text{-}20]_{Al2O3}$ (in-plane). This relationship implies a 30° in-plane rotation of the film unit cell with respect to that of the substrate (the so-called 'aligned domain'). This orientation relationship is favourable since it results in a reduction of mismatch $((d_f – d_s)/d_s$, where d_f and d_s denote the interplanar spacing of the film and substrate, respectively) from 32% to 18%.

Regarding the comparison of TD density, careful characterization was performed, working in TEM-mode under two-beam conditions using the **weak-beam dark field g/3g method** (WBDF). This method is ideal for characterization of extended defects, due to a small excitation error, so defects as TDs are better resolved. According to the invisibility criterion *g.b* (where b is the Burgers vector), we can identify the TD-type working under different two-beam conditions. The comparison was made in areas having the same thickness along the viewing direction.

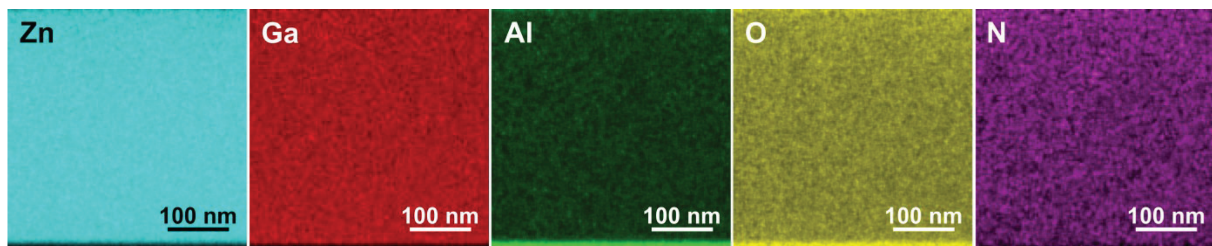

S2: EDX maps carried out in STEM-mode with 5 nm pixel size. The annealed films are random alloys on the meso-scale, exhibiting a homogeneous elemental distribution with no indication of phase separation phenomena and intense elemental clustering.

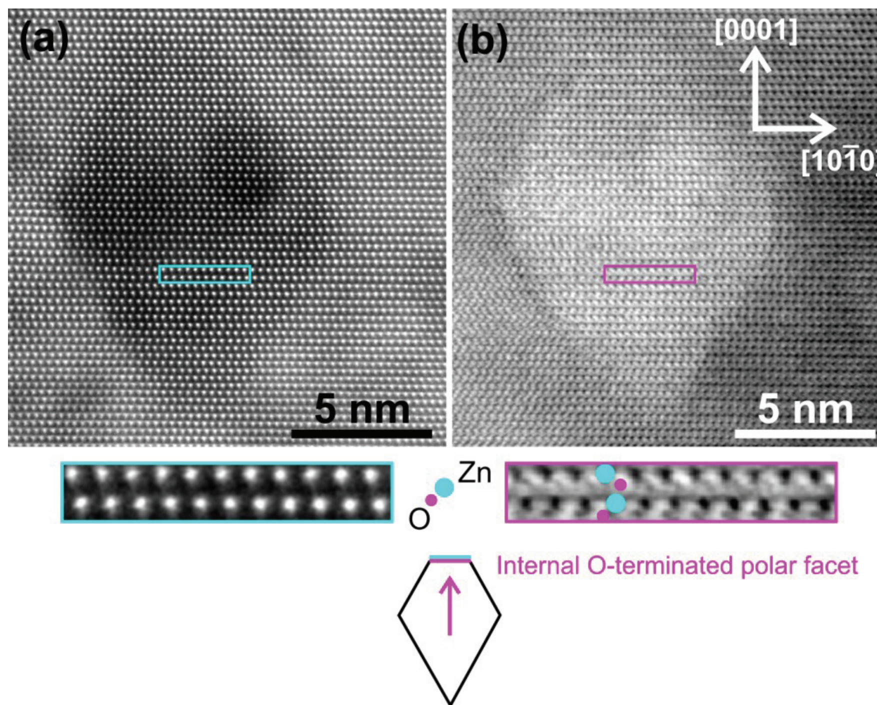

S3: (a) HAADF-STEM and (b) ABF-STEM images of a void recorded simultaneously. In HAADF only atomic columns of heavy elements (Zn and Ga) are detected while ABF provides visualization of both heavy and light elements (Zn, Ga, O, N). By resolving the Zn-O dumbbells the polarity is identified as Zn-faced ([0001] growth direction). Hence the polar facets that are stabilized at the voids are the O-terminated internal facets along with the semi-polar ones.

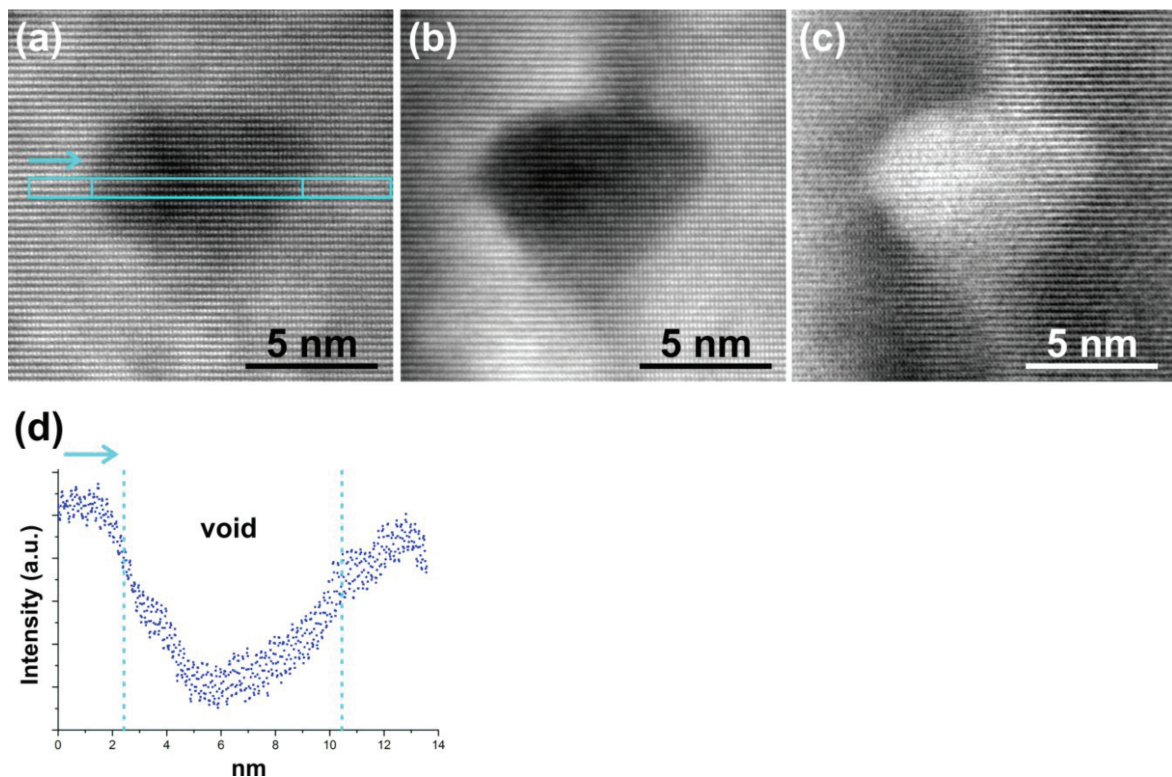

S4: (a) HAADF-STEM, (b) ADF-STEM and (c) ABF-STEM images of a void recorded simultaneously. (d) the intensity profile in HAADF indicates a clear drop in the Z-contrast crossing the void.

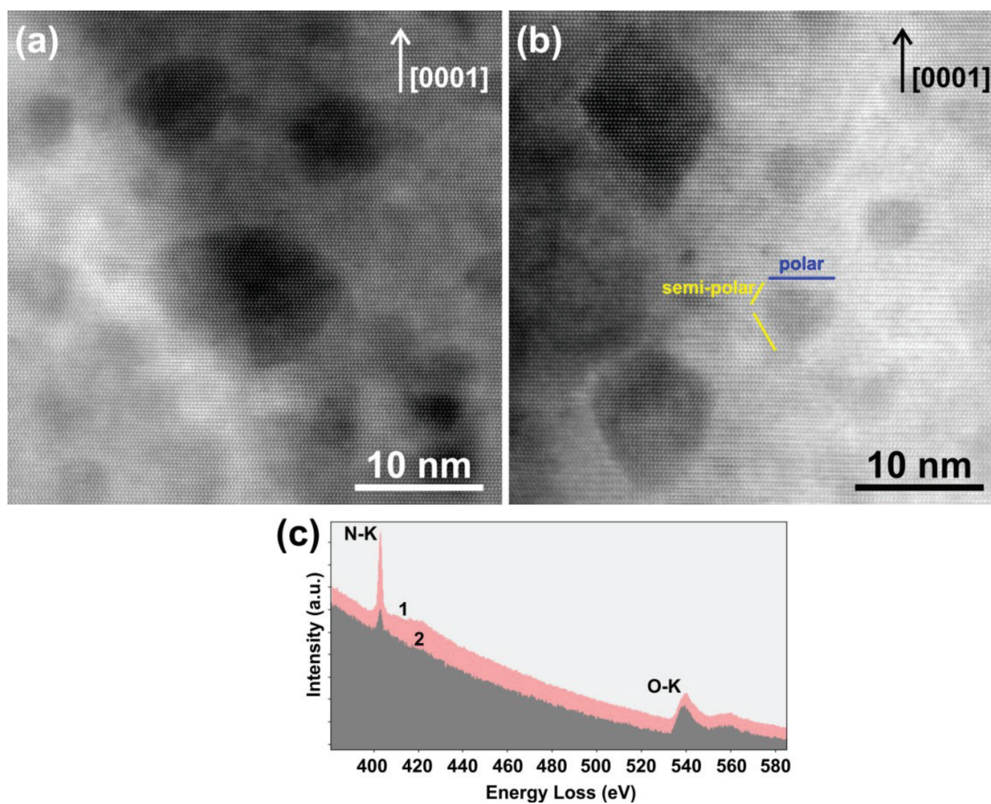

S5: ADF-STEM images showing voids in the case of (a) 5 sccm N_2 flow and (b) 2.5 sccm N_2 flow. In case (a), the voids were filled with N_2 and the facets exhibited more round shape. In case (b), weak (or zero) N-K signals were detected and the voids exhibited well-defined facets even at smaller sizes. It is evident that the facets on the polar {0001} planes appear only in the small voids, while the energetically favorable facets on semi-polar planes prevail as the voids grow in size. (c) Comparison of two EELS spectra (1) from a round void as shown in (a) and (2) from a sharply-faceted void as shown in (b).

Paper V

Interfacial properties and the resulting defects of $(ZnO)_{1-x}(GaN)_x$ thin films grown on c-Al_2O_3

C. Bazioti, V. S. Olsen, A. Yu. Kuznetsov, L. Vines and Ø. Prytz

Manuscript in preparation for submission

My contribution: Planning experiments, fabricate thin films, thin film post-growth processing, XRD measurements, analysing and writing XRD part, discussing results, contributing to manuscript and proof-reading.